SEARCHING FOR THE ORIGINS OF FLUORINE: A MEASUREMENT OF THE ^{19}F(t,^{3}He) REACTION

By

Amanda Margaret Prinke

A DISSERTATION

Submitted to
Michigan State University
in partial fulfillment of the requirements
for the degree of

DOCTOR OF PHILOSOPHY

Physics

2012

ABSTRACT

SEARCHING FOR THE ORIGINS OF FLUORINE: A MEASUREMENT OF THE ^{19}F(t,^{3}He) REACTION

By

Amanda Margaret Prinke

The astrophysical process responsible for fluorine nucleosynthesis has been a matter of significant debate. The β-decay of ^{19}O* in core-collapse supernova has been previously suggested as a possible avenue for fluorine nucleosynthesis. In hot astrophysical environments, it is possible to thermally populate low-lying excited states of ^{19}O, and the β-decay of these excited states would enhance the overall β-decay rate into ^{19}F.

To examine this theory from an experimental nuclear physics perspective, the ^{19}F(t,^{3}He) reaction differential cross section at 345 MeV was measured. This measurement was performed at the National Superconducting Cyclotron Laboratory using a secondary triton beam impinged on a Teflon (CF_2) target. The ^{3}He ejectiles were momentum-analyzed in the S800 spectrograph. A Gamow-Teller strength distribution was extracted from the reaction cross sections. The Gamow-Teller strength for the transition between the ground state of ^{19}F and the 0.096 MeV excited state of ^{19}O was then used to find the ^{19}O* β-decay rate to the ^{19}F ground state over a range of astrophysical temperatures.

The calculated β-decay rate for ^{19}O$^{*}(\beta^{-})^{19}$F with the new experimental measurement taken into account did show a modest enhancement for high stellar temperatures. However, the magnitude of this enhancement was much lower than prior theory calculations had predicted. The β-decay rate enhancement is not large enough to make a significant impact on future fluorine nucleosynthesis simulations.

TABLE OF CONTENTS

LIST OF TABLES

LIST OF FIGURES

Chapter 1

Astrophysics Motivation

1.1 Introduction

Experimental nuclear physics provides a unique opportunity to study the innermost workings of stars in the laboratory. The underlying physics for a nuclear reaction in a star has much in common with nuclear reactions that are produced with a particle accelerator at a research facility. One specific area where experimental nuclear physics has made a significant contribution to astrophysics is in the field of nucleosynthesis research. Nuclear reaction rates measured in laboratories are incorporated into simulations that predict the elemental abundances of stars.

This dissertation describes the measurement of a particular nuclear reaction, ^{19}F(t,^{3}He) at 115 MeV/nucleon, to test a hypothesis on fluorine nucleosynthesis in core-collapse supernovae. The rest of this chapter discusses the motivation for investigating fluorine nucleosynthesis in general as well as the specific reason for studying the ^{19}F(t,^{3}He) in particular. Theoretical principals that are important to charge-exchange reactions and relevant to the experiment's data analysis are explained in Chapter 2. Chapter 3 describes the experiment that was undertaken for this work. The data analysis of this experiment is explicated in Chapter 4; the results of the data analysis and their astrophysical implications are discussed in Chapter 5. A summary of the dissertation is provided in Chapter 6.

1.2 Nucleosynthesis

The study of nucleosynthesis endeavors to answer one of the most fundamental questions of science: *where did we come from?* We have a strong grasp on the origin of some elements [1, 2, and references therein]. Hydrogen (both ^{1}H and ^{2}H) and most helium was produced in the first moments of the universe during the Big Bang. A smaller fraction of helium is generated by hydrogen-burning processes in stellar environments. Carbon is formed from the triple-alpha process in helium-burning stars. Massive helium-burning stars also produce ^{16}O and ^{18}O. The slow neutron capture process, referred to as the s-process [3], explains the solar abundances of many isotopes in the mass range above iron up to bismuth, including krypton, xenon, barium, and lanthanum.

More complex astrophysical processes account for still more elements and for specific isotopes. The s-process is typically characterized by (n, γ) reactions at a time scale that is much slower than the intervening β-decays (over several thousand years) and is thought to occur primarily in asymptotic giant branch (AGB) stars (see Section 1.5). The rapid neutron capture process, referred to as the r-process [3], may explain many of the isotopes with $70 \leq A \leq 209$ (where A is the nucleon number). The r-process is typically characterized by neutron captures on a very short time scale compared to the relevant β-decays (less than 10 seconds) and is thought to occur in core-collapse supernovae (see Section 1.3) or in merging neutron stars. Specifically, the r-process accounts for several neutron-rich stable nuclei that are beyond the reach of the s-process, such as ^{122}Sn and ^{130}Te (the s-process is essentially blocked for these nuclei because there are intervening unstable nucleus in their isotopic chains, ^{121}Sn and ^{129}Te respectively, which will β-decay before more s-process neutrons are captured, meaning that ^{122}Sn and ^{130}Te are only accessible via rapid neutron captures). The r-process

may also account for naturally occurring thorium and uranium isotopes, which are too far beyond the stable isotopes to be produced by the s-process. The neutrino nucleosynthesis process occurs when supernovae release large amounts of neutrinos, and these neutrinos interact with stellar material to produce low-abundance isotopes [4, 5]. The neutrino process might account for the solar abundance of isotopes such as ^{138}La and ^{180}Ta, and it may partially contribute to the solar abundance of ^{11}B [6].

Several other astrophysical processes are also being explored as explanations for observed astrophysical abundance patterns. These include carbon, neon, oxygen, or silicon burning in massive stars, as well as proton capture (p-process) and rapid proton capture (rp-process). The origin of fluorine, however, has been a persistent mystery despite significant research efforts.

Fluorine nucleosynthesis is a challenging area of research. Theoretical efforts to model fluorine production in stellar environments have frequently been stymied by inadequate nuclear reaction rate data. Recently, there have been significant experimental improvements in many of the nuclear reaction rates tied to fluorine production; several recent measurements will be discussed later in this chapter. Hopefully, these reaction rate improvements (including the rate that is the subject of this dissertation) will pave the way for a more definitive theoretical explanation for fluorine nucleosynthesis. However, the biggest obstacle to creating a reliable model of fluorine production is arguably the "fragility" of the fluorine nucleus, meaning that ^{19}F is easily destroyed in stellar environments via neutron capture $\left(^{19}\mathrm{F}(n,\gamma)^{20}\mathrm{F}\right)$, alpha capture $\left(^{19}\mathrm{F}(\alpha,p)^{22}\mathrm{Ne}\right)$, or proton capture $\left(^{19}\mathrm{F}(p,\alpha)^{16}\mathrm{O}\right)$. This fragile nature leads to fluorine having a very low solar abundance relative to neighboring isotopes; it has the lowest abundance in the range of elements between carbon and calcium [7]. Efforts to explain fluorine production focus primarily on this problem and search for ways to

preserve significant quantities of fluorine from premature destruction. So far, no explanation offered for fluorine production fully explains the measured astrophysical abundances.

Another major challenge in this field is the astrophysical observation of fluorine. The low abundance of fluorine and its particular physical properties coalesce to make it very hard to detect [8]. Most of our knowledge of galactic fluorine abundances comes from the stellar absorption lines of HF molecules, which are found only in cool stars or in sunspots. Many of the vibration-rotation absorption lines from HF overlap with lines from other common molecules, like $^{12}C^{14}N$ [8, 9]. This makes the detection of a low-abundance element like fluorine very difficult. It also leads to some model-dependence in fluorine abundance measurements, where different predictions of contaminants can heavily influence the final fluorine abundance determination. Absorption lines from elemental fluorine have been observed in hotter stars, but such measurements are difficult because these absorption lines fall on the edge of the visible spectrum near the ultraviolet region [10, 11] or in the far ultraviolet region of the spectrum [12, 13].

In fact, the one and only measure to date of our own Sun's fluorine abundance was performed in 1969 by examining the spectral lines produced by the molecule HF in sunspots [14]. The molecule HF only forms in cool stars or in relatively cool locations like sunspots; most fluorine in the Sun and similar stars is elemental. Hall and Noyes found a solar abundance[1] of $A(\mathrm{F}) = 4.56 \pm 0.33$ in the Sun. The only other measure available for the solar system's fluorine abundance comes from abundance measurements performed on the CI group of car-

[1]Stellar abundances of elements are quantified using a common spectroscopic notation:

$$A(x) = \log \frac{N(x)}{N(\mathrm{H})} + 12.00 \tag{1.2.1}$$

indicates how abundant an element x is compared to the hydrogen in the same star. The scale is defined such that $A(\mathrm{H}) = 12.00$.

bonaceous chondrite meteorites [15], which found a value of $A(\mathrm{F}) = 4.46 \pm 0.06$. At a glance, the meteoric abundance seems like the best choice as a solar system standard for fluorine abundance because of its lower uncertainty, but an earlier review of the meteoric data openly questioned the quality of these measurements [16]. This suggests that the more conservative sunspot measurement with a larger error may be the better option. Fortunately, the sunspot and meteoric abundances are in agreement with each other, but the larger uncertainty of the sunspot measurement can make it difficult to determine whether other stars are exhibiting a significant overabundance of fluorine compared to our solar system.

Three astrophysical sites have been proposed for fluorine nucleosynthesis. All of these sites were suggested because they offer an opportunity to preserve fragile ^{19}F from the capture processes that would otherwise destroy it. Core-collapse supernovae might produce fluorine through an unusual neutrino nucleosynthesis process and eject it prior to its destruction into the interstellar medium through a supernova explosion (see Section 1.3). Wolf-Rayet stars might produce fluorine via helium-burning and then eject it into the interstellar medium in extreme solar winds, preserving it from destruction (see section 1.4). Asymptotic giant branch (AGB) stars might produce fluorine via helium-burning and then eject it into planetary nebulae (see Section 1.5).

1.3 Neutrino Nucleosynthesis of Fluorine

The first theory to attempt to tackle fluorine nucleosynthesis was proposed by Woosley and Haxton [4]. They hypothesized that solar fluorine abundances could be produced in the carbon and neon shells of core-collapse (Type II) supernovae due to interactions with neutrinos (see Figure 1.1). Woosley and Haxton postulated that neutrinos produced in

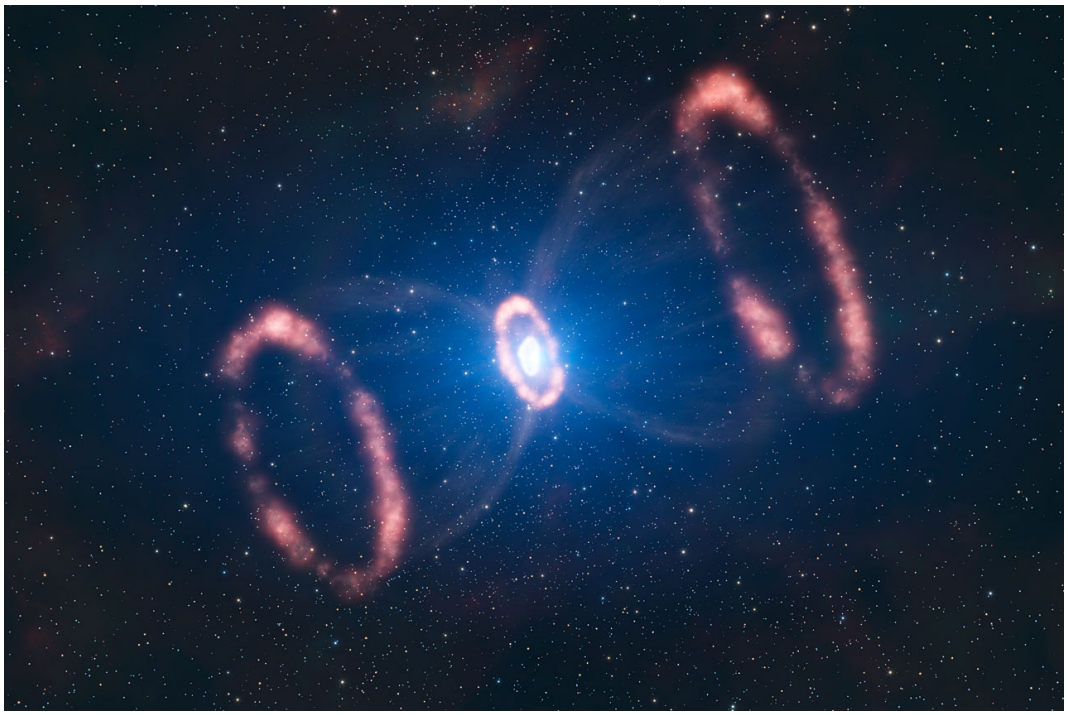

Figure 1.1: This is an artist's impression of the remnants of the core-collapse supernova SN 1987A. Image credit: ESO/L. Calçada [17]. For interpretation of the references to color in this and all other figures, the reader is referred to the electronic version of this dissertation.

the supernova go through inelastic collisions with the abundant ^{20}Ne found in the collapsing star. These inelastic collisions excite the ^{20}Ne nuclei, which can then emit a proton: $^{20}\mathrm{Ne}(\nu,\nu' p)^{19}\mathrm{F}$. The cross section for inelastic neutrino collisions is very low: the average cross section expected for a collision between a ^{20}Ne nucleus and a neutrino from a core-collapse supernova is less than one attobarn (10^{-18} barn) [18]. However, a core-collapse supernova produces a large flux of neutrinos: roughly 10^{58} neutrinos are released in a core-collapse supernova, accounting for about 10^{53} ergs of released energy [6, 18]. This large flux of neutrinos counteracts the low reaction cross section, making neutrino nucleosynthesis a potentially important method of production for certain low-abundance nuclides such as ^{19}F, ^{138}La, and ^{180}Ta. Early core-collapse supernova simulations [18, 19] gave promising results for fluorine production via neutrino nucleosynthesis, and a study by Renda *et al.* [20] em-

ploying a galactic chemical evolution model indicated that solar fluorine abundances could be explained fully by neutrino nucleosynthesis in core-collapse supernovae. Additionally, several astrophysical observations of extrasolar fluorine abundances [21, 22] are consistent with these early neutrino model predictions.

Despite this early success, more recent simulations and observations present a different picture. Heger *et al.* [6] found that revised core-collapse supernovae simulations predicted significantly less fluorine production than prior efforts. Advances in the field of neutrino physics, especially an enhanced understanding of neutrino oscillations, drove this revised study. Improved stellar models and nuclear reaction rates also impacted the newer simulations. An experimental measurement of the Gamow-Teller strength distribution for $^{20}\mathrm{Ne}(p,n)^{20}\mathrm{Na}$ [23] was included in this recent simulation (see Section 2.1 for an explanation of Gamow-Teller strength). This experimental measurement had a particularly large impact on the simulated fluorine production, because the measured Gamow-Teller strength distribution was found to be much lower than earlier shell-model calculations had predicted. The full impact on predictions of core-collapse supernovae fluorine production was a reduction of about 40% from the earlier estimates of Woosley *et al.* [6, 19]. An additional study by Austin *et al.* on the sensitivity of neutrino nucleosynthesis to variations in certain poorly-known reaction rates showed large fluctuations in fluorine production, suggesting that supernovae account for 25% to 75% of the solar fluorine abundance. With the lower fluorine production rates of Heger *et al.*, one cannot attribute a solar fluorine abundance solely to core-collapse supernovae. On the experimental front, Federman *et al.* [24] set out to measure ν-process fluorine in stars that had formed in the remnants of known core-collapse supernovae, but they did not see any evidence of enhanced fluorine abundances. The revised, significantly lower theoretical predictions of fluorine abundance and the lack of direct experimental evidence for

neutrino nucleosynthesis of fluorine indicate that different methods of fluorine production should be considered.

The reaction investigated in this dissertation, ^{19}F(t,^{3}He)^{19}O*, is most relevant to supernova environments. However, the method of fluorine production examined here differs significantly from the traditional neutrino nucleosynthesis scenario described above. Instead, this dissertation seeks to examine the possibility that fluorine is produced by neutron capture on ^{18}O to form ^{19}O, followed by a β-decay to ^{19}F:

$$^{18}\mathrm{O}(n,\gamma)^{19}\mathrm{O}(\beta^{-})^{19}\mathrm{F}. \tag{1.3.1}$$

The isotope ^{18}O is already produced primarily during helium-burning in the massive stars that are the progenitors of core-collapse supernovae [5]. The neutrons needed for this process could come from the supernova explosion itself. Core-collapse supernovae have the potential to emit sufficient quantities of neutrons for r-process nucleosynthesis to occur [3, 5], so there is potential for some ^{19}O to form and decay to ^{19}F during the supernova explosion.

Supernovae are particularly relevant to the ^{19}F(t,^{3}He)^{19}O* reaction because of the high temperatures achieved during the explosion. At these high temperatures, a significant portion of ^{19}O will achieve equilibrium in the very low-lying first excited state at 0.096 MeV, making it possible to β-decay from this excited state in ^{19}O* to ^{19}F. This is interesting because β-decay between the ground state of ^{19}O and the ground state of ^{19}F is forbidden (the spin-parity assignment of the ^{19}O ground state is $J^{\pi} = \frac{5}{2}^{+}$, while the spin-parity assignment of the ^{19}O ground state is $J^{\pi} = \frac{1}{2}^{+}$ [25]). However, the low-lying excited state in ^{19}O at 0.096 MeV has a spin and parity of $J^{\pi} = \frac{3}{2}^{+}$, which means that β-decay from this 0.096 MeV excited state in ^{19}O to the ground state of ^{19}F is allowed (see Figure 1.2).

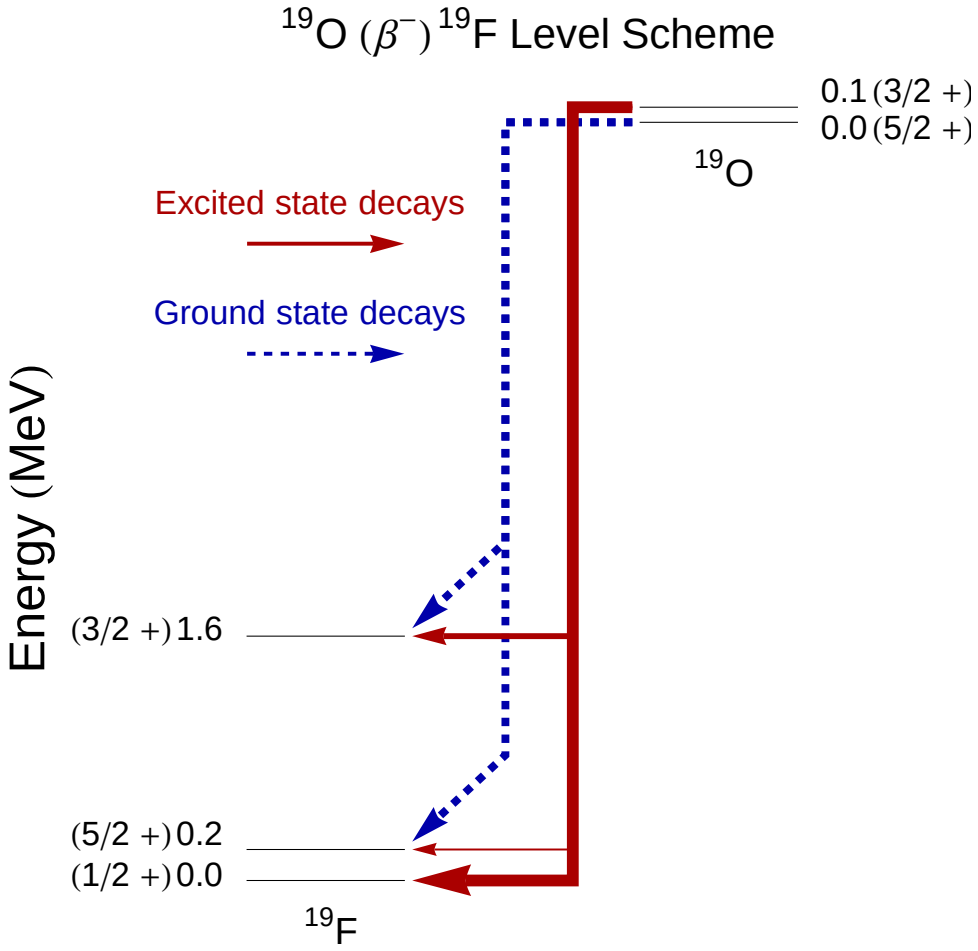

Figure 1.2: This level scheme depicts the allowed β-decays from ^{19}O to ^{19}F. Each arrow represents an allowed β-decay, while the thickness of the arrow roughly corresponds to the expected branching ratio (thicker arrows signify more probable transitions). The spin and parity for each level is indicated in parentheses. Information on these energy levels was taken from Tilley *et al.* [25].

This opens the door for a significant increase in the β-decay rate for ^{19}O in a supernova compared to the β-decay rate that has been measured in laboratory conditions. The first excited state of ^{19}O decays to the ground state by γ-ray emission in roughly 1 ns, so it isn't viable to measure the excited state β-decay through a direct experiment. Chernyhk *et al.* [26] performed a theoretical calculation to estimate the reaction rate increase that occurs when the 0.096 MeV state in ^{19}O is taken into account. Their calculations suggested that the ^{19}O$(\beta^-)^{19}$F β-decay rate might increase by a factor of three at high stellar temperatures, which indicates that this reaction is an excellent candidate for further experimental investigation. In Section 4.3.3 of this dissertation, the strength of the transition from the 0.096 MeV state of ^{19}O to the ground state of ^{19}F is extracted experimentally through study of the ^{19}F$(t,^3$He$)^{19}$O* reaction.

1.4 Wolf-Rayet Star Production of Fluorine

A different astrophysical site proposed for fluorine nucleosynthesis is the Wolf-Rayet star [27] (see Figure 1.3). A Wolf-Rayet star is a type of hot, giant star characterized by powerful stellar winds. These stars typically have temperatures above 30,000 K and have 10 to 25 times the mass of the Sun (but they are occasionally much more massive) [28]. The distinctive stellar winds of a Wolf-Rayet star are driven by photons transferring momentum via absorption to material in the outer atmosphere of the star. This radiative pressure drives very high winds that in turn remove large quantities of material from the star: winds of up to 6000 $\frac{km}{s}$ have been measured, and calculations predict that the winds from Wolf-Rayet stars eject material greater than the mass of the Earth in a year. This mass-loss mechanism makes Wolf-Rayet stars ideal candidates for fluorine production; any fluorine that is produced by

Figure 1.3: This image shows a Wolf-Rayet star, WR124. It is surrounded by a nebula, M1-67, that was formed from material ejected by the Wolf-Rayet star's powerful winds. Image credit: ESO [17].

the star via helium-burning can be ejected into the interstellar medium by high stellar winds before it is destroyed by α-capture.

In Wolf-Rayet stars, fluorine production occurs during early phase helium core burning [27]. In stars that are burning helium, fluorine is destroyed via the $^{19}\mathrm{F}(\alpha,p)^{22}\mathrm{Ne}$ reaction, typically near the end of the helium-burning phase. However, the high stellar winds of a Wolf-Rayet star preserve the fluorine by sweeping much of it out into the interstellar medium before it can be destroyed in α-capture. In the early helium burn phase, fluorine production is accomplished via the chains [27]:

$$^{14}\mathrm{N}(\alpha,\gamma)^{18}\mathrm{F}(\beta^{+})^{18}\mathrm{O}(p,\alpha)^{15}\mathrm{N}(\alpha,\gamma)^{19}\mathrm{F}, \tag{1.4.1}$$

$$^{14}\mathrm{N}(\alpha,\gamma)^{18}\mathrm{F}(n,p)^{18}\mathrm{O}(p,\alpha)^{15}\mathrm{N}(\alpha,\gamma)^{19}\mathrm{F}, \text{ and} \tag{1.4.2}$$

$$^{14}\mathrm{N}(\alpha,\gamma)^{18}\mathrm{F}(n,\alpha)^{15}\mathrm{N}(\alpha,\gamma)^{19}\mathrm{F} \tag{1.4.3}$$

with neutrons and protons produced in the reactions $^{13}\mathrm{C}(\alpha,n)^{16}\mathrm{O}$ and $^{14}\mathrm{N}(n,p)^{14}\mathrm{C}$, respectively. The first chain, Equation 1.4.1, is the dominant fluorine-producing reaction in Wolf-Rayet stars.

Simulations by Meynet and Arnould [27] supported the theory that Wolf-Rayet stars could create a fluorine overabundance. In particular, Meynet and Arnould found that Wolf-Rayet stars with masses ranging from 40 to 85 times the mass of the Sun and with metallicity similar to the Sun would exhibit the highest fluorine yields. Lower metallicities lead to the stars burning off the fluorine before stellar winds can carry it away. Higher metallicities and higher masses lead to helium-burning cores that are too small to be uncovered by stellar winds, so the fluorine cannot escape into the interstellar medium before it is destroyed. These simulations indicated that Wolf-Rayet stars could potentially account for the solar abundance of fluorine, and there were even some concerns expressed that the simulations could predict too high of a solar fluorine abundance. The aforementioned galactic chemical evolution model employed by Renda *et al.* [20] indicated that Wolf-Rayet stars were needed to match experimentally observed overabundances of fluorine, along with neutrino nucleosynthesis and AGB star production of fluorine.

Later, Palacios, Arnould, and Meynet revisited these Wolf-Rayet simulations of fluorine abundance [29]. Updated models of Wolf-Rayet stars and updated nuclear reaction rates triggered the re-examination. The updated stellar models indicated a significant reduction in expected mass loss, meaning that more fluorine will be burned up in α-capture and less will escape into the interstellar medium. Note that neutron densities in Wolf-Rayet stars are considered negligible, so the reaction $^{19}\mathrm{F}(\alpha,p)^{22}\mathrm{Ne}$ is considered the only significant source

of fluorine destruction. These mass loss changes lead to a decrease in fluorine production in Wolf-Rayet stars by as much as a factor of 30. The authors note, however, that these simulations are very sensitive to the rate of $^{19}\mathrm{F}(\alpha, p)^{22}\mathrm{Ne}$ and to mass loss rates that may be underestimated in this model. If these simulations prove correct, Wolf-Rayet stars are not a significant source of galactic fluorine production. However, the rate of $^{19}\mathrm{F}(\alpha, p)^{22}\mathrm{Ne}$ was recently measured by Ugalde *et al.* [30] and they recommend a rate that is an order of magnitude lower than the rate used in Palacios *et al.*, which would lead back to higher fluorine abundances in Wolf-Rayet stars.

Observationally, there is no direct measurement of fluorine in the stellar winds of a Wolf-Rayet star. However, there are some measurements that indirectly support the Wolf-Rayet production of fluorine. Observations of red giants in the Large Magellanic Cloud and in the globular cluster ω Centauri by Cunha *et al.* [21] show a link between fluorine abundance and metallicity. This link is predicted by the Wolf-Rayet simulations and by neutrino nucleosynthesis models of fluorine. Such a link between metallicity and fluorine abundance is not predicted by the AGB star models of fluorine production that will be discussed in greater detail later in this chapter. Later observations of red giants in the Galactic bulge, also by Cunha *et al.* [22], supported Wolf-Rayet fluorine production over neutrino or AGB production. These Galactic bulge red giants had a stronger link between metallicity and fluorine abundance than could be explained through Heger *et al.*'s [6] neutrino nucleosynthesis calculations, and had no overabundance of the *s*-process elements that are expected from AGB star fluorine production. A study of fluorine abundances in planetary nebulae by Zhang *et al.* [11] found one planetary nebula with both a Wolf-Rayet central star and a high fluorine overabundance. This particular Wolf-Rayet star planetary nebula deviated significantly from the trend of the other planetary nebulae observed in Zhang *et al.*'s study,

in that it had a high abundance of fluorine and a high metallicity whereas the general trend among the nebulae was a decrease in fluorine with higher metallicity. These observations provide some qualitative support for Wolf-Rayet nucleosynthesis of fluorine, but lack a strong quantitative argument.

The picture for fluorine production in Wolf-Rayet stars is thus anything but clear. There is certainly room for Wolf-Rayet stars to play an important role in fluorine nucleosynthesis. However, updated models for Wolf-Rayet fluorine production are needed in light of Ugalde *et al.*'s measurement of the $^{19}\mathrm{F}(\alpha,p)^{22}\mathrm{Ne}$ rate.

The measurements that are discussed in this dissertation are not expected to have an impact on fluorine nucleosynthesis in Wolf-Rayet stars. The temperatures relevant to fluorine production via helium-burning ($T \leq 0.2$ GK) are too low for any significant amount of $^{19}\mathrm{O}$ to occupy an excited state (see Sections 1.3 and 5.1 for more details). Additionally, the low neutron densities of Wolf-Rayet stars mean that they are the least likely of the three major sites proposed for fluorine production to undergo significant rates of the alternative fluorine production process, $^{18}\mathrm{O}(n,\gamma)^{19}\mathrm{O}(\beta^-)^{19}\mathrm{F}$.

1.5 Fluorine Found in AGB Stars

Direct observational evidence of fluorine abundances greater than the solar abundance was first recorded in asymptotic giant branch (AGB) stars by Jorissen *et al.* [8]. This discovery spurred much of the activity in the field of fluorine nucleosynthesis in the last two decades. AGB stars are cool, red giants that eject mass into the interstellar medium as they burn (see Figure 1.4). Stars with a mass less than roughly 9 times the mass of the Sun will go through an AGB phase as they near the end of their life. As an AGB star dies, the mass

Figure 1.4: This image shows the planetary nebula NGC 5189. Planetary nebulae like this one are formed when an asymptotic giant branch (AGB) star loses its outer layers. Many such nebulae are roughly spherical, giving rise to images that look like giant planets (hence the name "planetary" nebula). This one has a more complex shape that resembles a spiral. Image credit: ESO [17].

emitted forms a planetary nebula, and the core that remains behind becomes a white dwarf. AGB stars have an inert, electron-degenerate core comprised of carbon and oxygen. This core is surrounded by a helium-burning shell, which in turn is surrounded by a hydrogen-burning shell, and the outermost layer of the star forms a convective envelope [28, 30]. Fluorine nucleosynthesis occurs in the helium-burning shell of the AGB star. The region between the hydrogen- and helium-burning shells is referred to as the intershell. The two burning regions are largely isolated from each other by the intershell, but the complicated stellar dynamics of AGB stars allow for material from the hydrogen shell to occasionally be mixed into the helium-burning region, introducing protons that play an important role in the fluorine nucleosynthesis process [8]. Some protons in the helium shell are also generated by the

Type	Description
K	Orange stars slightly cooler than the Sun.
M	Cool, red stars.
MS	Intermediate AGB star with more carbon than M stars and less than S stars.
S	AGB star rich in s-process elements, with more carbon than M stars and less than C stars.
SC	AGB star with more carbon than S stars. Abundance of carbon and oxygen is nearly equal.
C	Carbon-rich AGB stars.
J	Carbon AGB stars with high ^{13}C abundances.

Table 1.1: Brief descriptions of the stellar classifications that are relevant for a discussion of asymptotic giant branch stars.

$^{14}\mathrm{N}(n,p)^{14}\mathrm{C}$ reaction. The neutrons needed for the preceding reaction and other neutron captures in AGB stars are generated through the $^{13}\mathrm{C}(\alpha,n)^{16}\mathrm{O}$ reaction [8] and potentially through the $^{22}\mathrm{Ne}(\alpha,n)^{25}\mathrm{Mg}$ reaction [30, 31].

The study by Jorissen *et al.* [8] covered red giant stars of several different spectral types. Please refer to Table 1.1 for a brief definition of each spectral type. In this study, it was found that K and M stars have fluorine abundances consistent with the Sun. Slight overabundances were found in some MS and S stars, and high excesses of fluorine were observed in barium stars, SC stars, most C stars, some J stars, and a few MS or S stars. The excess fluorine abundances ranged as high as 100 times the solar fluorine abundance and frequently fell within the range of 3 to 30 times the solar fluorine abundance. However, Abia *et al.* [9, 32] recently released two re-evaluations of the fluorine abundances in several stars from the Jorissen *et al.* study. Abia *et al.*'s 2009 paper [9] looked at three C stars from the Jorissen *et al.* study and found much lower fluorine abundances that are consistent with solar fluorine abundance. Abia *et al.* examined in detail the differences between their measurement and Jorissen *et al.*, and found that the most likely culprit for the discrepancy

is contaminants. Jorissen *et al.*'s fluorine abundance measurements relied heavily on two specific spectral vibration-rotation absorption lines of the HF molecule that Jorissen *et al.* state are mostly free of contamination, but the study by Abia *et al.* used a model that showed significant contamination of these same lines in carbon-rich stars from $^{12}C^{14}N$ and $^{12}C^{12}C$ molecules. Abia *et al.*'s abundance measurements relied instead on a different vibration-rotation line of HF that their model indicated had no contamination [9].

Abia *et al.* released a 2010 paper [32] that covered a wider variety of AGB stars, including several J-type, SC-type, and C-type stars (see Table 1.1 for a description of these stellar classifications). This study also showed systematic reductions in the fluorine overabundances as compared to Jorissen *et al.*'s work. The revised fluorine abundances found by Abia *et al.* for J and C stars [32] are mostly consistent with the solar fluorine abundance [14]. However, Abia *et al.* still see a significant fluorine overabundance in SC stars. Both Jorissen *et al.*'s paper [8] and Abia *et al.*'s paper [32] note that the SC stars are unique in that they have a nearly equal amount of carbon and oxygen. This leads to nearly all the carbon and oxygen being bound up as CO molecules. In turn, very slight variations in carbon and oxygen abundances in SC star models result in large variations in the final molecular makeup predicted by the models, meaning that there is a far greater uncertainty associated with these SC star measurements than with other AGB stars. This casts considerable doubt as to whether the high fluorine abundances measured in SC stars are due to systematic errors or genuine enhancements.

Several other extrasolar abundance measurements of fluorine have been performed, but they also present conflicting information on how significant AGB stars are for fluorine production. In 2003, Cunha *et al.* [21] released a paper with fluorine abundance measurements of red giants in the Large Magellanic Cloud and in the globular cluster ω Centauri. They

found that the abundance of fluorine in the ω Centauri stars was well below the solar abundance and many of the Large Magellanic Cloud star abundances were slightly below the solar abundance. The ω Centauri stars are notable because they have high abundances of elements produced in the s-process. Since AGB stars are thought to be the primary production site for s-process elements, the high s-process abundance in ω Centauri stars implies that AGB stars played a significant role in their chemical evolution. If this is the case, the low fluorine abundances in ω Centauri stars suggests that AGB stars may not be strong contributors to fluorine production. In another paper published in 2008, Cunha *et al.* [22] found fluorine overabundances in red giants in the galactic bulge that had no s-process enrichment. Models predict that, in AGB stars, fluorine production and s-process element production should be correlated [33], so a lack of s-process enrichment suggests that the fluorine seen in the red giants observed by Cunha *et al.* is not produced by AGB stars.

Conversely, measurements of fluorine abundances in planetary nebulae by Zhang and Liu [11] show an enhancement of fluorine when compared with the solar fluorine abundance. Planetary nebulae are composed of the material ejected into the interstellar medium by AGB stars [1], so this measurement of fluorine overabundance provides evidence in favor of AGB stars as a fluorine production site. Werner *et al.* [12] found very high fluorine overabundances of up to 250 times the solar abundance in extremely hot, hydrogen-deficient post-AGB stars, which also supports the hypothesis that AGB stars are a fluorine production site. Pandey *et al.* [13] found high fluorine enhancements of about 100 times solar in a sample of cool extreme helium stars (hydrogen-deficient supergiants), which may have previously gone through an AGB star phase.

Jorissen *et al.* examined several different nuclear reaction paths that could produce ^{19}F

in an AGB star [8]. They concluded that the most likely path for fluorine production is:

$$^{14}\mathrm{N}(\alpha,\gamma)^{18}\mathrm{F}(\beta^{+})^{18}\mathrm{O}(p,\alpha)^{15}\mathrm{N}(\alpha,\gamma)^{19}\mathrm{F}, \tag{1.5.1}$$

where neutrons and protons are produced via the $^{13}\mathrm{C}(\alpha,n)^{16}\mathrm{O}$ and $^{14}\mathrm{N}(n,p)^{14}\mathrm{C}$ reactions, respectively (see Figure 1.5). This is the reaction path that is discussed in most literature on fluorine production in AGB stars. However, Jorissen *et al.* also mention another potentially viable path for fluorine nucleosynthesis:

$$^{14}\mathrm{N}(\alpha,\gamma)^{18}\mathrm{F}(\beta^{+})^{18}\mathrm{O}(n,\gamma)^{19}\mathrm{O}(\beta^{-})^{19}\mathrm{F}, \tag{1.5.2}$$

where neutrons are produced via the $^{13}\mathrm{C}(\alpha,n)^{16}\mathrm{O}$ reaction, the $^{18}\mathrm{O}(\alpha,n)^{21}\mathrm{Ne}$ reaction, or the $^{22}\mathrm{Ne}(\alpha,n)^{25}\mathrm{Mg}$ reaction [30, 31] (see Figure 1.5). At the time of publication of Jorissen *et al.*'s paper, there were large uncertainties associated with the $^{18}\mathrm{O}(n,\gamma)^{19}\mathrm{O}$ rate. Such a fluorine production path would also require a large initial $^{18}\mathrm{O}$ content in the AGB star. This path is constrained by the competing $^{19}\mathrm{F}(n,\gamma)^{20}\mathrm{F}$ rate, which destroys the $^{19}\mathrm{F}$. Jorissen *et al.* expressed skepticism that the reactions $^{18}\mathrm{O}(n,\gamma)^{19}\mathrm{O}(\beta^{-})^{19}\mathrm{F}$ could play a significant role in AGB star fluorine nucleosynthesis because the rate of neutron capture on $^{18}\mathrm{O}$ is orders of magnitude lower than neutron capture on $^{19}\mathrm{F}$ [8].

The specific measurements that are discussed in this dissertation are not expected to have an impact on fluorine nucleosynthesis in AGB stars. The temperatures relevant to fluorine production via helium-burning ($T \leq 0.2$ GK) are too low for any significant amount of $^{19}\mathrm{O}$ to occupy an excited state (see Sections 1.3 and 5.1 for more details). However, the broader process of $^{19}\mathrm{O}(\beta^{-})^{19}\mathrm{F}$ (see Figure 1.5) as a potential source of fluorine in AGB stars has not

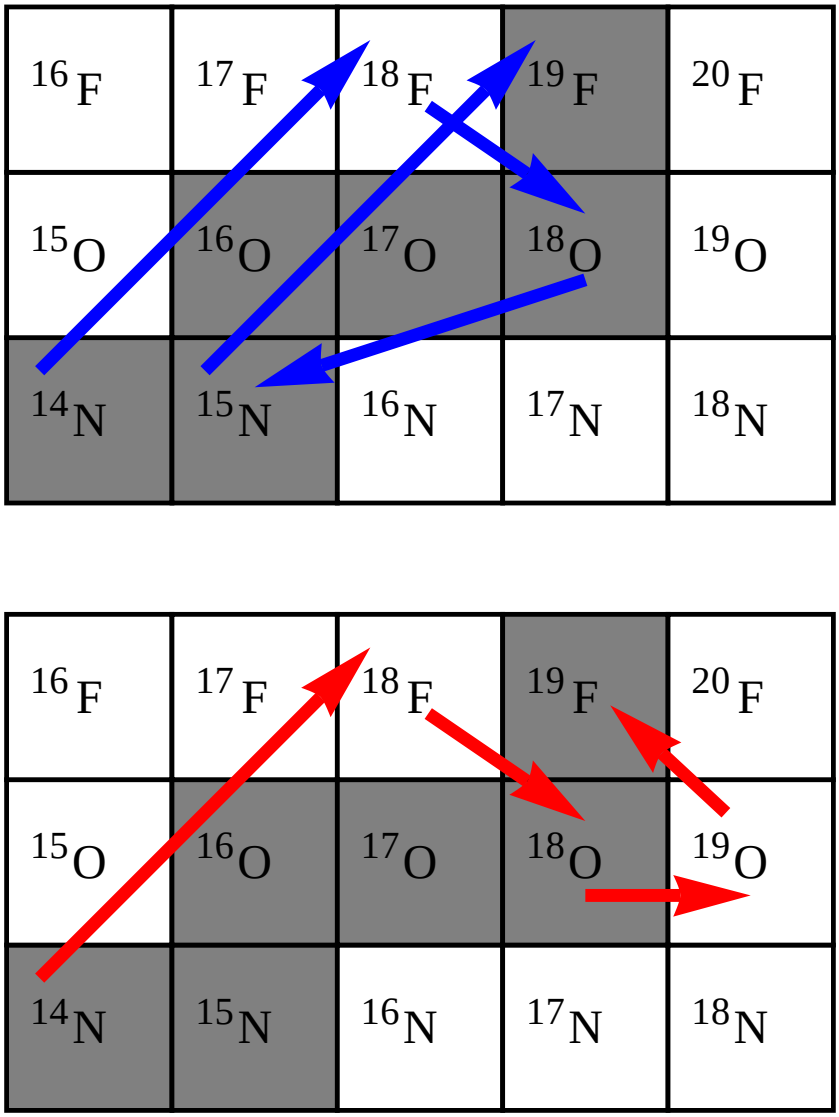

Figure 1.5: Nuclear paths for fluorine nucleosynthesis in AGB stars. Grayed boxes indicate a stable isotope in this slice of the chart of nuclides. The blue path in the top figure corresponds to Jorissen *et al.*'s primary reaction path. The red path in the bottom figure is the alternative path involving $^{19}\mathrm{O}(\beta^-)^{19}\mathrm{F}$ discussed in the text.

received attention in modern AGB nucleosynthesis calculations. Recent experimental developments suggest that this alternate reaction path deserves renewed scrutiny: a new measurement of the $^{19}\mathrm{F}(n,\gamma)^{20}\mathrm{F}$ rate by Uberseder *et al.* [34] indicates a lower cross section than prior estimates, a recalculation of the $^{22}\mathrm{Ne}(\alpha,n)^{25}\mathrm{Mg}$ rate by Karakas *et al.* [31] reduces uncertainties on this reaction, and a measurement of $^{19}\mathrm{F}(\alpha,p)^{22}\mathrm{Ne}$ rate by Ugalde *et al.* [30] indicates an order of magnitude lower cross section than prior measurements. These small shifts all favor higher abundances of fluorine and better conditions for β-decay from $^{19}\mathrm{O}$. The $^{19}\mathrm{O}(\beta^-)^{19}\mathrm{F}$ process should be included in future fluorine nucleosynthesis calculations simply to determine its contribution (if any) to AGB star fluorine production.

Chapter 2

Theory

The primary goal of this research is to measure the Gamow-Teller strength distribution for transitions from ^{19}F to ^{19}O via the ^{19}F(t,^{3}He)^{19}O* charge-exchange reaction. This Gamow-Teller strength distribution will be used to calculate a weak decay rate for the ^{19}O*(β^-)^{19}F reaction for use in the astrophysics application discussed in Chapter 1. This chapter explains the theoretical concepts that form the foundation of the ^{19}F(t,^{3}He)^{19}O* measurement. In addition to covering relevant theoretical arguments, this chapter will also discuss the computer programs used to perform theoretical physics calculations needed in the data analysis for Chapter 4.

2.1 Gamow-Teller Strength

When a nucleus undergoes β^--decay, it converts one neutron into a proton and emits an electron and antineutrino in the process [2]:

$$^{19}_{8}\mathrm{O}_{11} \rightarrow ^{19}_{9}\mathrm{F}_{10} + e^- + \bar{\nu}_e. \tag{2.1.1}$$

A β-decay involves a unit change in isospin ($\Delta T = 1$); this isospin change is represented by the isospin operator τ. For the case of β^--decay, this is specifically an isospin-lowering process represented by the operator τ_-. There are two separate classes of β-decay transitions:

Gamow-Teller and Fermi. Gamow-Teller transitions occur when the ejected electron and antineutrino have parallel spins. This means that the transition has a unit change in spin ($\Delta S = 1$); such a spin transfer is represented by the spin operator σ, and the overall Gamow-Teller transition is then represented by the operator $\sigma\tau$. The corresponding β-decay transitions where the ejected electron and antineutrino are antiparallel ($\Delta S = 0$) are called Fermi transitions, which are represented simply by the operator τ.

Nuclear reactions that involve the exchange of a neutron for a proton, or vise versa, are called change-exchange reactions. The simplest example is an (n, p) or (p, n) reaction, but more complex probes such as (t,^{3}He) and (^{7}Li,^{7}Be) can also be used. These reactions are also isovector transitions ($\Delta T = 1$) like β-decays. In cases where there is a change in spin but no change in orbital angular momentum ($\Delta S = 1$, $\Delta L = 0$), these strong-force mediated reactions can also be represented by the $\sigma\tau$ operator and connect the same states as allowed transitions in the β-decay mediated by the weak force. Under the right circumstances, the cross section of a nuclear charge-exchange reaction is proportional to the strength of the Gamow-Teller transition. This allows for an extraordinary situation where transition strengths associated with the weak force can be studied directly in reactions mediated by the strong force. Therefore, charge-exchange reactions like (t,^{3}He) can be used to study Gamow-Teller β-decay transitions that are inaccessible to direct β-decay studies because of Q-value limitations.

A significant amount of research has gone into establishing a firm relationship between various charge-exchange reaction cross sections and Gamow-Teller strengths. Taddeucci *et al.* [35] performed the first detailed investigation of the relationship between weak transition strengths and (p, n) cross sections at intermediate beam energies (120–200 MeV). In Reference [35], they established a proportionality called a unit cross section ($\hat{\sigma}_{\mathrm{GT}}$) between

Gamow-Teller strengths and the (p, n) reaction cross section at zero momentum transfer in the Eikonal approximation. This proportionality equation is written as:

$$\frac{d\sigma}{d\Omega}(q = 0) = KN^D|J_{\sigma\tau}|^2 \left(B[GT]\right) = \hat{\sigma}_{\mathrm{GT}} \left(B[GT]\right), \tag{2.1.2}$$

where $\frac{d\sigma}{d\Omega}(q = 0)$ represents the reaction cross section at zero momentum transfer, B[GT] denotes Gamow-Teller strength, and $KN^D|J_{\sigma\tau}|^2$ is the factorization of the unit cross section ($\hat{\sigma}_{\mathrm{GT}}$) proportionality coefficient under the Eikonal approximation. In that factorization, K represents a kinematic factor (see also Figure 2.2). N^D is a distortion factor that is defined by the ratio of distorted-wave to plane-wave cross sections; it accounts for the distortion of the incoming plane wave of the projectile and outgoing plane wave of the ejectile by the mean field of the target and residual nuclei, respectively. $|J_{\sigma\tau}|^2$ is the volume integral of the central $\sigma\tau$ component of the effective interaction between the nucleons in the target and projectile nuclei. Note that Gamow-Teller strength is defined here such that B[GT] = 3 for the decay of the free neutron.

This proportionality between Gamow-Teller strength and charge-exchange cross section holds only under certain conditions. As already mentioned, the charge-exchange cross section must be obtained for zero momentum transfer ($q = 0$), which requires that the cross section be extracted for zero reaction Q-value ($Q = 0$) and at a scattering angle of zero degrees ($\theta_{com} = 0°$). A direct, single-step charge-exchange reaction mediated by pion exchange is needed with no multi-step contributions from knock-on interactions; this occurs at intermediate beam energies above 100 MeV per nucleon [36, 37]. It has also been shown that the proportionality of Equation 2.1.2 can break down if the transition strength is very weak. This is likely caused by interference between the transition amplitudes mediated by

the $\sigma\tau$ and Tτ (tensor-τ) components of the effective interaction, which is discussed in more detail in Section 2.2. A more detailed discussion of the unit cross section is available in References [35, 38, 39].

Further studies of charge-exchange reactions and Gamow-Teller strength proportionalities have opened up additional experimental tools beyond the initial (p, n) probe. A similar relationship has been established for probes such as (^{7}Li,^{7}Be) reactions [40, 41], (^{3}He, t) reactions [38], and (t,^{3}He) reactions [42]. The significant similarities between (t,^{3}He) and (^{3}He, t) reactions and the availability of high-quality data sets for both types of reactions has permitted detailed examinations of the three factors (K, N^D, and $|J_{\sigma\tau}|^2$) in the unit cross section in Equation 2.1.2 [39].

To extract Gamow-Teller strengths from charge-exchange data, a value must be established for the unit cross section ($\hat{\sigma}_{\mathrm{GT}}$). There are two methods to accomplish this. In the method that is most frequently used, $\hat{\sigma}_{\mathrm{GT}}$ is determined through a direct calibration. A charge-exchange cross section is measured for a specific transition with a well-known Gamow-Teller strength from direct β-decay studies. Alternatively, it is possible to interpolate the unit cross section from other measurements on targets with similar masses where a unit cross section was established via the first method. This is useful when there is no well-known Gamow-Teller β-decay measurement available (as is the case for the ^{19}F$\rightarrow^{19}$O transition). In Reference [38], a phenomenological relationship between the unit cross section and nuclear mass (A) was established for (^{3}He, t) reactions at 140 MeV/nucleon in the region of $12 \leq A \leq 120$ (see Figure 2.1):

$$\hat{\sigma} = \frac{109}{A^{0.65}}. \tag{2.1.3}$$

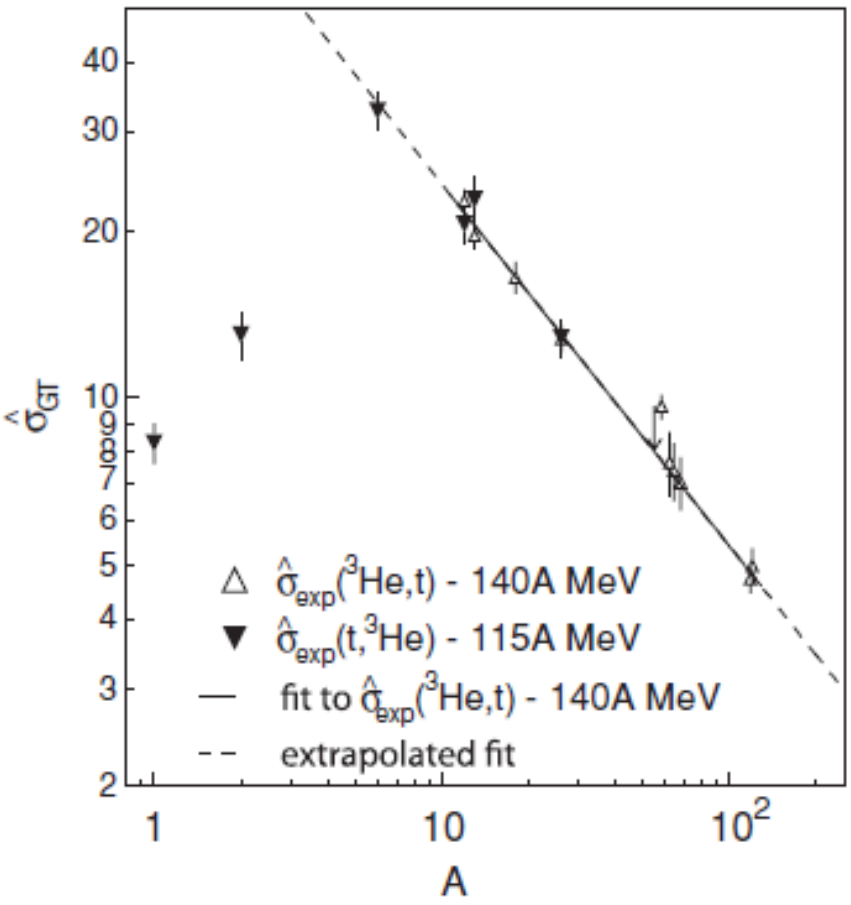

Figure 2.1: This figure shows the nuclear mass dependence (A) of the measured unit cross section ($\hat{\sigma}_{\mathrm{GT}}$) for several different (^{3}He, t) and (t,^{3}He) reactions. The solid line is a phenomenological fit to the (^{3}He, t) data for masses of $12 \leq A \leq 120$ that is discussed in detail in Reference [38]. The deviation from this fit at low masses is an expected phenomenon, dominated by the kinematic contribution (K) in Equation 2.1.2 (see also Figure 2.2). This figure was taken from Reference [39].

This equation has also been found to work well for (t,^{3}He) reactions at 115 MeV/nucleon [39] and was used to calculate a unit cross section for the present measurement of ^{19}F(t,^{3}He)^{19}O*

2.2 Distorted Wave Born Approximation

The spectrum for a charge-exchange reaction measurement is not restricted to only Gamow-Teller transitions. Several other transitions with different spin and angular momen-

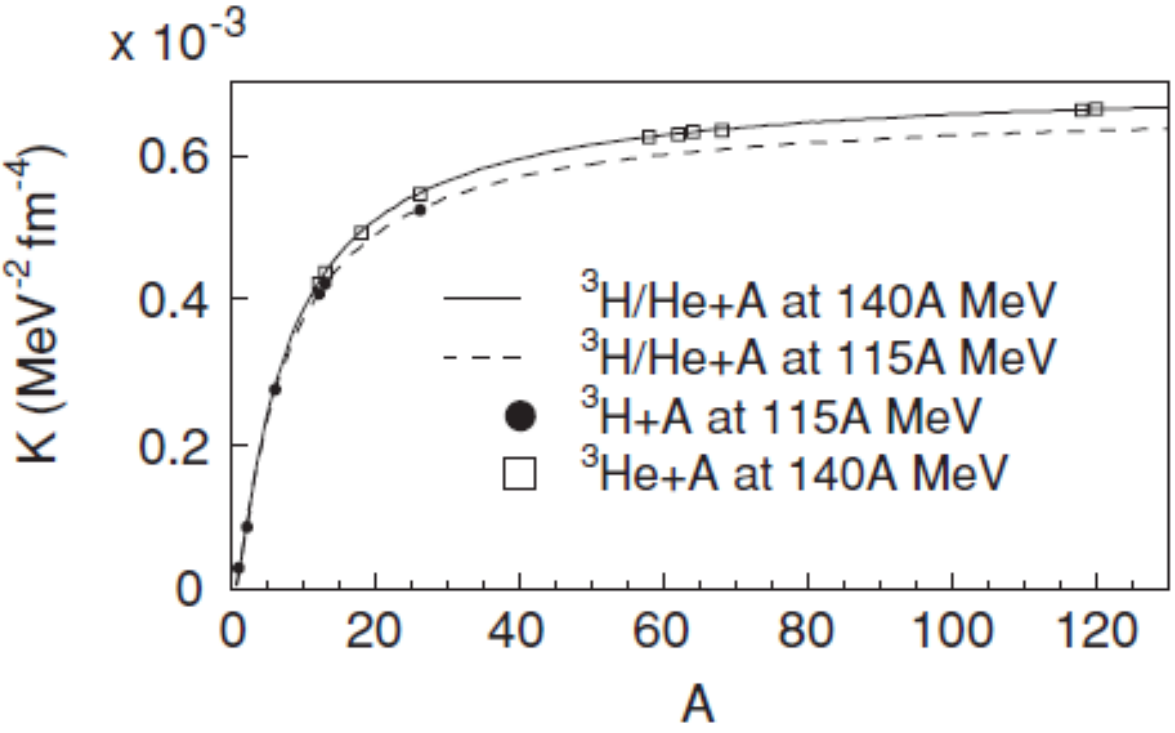

Figure 2.2: This figure shows the nuclear mass dependence (A) of the kinematic factor (K) in Equation 2.1.2 for the unit cross section ($\hat{\sigma}_{\mathrm{GT}}$) for several different (^{3}He$,t$) and (t,^{3}He) reactions. The solid line is defined as $K = \dfrac{E_i E_f k_f}{(\pi\hbar^2 c^2) k_i}$, where E_i and E_f are the reduced energies for the incoming and outgoing channel and k_i and k_f are the linear momentums of the projectile and ejectile. Since this line trends toward zero for low masses, it causes masses $A < 12$ to fall off the phenomonological fit described by Equation 2.1.3. The kinematic factor and its impact on the unit cross section is discussed in more detail in Reference [39]. This figure was taken from Reference [39].

tum transfers contribute as well. The allowed Gamow-Teller transitions ($\Delta S = 1,\ \Delta L = 0$) must be separated from these other contributions during the data analysis. As an example, transitions with a total angular momentum transfer of 1 ($\Delta L + \Delta S = \Delta J = 1$) can occur as Gamow-Teller ($\Delta S = 1,\ \Delta L = 0$) transitions or as quadrupole ($\Delta S = 1,\ \Delta L = 2$) transitions. The only way to achieve this separation of the Gamow-Teller transition is to use a reaction model; the reaction model can be used to predict the angular distributions for contributions to the spectra associated with different transfers of orbital angular momentum. The measured differential cross sections for the charge-exchange reaction are then decomposed on the basis of these theoretical calculations (see Section 4.3.1) so that the $\Delta L = 0$ component can be isolated. Further, once the $\Delta L = 0$ component of the measured differential cross sections are extracted, they must be extrapolated to zero momentum transfer ($q = 0$) so that the proportionality relationship in Equation 2.1.2 can be applied and Gamow-Teller strengths can be extracted. This procedure also requires theoretical reaction calculations, both to extrapolate from a finite reaction Q-value to $Q = 0$ and to quantify the cross section at a scattering angle of zero ($\theta_{com} = 0^{\circ}$), which then fulfills the zero linear momentum transfer condition.

As mentioned above, Tτ (tensor-τ) terms can further complicate matters for weak Gamow-Teller transitions due to interference between the transition amplitudes mediated by the $\sigma\tau$ and Tτ interactions. The angular distribution at forward scattering angles is not modified by this interference, but the proportionality in Equation 2.1.2 becomes uncertain. The effect is strongest for weak excitations [42, 43], where the tensor contribution can become the dominant term. The tensor contribution can be estimated through theory calculations.

The theoretical tool used for these reaction calculations was the three-part WSAW, FOLD, and DWHI code package [44]. Angular distributions were calculated with this code

package through a first order distorted wave Born approximation (DWBA) [45, 46, 47, 48]. In general, a reaction cross section can be expressed in terms of transition amplitudes (T_{fi}) from a DWBA calculation as:

$$\frac{d\sigma}{d\Omega} = \left(\frac{\mu}{2\pi\hbar^2}\right)^2 \left(\frac{k_f}{k_i}\right) |T_{fi}|^2, \tag{2.2.1}$$

where μ is the reduced energy, k_i is the incoming wave number, and k_f is the outgoing wave number [49]. The calculation of transition amplitudes requires several nuclear structure and nuclear reaction inputs. The FOLD code is the core of this reaction model package; it computes form factors, which contain information about the interaction between the projectile and target as well as nuclear structure information about relevant transitions. The WSAW code generates radial wave functions that are used in FOLD's calculation of form factors. The DWHI code uses the form factors computed by FOLD and optical potentials to calculate transition amplitudes and differential cross sections on the basis of the DWBA formalism.

The WSAW code is used to compute a set of single-particle radial wave functions (ϕ) for a two-body particle system, such as the target-recoil system. A potential with a Coulomb, Woods-Saxon, and spin-orbit term is input into the code for each single-particle state. Then radial wave functions for each single-particle state are determined by allowing the depth of the Woods-Saxon potential to vary while fitting the radial wave function to the Schrödinger equation such that it reproduces a set of input single-particle binding energies. The other parameters in the potential are fixed in the WSAW input file at the following values: diffuseness $a_0 = 0.65$ fm, Coulomb radius $r_c = 1.25$ fm, Woods-Saxon radius $r_0 = 1.25$ fm, spin-orbit potential depth coefficient $V_{SO} = 7.0$ MeV. The single-particle binding energies for the target-recoil system were calculated with the shell-model code OXBASH [50] us-

Model	E_b (MeV)	Model	E_b (MeV)
$^{18}\mathrm{O} + p(0s_{1/2})$	-29.6	$^{18}\mathrm{O} + n(0s_{1/2})$	-29.6
$^{18}\mathrm{O} + p(0p_{3/2})$	-17.9	$^{18}\mathrm{O} + n(0p_{3/2})$	-17.7
$^{18}\mathrm{O} + p(0p_{1/2})$	-13.3	$^{18}\mathrm{O} + n(0p_{1/2})$	-13.1
$^{18}\mathrm{O} + p(0d_{5/2})$	-5.9	$^{18}\mathrm{O} + n(0d_{5/2})$	-6.1
$^{18}\mathrm{O} + p(0d_{3/2})$	-1.0	$^{18}\mathrm{O} + n(0d_{3/2})$	-1.0
$^{18}\mathrm{O} + p(1s_{1/2})$	-3.1	$^{18}\mathrm{O} + n(1s_{1/2})$	-4.4
$^{18}\mathrm{O} + p(0f_{7/2})$	-1.0	$^{18}\mathrm{O} + n(0f_{7/2})$	-1.0
$^{18}\mathrm{O} + p(0f_{5/2})$	-1.0	$^{18}\mathrm{O} + n(0f_{5/2})$	-1.0
$^{18}\mathrm{O} + p(1p_{3/2})$	-1.0	$^{18}\mathrm{O} + n(1p_{3/2})$	-1.0
$^{18}\mathrm{O} + p(1p_{1/2})$	-1.0	$^{18}\mathrm{O} + n(1p_{1/2})$	-1.0
$^{18}\mathrm{O} + p(0g_{9/2})$	-1.0	$^{18}\mathrm{O} + n(0g_{9/2})$	-1.0

Table 2.1: This table lists the single-particle binding energies that were used as an input for the WSAW radial wave form calculation. The model column indicates the core nucleus and the added proton (left) or neutron (right) in the indicated single-particle level to form the ^{19}F or ^{19}O nucleus, respectively. These binding energies for the *spsdpf* model space were calculated using the Skyrme SK20 interaction [51] with the shell-model code OXBASH [50]. When the calculated binding energies were greater than -1.0 MeV, a value of -1.0 MeV was substituted to ensure that the generated wave functions were well-bound and the computations converged.

ing the Skyrme SK20 interaction [51]. The Skyrme SK20 interaction was selected for this application because it is valid over a wide range nuclei and thus allows for comparisons across a broad variety of charge-exchange reactions. The binding energies (E_b) used for the WSAW calculation on the ^{19}F–^{19}O system are listed in Table 2.1. The t–^{3}He system radial wave functions were computed from Variational Monte Carlo results [52, 42] instead of with WSAW.

The FOLD code produces form factors ($F(\vec{r})$) by double-folding the effective nucleon-nucleon interaction (V_{eff}) of Love and Franey [37, 53] at 140 MeV/nucleon over the one-body transition densities of the projectile-ejectile and target-recoil systems. Form factors are a function of the distance between the target and projectile ($\vec{r}$). These form factors account for the composite nature of all the nuclei involved in the ^{19}F(t,^{3}He)^{19}O* reaction when the

DWBA is performed. The one-body transition densities describe the overlap between initial and final states in the projectile-ejectile and target-recoil systems. A one-body transition density serves as a weighting factor for each one-particle, one-hole transition, determined by the overlap between the initial and final nuclear states. One-body transition densities for the ^{19}F–^{19}O system were calculated in the *spsdpf*-shell model space with the WBP effective interaction [54] using the shell-model code OXBASH [50]. FOLD generates form factors from the radial wave functions generated in WSAW (ϕ), one-body transition densities, kinematic data, and spin-coupling information. Form factors are calculated with the equation [49]:

$$F(\vec{r}) = \sum \left\langle \Phi_e \Phi_r \middle| a^\dagger a c^\dagger c \middle| \Phi_p \Phi_t \right\rangle \left\langle \phi_e \phi_r \middle| V_{eff} \middle| \phi_e \phi_r \right\rangle, \tag{2.2.2}$$

where the subscripts of t, p, e, and r indicate the wavefunctions of the target, projectile, ejectile, and recoil particles respectively and the sum runs over all possible quantum numbers for the system. The portion of the equation represented by $\left\langle \Phi_e \Phi_r \middle| a^\dagger a c^\dagger c \middle| \Phi_p \Phi_t \right\rangle$ contains the one-body transition densities as well as spin-coupling terms and creation and annihilation operators.

The DWHI code uses the form factors found with FOLD calculations to compute transition amplitudes (T_{fi}) and then angular distributions $\left(\frac{d\sigma}{d\Omega}\right)$ through a DWBA calculation. Transition amplitudes for a specific transfer of spin (ΔS), total angular momentum (ΔJ), and orbital angular momentum (ΔL) are calculated from the following equation [49]:

$$T_{fi} = \left\langle \chi_f(\vec{k_f}, \vec{r}) \middle| F(\vec{r}) \middle| \chi_i(\vec{k_i}, \vec{r}) \right\rangle, \tag{2.2.3}$$

where $\chi_i(\vec{k_i}, \vec{r})$ and $\chi_f(\vec{k_f}, \vec{r})$ are the distorted waves for the initial and final states, respec-

	Real			Imaginary		
Channel	Depth (MeV)	Radius (fm)	Diffuseness (fm)	Depth (MeV)	Radius (fm)	Diffuseness (fm)
$^{19}\mathrm{F} + t$	-18.8	1.54	0.74	-36.3	0.89	0.96
$^{19}\mathrm{O}{+}^{3}\mathrm{He}$	-22.1	1.54	0.74	-42.66	0.89	0.96

Table 2.2: This table lists the Woods-Saxon optical model potential parameters used for the DWBA calculations. The parameters for the outgoing channel were measured in Reference [55] for the incoming channel of the $^{16}\mathrm{O}(^{3}\mathrm{He}, t)^{16}\mathrm{F}$ reaction at 140 MeV/nucleon. The parameters for the incoming channel were derived from the parameters of the outgoing channel as described in Reference [56].

tively. An optical potential is used in this calculation to account for the distortion effects of the nuclear mean field. Since there are no optical potentials available for the specific beam energy and reaction channels of this experiment, a suitable published optical potential from a similar reaction was used instead. The best optical model available for this purpose was found in Reference [55], in which Fujita *et al.* studied the $^{16}\mathrm{O}(^{3}\mathrm{He}, t)^{16}\mathrm{F}$ reaction at 140 MeV/nucleon. As part of their analysis, Fujita *et al.* determined the optical potential for the $^{16}\mathrm{O}{+}^{3}\mathrm{He}$ channel from elastic scattering data. The model chosen for this optical potential consisted of real and imaginary Woods-Saxon terms, and any error due to the choice of optical potential is expected to be negligible. The extracted parameters for the $^{16}\mathrm{O}{+}^{3}\mathrm{He}$ channel were used in the current analysis for the $^{19}\mathrm{O}{+}^{3}\mathrm{He}$ outgoing reaction channel. For the incoming channel of $^{19}\mathrm{F} + t$, the real and imaginary Woods-Saxon potential depths were scaled by a factor of 0.85, following the phenominological procedure described in Reference [56]. The Woods-Saxon optical model potential parameters used for the DWHI calculations are listed in Table 2.2. In addition to the optical model parameters, DWHI also takes spin and kinematic information as inputs, including reaction Q-values. The calculated transition amplitudes are then used to compute the desired differential cross section angular distributions through Equation 2.2.1.

The differential cross section angular distributions produced by the WSAW/FOLD/DWHI code package were used during the data analysis in a multipole decomposition analysis (see Section 4.3.1). They were also used to extrapolate differential cross sections with finite linear momentum transfer to zero linear momentum transfer ($q = 0$). This extrapolation meets the necessary conditions for the determination of Gamow-Teller transition strengths using the unit cross section proportionality described in Section 2.1.

Chapter 3

Experiment

The goal of this dissertation is to extract the Gamow-Teller strength of the ^{19}F(t,^{3}He)^{19}O* reaction (see Section 2.1 for a detailed explanation of Gamow-Teller strength). This chapter will discuss the facility at which this experiment was performed and describe the experimental devices used to collect the data for this dissertation. A beam of tritons was impinged on a target that contained fluorine (CF_2). The charge-exchange reaction of interest, ^{19}F(t,^{3}He)^{19}O*, was selected for by triggering on ^{3}He ejectiles with a high-resolution spectrograph. The spectrograph recorded position, angles, timing, and energy loss data that are used in Chapter 4 to construct differential cross sections for the reaction over the excitation energy (E_x) range of 0 MeV $\leq E_x[^{19}\text{O}] \leq$ 16 MeV, and those differential cross sections are then used to calculate Gamow-Teller strengths.

This experiment is not the first measurement of the ^{19}F(t,^{3}He) reaction. Earlier work by Pinder *et al.* [57] measured the cross section of the ground and first excited state of ^{19}O produced by a (t,^{3}He) reaction with a 33 MeV beam of tritons. However, that data set did not provide enough information to investigate the astrophysics application discussed in Section 1.3. At the low beam energies used by Pinder *et al.*, many two-step (indirect) reactions occur; the proportionality relationship of Equation 2.1.2 discussed in Section 2.1 isn't valid under such conditions.

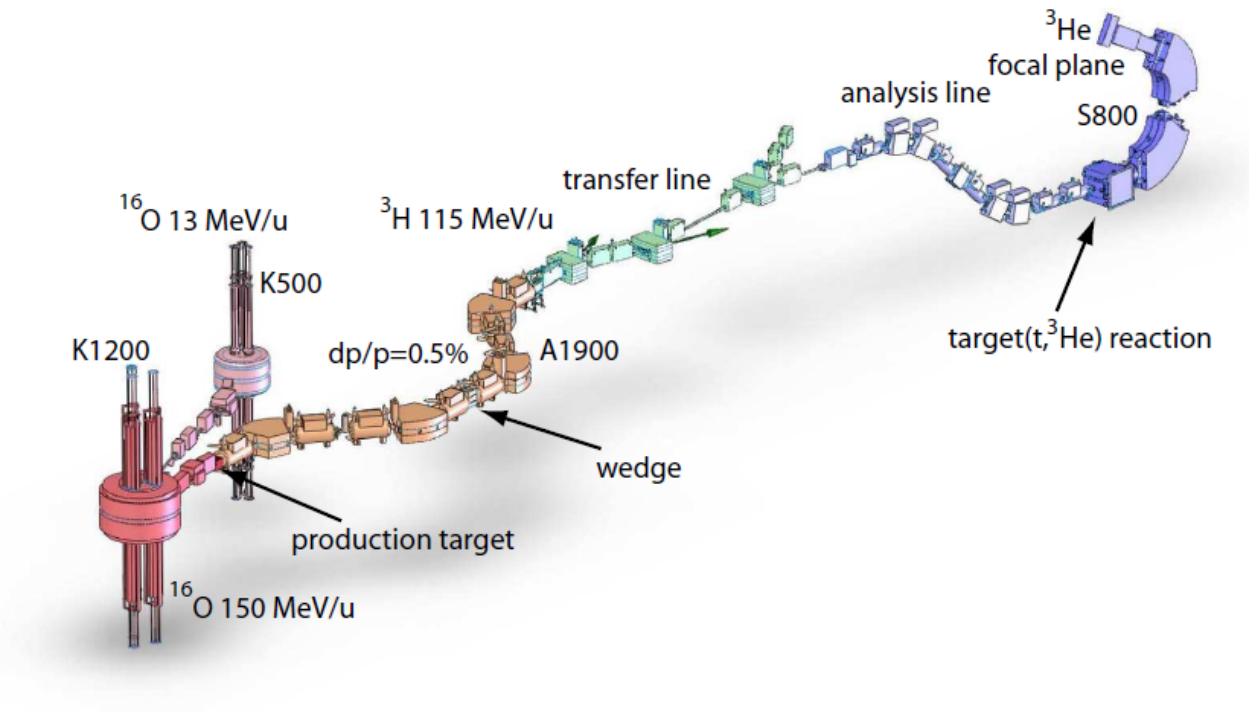

Figure 3.1: This is a schematic of the devices used in experiment e09053 at the NSCL. This figure shows the Coupled Cyclotron Facility (red), the A1900 fragment separator (orange), the transfer line between theA1900 and the S800 spectrograph (green), the S800 spectrograph analysis line (blue), and the S800 spectrograph (purple). For more details, refer to the text. Image taken from Reference [48].

3.1 Triton Beam Production

This experiment was performed at the Coupled Cyclotron Facility at the National Superconducting Cyclotron Laboratory (NSCL). The experiment was designated with the number e09053 and ran in February 2010. See Figure 3.1 for a schematic layout of the NSCL apparatuses used in this research.

The Coupled Cyclotron Facility [58, 59] consists of two superconducting cyclotrons (red section of Figure 3.1): the K500 cyclotron and the K1200 cyclotron. In this experiment, $^{16}O^{3+}$ ions from an Electron Cyclotron Resonance ion source were injected into the smaller of the two cyclotrons, the K500. The $^{16}O^{3+}$ ions underwent an initial acceleration to an

energy of 13 MeV/nucleon in the K500 cyclotron and were then injected through a coupling line into the larger K1200 cyclotron. Inside the K1200 cyclotron, the ions hit a thin carbon stripper foil that removed the remaining electrons, producing $^{16}O^{8+}$. This fully-ionized oxygen was accelerated in the K1200 cyclotron to an energy of 150 MeV/nucleon. It was then extracted from the K1200 and impinged on a beryllium production target to create a secondary radioactive beam through projectile fragmentation. A 3526 mg/cm^2 production target of ^{9}Be was used in this experiment to produce a 115 MeV/nucleon triton ($^3H^+$ or t) secondary beam. Prior research by Hitt *et al.* [60, 47] found that this method produces the highest triton beam rate at an energy appropriate for charge-exchange experiments ($>$ 100 MeV/nucleon) at the NSCL.

A wide variety of fragments are produced when primary beam impinges on the beryllium production target. To separate the desired secondary beam from all other fragments and from the remaining primary beam, the secondary beam is sent through the A1900 fragment separator [61, 62] (see Figure 3.2 for the layout of the A1900 fragment separator, which is also pictured in the orange section of Figure 3.1). The A1900 separator consists of four dipole magnets and eight quadrupole triplets and separates fragments by momentum. It has high momentum and angular acceptance ($\Delta p/p$ = 5% and $\Delta\Omega$ = 8 msr, respectively). It operates in an achromatic ion-optical mode, meaning that the final positions and angles of the output beam particles are independent of momentum. The first half of the A1900 fragment separator selects fragments with a specific magnetic rigidity: $B\rho = \gamma mv/q$ [62], where $B\rho$ is magnetic rigidity, γ is the Lorentz factor, m is mass, v is velocity, and q is charge. Further separation of fragments occurs when the beam passes through an energy degrader, often referred to as a wedge [61]. Fragments that enter the wedge with a fixed magnetic rigidity will emerge with magnetic rigidity that varies by atomic number due to

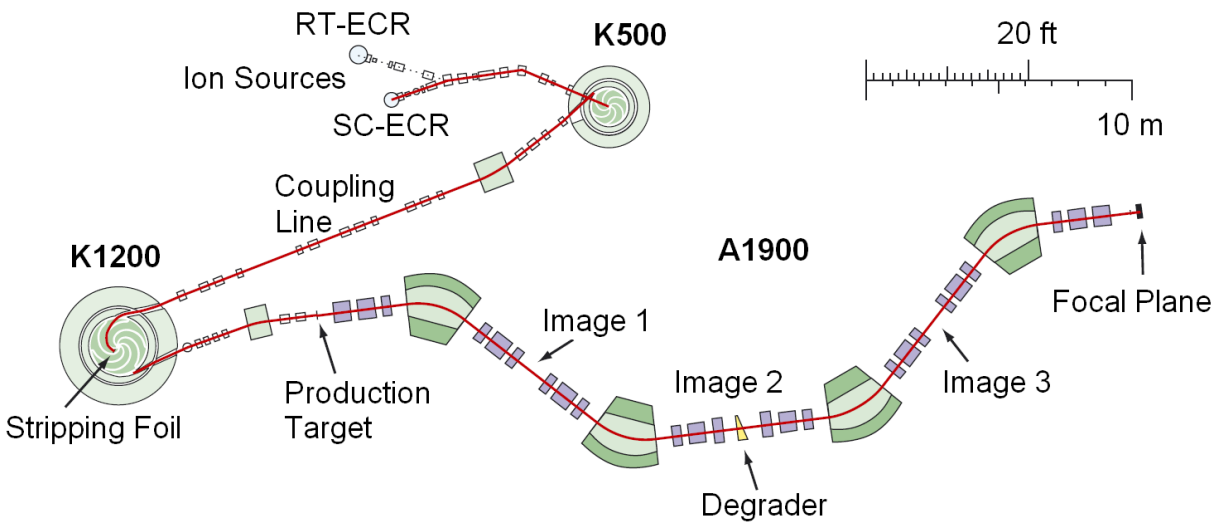

Figure 3.2: This figure shows a schematic of the A1900 fragment separator. This device separates the desired secondary beam isotope from other fragments. See the text for a detailed description of the separation process. Image taken from Reference [62].

differences in energy loss in the wedge. After the wedge, the A1900 fragment separator disperses the fragments at its focal plane, and slits are used to remove the contaminants by blocking particles with a momentum that varies too much from the desired isotope.

In this experiment, a 195 mg/cm^2 aluminum wedge was used in the A1900 fragment separator to remove the primary contaminants of the triton beam, ^{6}He and ^{9}Li. This method of purifying the triton beam with a wedge was first tested in experiment 06032 by C. J. Guess *et al.* [48]. Without this wedge, the triton beam had a purity of about 85%, and the ^{6}He contamination created a background at the S800 spectrograph focal plane by breaking up into $^3\mathrm{He} + 3n$ at the reaction target. With the wedge inserted, all background from these ^{6}He events was eliminated. The slits that purify the triton beam after the wedge were set to restrict the momentum acceptance to $\Delta p/p = 0.5\%$. The final purified triton secondary beam was directed through a transfer line (green section of Figure 3.1) toward the experimental station.

There are two beam monitors of note near the cyclotrons and the A1900 that were used

in the data analysis for this experiment. These beam monitors did not intercept the triton beam, but they produced signals that were proportional to the triton beam intensity. The first probe, labeled Z001I-C, was a non-intercepting current probe located immediately after the K1200 cyclotron that measured the primary beam intensity. The second probe, labeled Z026R-C, was a copper bar located in the first dipole magnet of the A1900. It acted as a Faraday cup to measure the current of the unreacted primary beam that passed through the beryllium production target; the secondary triton beam was steered away from this probe by the dipole magnet. These beam current measurements, along with other data, were used to provide a relative scale for the secondary beam intensity on different reaction targets. This information was needed because there was no direct measurement of the secondary beam intensity available throughout the experiment. An estimate of the average absolute triton beam intensity from the well-known ^{12}C(t,^{3}He) cross section gave a rate of roughly 7×10^6 particles per second. This rate was 30% lower than in experiment 06032 due to problems with the triton beam tuning.

3.2 Targets

Four different reaction targets were used in the course of this experiment at the pivot point of the S800 spectrograph. The reaction target of primary interest for this dissertation was an 11.2 mg/cm^2 thick piece of CF_2, commonly known as Teflon. The goal of using this target was to study the ^{19}F(t,^{3}He)^{19}O* reaction. CF_2 was selected as the fluorine target material because it has a high fluorine content and is easy to obtain. No notable contamination of the CF_2 target was detected. A separate CH_2 reaction target with a thickness of 10 mg/cm^2 was used to provide both calibration data and information on the ^{12}C background events

produced by the carbon in the CF_2 target. The third target, a piece of aluminum coated with ZnS (which fluoresces when hit by beam), was used as a viewer to verify that the beam spot was properly aligned on the target at the pivot point. The fourth reaction target was a foil of isotopically purified ^{56}Fe. Data taken on the ^{56}Fe target was analyzed in detail in a separate study by Y. Shimbara *et al.* [63], and is only used in this dissertation for a few calibrations.

In prior charge-exchange measurements at the NSCL, a large vacuum chamber with a remote-controllable target ladder was used to implement easy transitions between different reaction targets. The large vacuum chamber was not available for this experiment, so all reaction target changes were done manually instead. Since manual target changes are time-consuming, this means that there were limited opportunities to perform calibration checks with the CH_2 target and to inspect the beam spot at the S800 pivot point. However, enough calibration runs were performed that this restriction did not add any significant error to the data taken on the CF_2 reaction target.

3.3 S800 Spectrograph

The experimental station used for this research was the S800 spectrograph [64, 65]. The S800 spectrograph is a high resolution and high acceptance device that uses superconducting magnets to measure the momentum of charged particles. It has two sections: the analysis line (light blue area in Figure 3.1), and the high acceptance spectrograph with focal plane detectors (purple area in Figure 3.1). The S800 spectrograph focal plane detectors provide timing, position, and energy loss data for the reaction ejectile. This information is used to reconstruct the events at the reaction target.

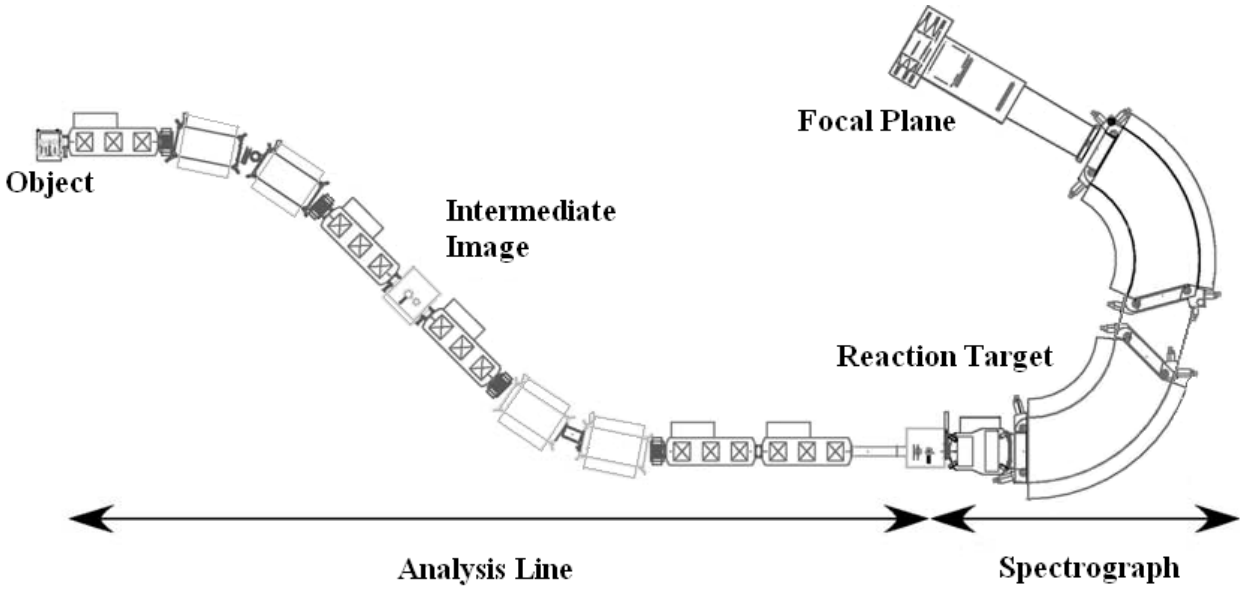

Figure 3.3: This figure shows the layout of the S800 spectrograph and its analysis line. The triton beam entered the S800 analysis line at the object position and was momentum-dispersed as it traveled through the analysis line so that it was fully dispersed at the reaction target. When the desired (t,^{3}He) reaction occurs in the target, the ^{3}He ejectiles are bent through the S800 spectrograph and then measured by detectors at the focal plane. Image adapted from a figure in Reference [65].

The analysis line of the S800 spectrograph (see Figure 3.3) is composed of four dipole magnets and five quadrupole triplet magnets. Two distinct operating modes are available for the device. In focused mode, the analysis line is achromatic, which produces a chromatic image at the focal plane. Focused mode provides high momentum acceptance of beam particles at the expense of energy resolution in the measured ejectiles. In dispersion matching mode, the entire system of analysis line and spectrograph is achromatic, meaning that the momentum spread of the beam at the beginning of the analysis line is ideally cancelled out at the focal plane. Thus the momentum variation that is measured at the focal plane is only due to the momentum transfer that took place in the reaction target. This mode provides better energy resolution for the ejectiles at the cost of lower momentum acceptance. The reduced momentum acceptance in dispersion matching mode occurs because the beam is

momentum-dispersed on the reaction target at the S800 spectrograph pivot point, and the S800 spectrograph dispersion is about 11 cm per 1% momentum spread. The layout of the analysis line and the S800 spectrograph cannot fully accommodate a very large beam spot, so in dispersion matching mode the momentum needs to be restricted to $\Delta p/p = 0.5\%$ to provide a manageable beam spot size (this corresponds to a beam spot roughly 5.5 cm tall) whereas focused mode can support a momentum spread of up to $\Delta p/p = 3\%$. Dispersion matching mode was used for this experiment because the high energy resolution was critical to reconstructing the reaction on an event-by-event basis. The magnetic rigidity ($B\rho$) of the analysis line was set to 4.8 Tm for this experiment.

The spectrograph itself (see Figure 3.3) consists of two quadrupole magnets and two dipole magnets that focus the reaction ejectiles onto a set of detectors at the focal plane. The magnetic rigidity set for the S800 spectrograph during this experiment was $B\rho = 2.3293$ Tm. The focal plane detectors suite contains two Cathode Readout Drift Chambers (CRDCs), an ion chamber, and a set of plastic scintillators [65]. At the time of this experiment, the focal plane detectors were undergoing an upgrade. As a result, the ion chamber was offline and the four plastic scintillators that are normally in the focal plane were replaced; both CRDCs were fully functional. This did not adversely affect the experiment. The ion chamber is not used for $(t,{}^3\mathrm{He})$ experiments because the ^{3}He ejectile has a low proton number ($Z = 2$), so it doesn't lose enough energy in the ion chamber fill gas to produce a useful signal [47]. The four plastic scintillators were in the process of being replaced with a more sophisticated hodoscope detector made of 32 crystal CsI(Na) scintillators [66] and a single new thin plastic scintillator. The new thin plastic scintillator had been fully installed when this experiment ran and provided sufficient timing and energy loss data to replace the old scintillators.

The two Cathode Readout Drift Chambers (CRDCs) measure the dispersive and non-

dispersive positions of particles [64]. They are separated by a distance of 1.073 meters along the beam path so that the two sets of position measurements can be used to reconstruct the flight path angle of particles. Each CRDC acts as single wire drift detector [64, 67]. The drift chamber is filled with a gas mixture of 80% CF_4 and 20% C_4H_{10}. This gas mixture has low aging characteristics, high drift velocity, and low avalanche spread. A set of 225 cathode pads are arrayed along the dispersive direction and a single anode wire runs parallel to them (see Figure 3.4). When an ejectile enters the CRDC, the gas is ionized, creating electron - ion pairs. The electrons drift quickly along the electric field toward the anode wire. As the electrons reach the anode wire, they induce a signal on both the anode and the nearby cathode pads [67]. The amount of signal induced on each cathode pad will vary with the distance from the ejectile dispersive position, so the CRDC determines the dispersive position by performing a Gaussian fit to the current measured on each pad (see inset on Figure 3.4). The non-dispersive position is determined by the drift time of electrons; the detector measures the time difference between the data acquisition trigger (a signal from the plastic scintillator) and the collection of electrons on the anode wire.

The CRDCs give a position resolution of approximately 0.5 mm in both directions, which corresponds to an ideal scattering angle resolution of 2 mrad. In dispersion matching mode, the ideal energy resolution of the S800 spectrograph for reconstructed events is 1 part in 10,000 [65]. In practice, experiments performed with the S800 spectrograph and radioactive beams usually obtain a scattering angle resolution of 10 mrad and an energy resolution of up to 1 part in 2,000. The difference between the ideal and actual resolution is due to factors external to the S800 spectrograph, such as beam spot size and reaction target thickness. See Sections 4.1.2, 4.1.3, and 4.1.4 for a detailed description of the extraction of reaction data from CRDC measurements and a discussion of the resolutions obtained in this experiment.

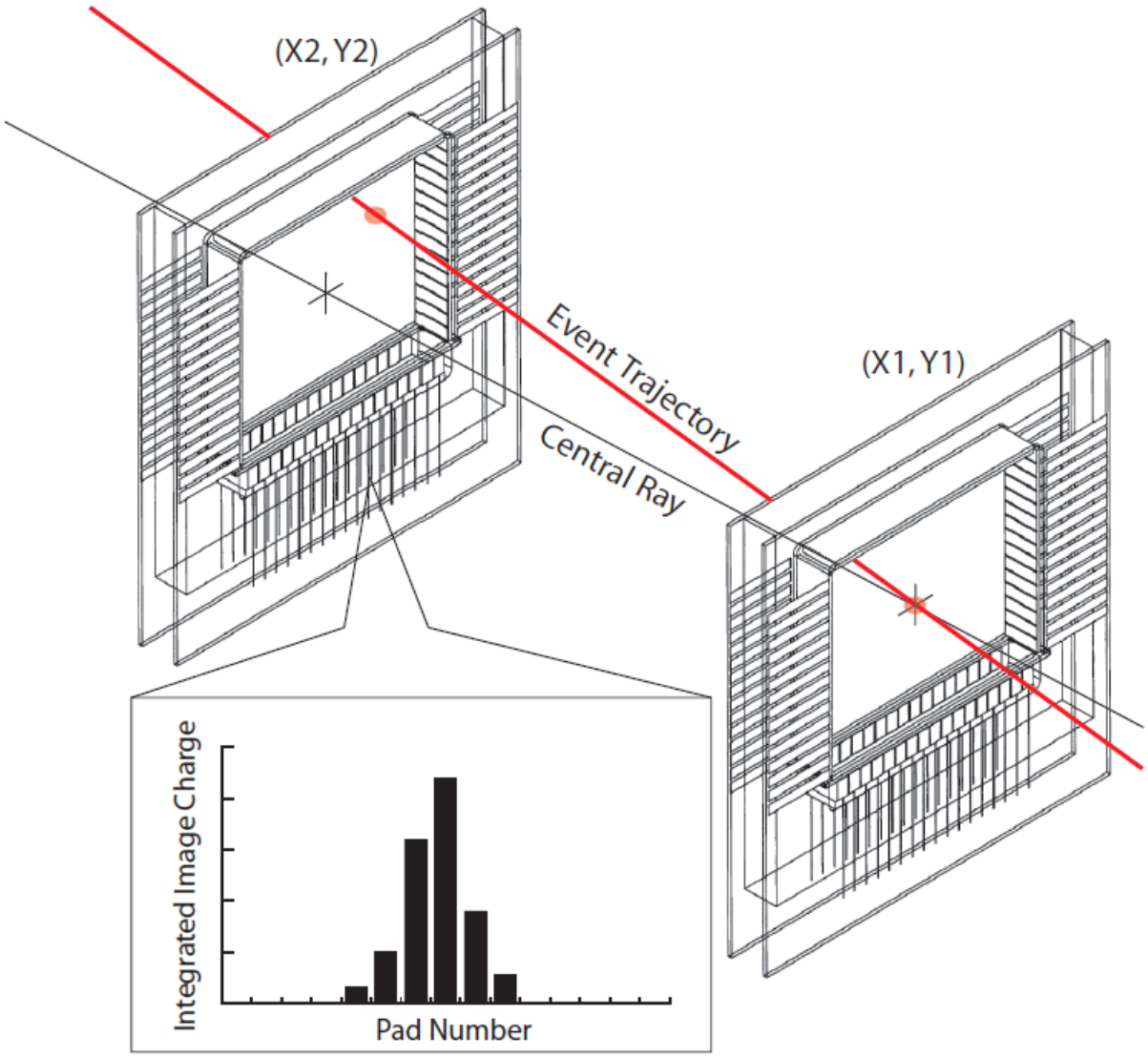

Figure 3.4: This diagram illustrates how the CRDCs in the focal plane of the S800 spectrograph work. The CRDCs are used to measure the transverse positions of an event at two different locations along the beam axis of the focal plane. This information can then be used to reconstruct the dispersive and non-dispersive angles of the event's trajectory. The red line is an example of an event, and the thin black line shows the central axis of the S800 spectrograph focal plane. The bar-chart insert shows an example of an integrated image charge as measured by the CRDCs. The integrated image charge is fitted with a Gaussian line to obtain a specific dispersive position. The original CRDC image is taken from Reference [64] and was adapted by G. W. Hitt in Reference [47].

Name	Voltage Applied (V)
CRDC 1 Anode	1150
CRDC 1 Drift	800
CRDC 2 Anode	1150
CRDC 2 Drift	800
Grid	25
Upper Scintillator PMT	1790
Lower Scintillator PMT	1760

Table 3.1: This table lists the voltages that were applied to the S800 spectrograph focal plane detectors for this experiment.

Table 3.1 lists the voltages that were applied to the CRDCs during this experiment.

The plastic scintillator that was present in the S800 for this experiment was used to measure relative energy loss and to provide a timing signal. This scintillator was a 1 mm thick piece of C_9H_{10} plastic with photomultiplier tubes (PMT) attached to both ends. Ejectiles that pass through the scintillator deposit energy proportional to their proton number squared (Z^2) and dependent on their velocity. Some of that energy will excite electrons in the plastic. As these electrons de-excite, they release photons that are detected in the PMTs. A timing signal generated by the scintillator serves as a trigger for the data acquisition system and as the start of a time-of-flight measurement. The cyclotron RF provides a corresponding stop signal for the time-of-flight measurement. Energy loss and time-of-flight information were used to make a particle identification (see Section 4.1.1 for more details) to ensure measurement of the desired reaction channel and to exclude background events. Table 3.1 lists the voltages that were applied to the PMTs during this experiment.

Chapter 4

Data Analysis

This chapter will explain the data analysis process used for this dissertation. The data collected with the S800 spectrograph (see Section 3.3 for details) from the ^{19}F(t,^{3}He)^{19}O* reaction at 115 MeV/nucleon was used to obtain excitation energy spectra for the ^{19}O* recoil nucleus in Section 4.1. The excitation energy spectra were converted into differential cross sections, up to 16 MeV in the excitation energy of the ^{19}O recoil nucleus, in Section 4.2. A multipole decomposition analysis was performed to extract the $\Delta L = 0$ contributions to the differential cross sections as a function of excitation energy. In Section 4.3, the Gamow-Teller strength distribution for the ^{19}F(t,^{3}He)^{19}O* reaction was extracted using the proportionality relationship between the $\Delta L = 0$ component of the differential cross section at zero momentum transfer and the Gamow-Teller strength (see Equation 4.3.1 and Section 2.1). Finally, the Gamow-Teller strength associated with the excitation of the 0.096 MeV state in ^{19}O was used to calculate the corresponding β-decay rate of ^{19}O*(β^{-})^{19}F in Section 5.1, because this specific low-lying state was important for the astrophysical application discussed in Chapter 1.

4.1 Extracting Excitation Energy Spectra

Data extracted from the S800 spectrograph focal plane detectors were used to reconstruct the excitation energy spectra and to determine the differential cross sections. The ejectile

Name	Description
tof	time of flight of the ejectile: the difference between an initial timing signal from a thin scintillator in the focal plane and a stop timing signal from the radiofrequency of the K1200 cyclotron, in arbitrary units
de1u	energy loss signal from the upper photomultiplier tube on the thin scintillator, in arbitrary units
de1d	energy loss signal from the lower photomultiplier tube on the thin scintillator, in arbitrary units
de1	derived energy loss in the thin scintillator, in arbitrary units: $de1 = \sqrt{(de1u)(de1d)}$
xg1	position in the dispersive plane recorded by CRDC 1, in terms of a pad number
xg2	position in the dispersive plane recorded by CRDC 2, in terms of a pad number
tac1	drift time recorded by CRDC 1, in nanoseconds; used to determine the position in the non-dispersive plane
tac2	drift time recorded by CRDC 2, in nanoseconds; used to determine the position in the non-dispersive plane

Table 4.1: A description of the ejectile parameters that were measured with the S800 spectrograph focal plane.

parameters measured by the S800 spectrograph at the focal plane are listed in Table 4.1. The extracted energy loss and timing information was used to uniquely identify and separate the desired $^{3}He^{2+}$ ejectiles from other possible reaction products and background events (described in Section 4.1.1). The position parameters that were measured at the S800 spectrograph focal plane were also calibrated (discussed in Section 4.1.2) and used to reconstruct the ejectile's properties at the secondary target position (explained in Section 4.1.3). Table 4.2 provides a summary of the reconstructed ejectile parameters at both the focal plane and the secondary target position. These parameters are referred to and used in calculations throughout this chapter. When a parameter is corrected or calibrated, a subscript "c" is used to differentiate the corrected parameter from the original data.

The properties of the ejectile at the secondary target position were used to calculate the excitation energy of the recoil nucleus through a missing mass calculation (described in

Name	Description
afp	angle in the dispersive plane at the focal plane, in radians
bfp	angle in the non-dispersive plane at the focal plane, in radians
xfp	position in the dispersive plane at the focal plane, in microns
yfp	position in the non-dispersive plane at the focal plane, in microns
ata	angle in the dispersive plane at the target, in radians
bta	angle in the non-dispersive plane at the target, in radians
dta	fractional energy, closely related to the ejectile's kinetic energy
yta	position in the non-dispersive plane at the target, in meters

Table 4.2: A description of the ejectile parameters that were calculated from the measurements taken with the S800 spectrograph.

Section 4.1.4). Some corrections were applied to improve energy resolution (explained in Section 4.1.5). The excitation energy spectra obtained through this method were used to construct differential cross sections in Section 4.2.

4.1.1 Particle Identification

The S800 spectrograph detects particles with a magnetic rigidity within a narrow range. In this experiment, a central magnetic rigidity setting of Bρ = 2.32930 Tm ($\pm$0.5% due to momentum acceptance restrictions) was selected to correspond with the rigidity of the ^{3}He^{2+} ejectiles that are produced in the (t,^{3}He) reaction at a triton beam energy of 115 MeV/nucleon in the excitation energy region of interest. The limited momentum acceptance of the S800 spectrograph prevented most ejectiles from alternative reaction channels in the secondary target from entering the S800 spectrograph focal plane. However, there were still some background events that needed to be separated from the desired (t,^{3}He) reaction channel ejectiles. Many of these background events were due to unreacted tritons scattering off the S800 spectrograph dipole magnets or ejectiles from triton reactions such as (t, d) or (t, p) with the aforementioned magnets. A particle identification gate was necessary to select out

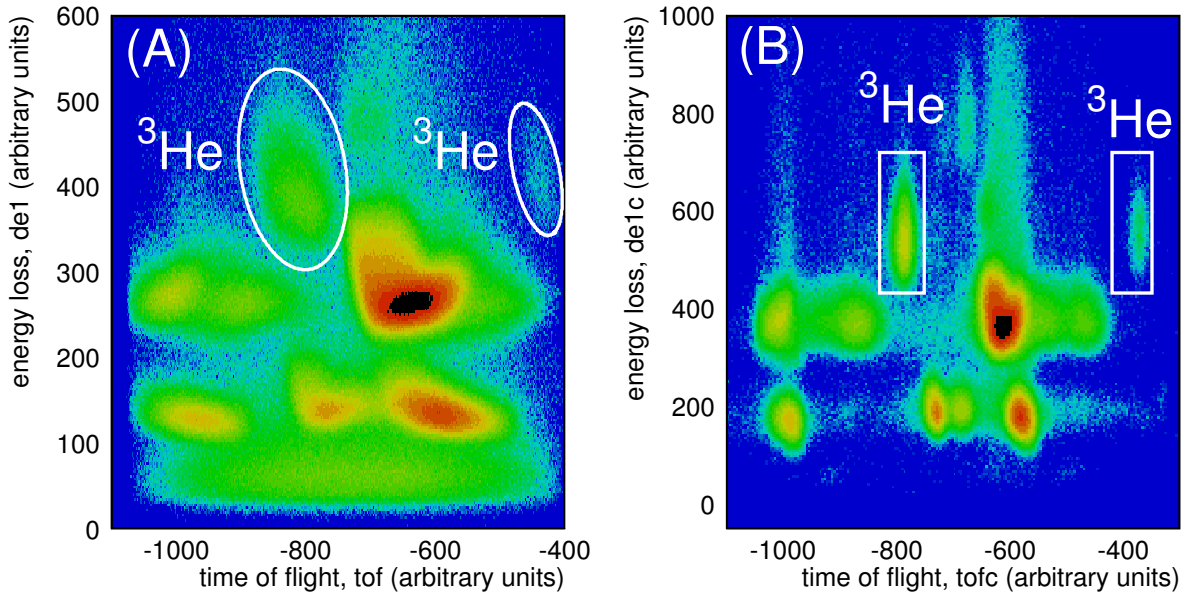

Figure 4.1: These figures show particle identification spectra. The z-axis is on a logarithmic scale. Two cycles of the cyclotron RF are shown here, so two blobs in each figure correspond to the desired $^3He^{2+}$ ejectiles. Figure A (left) shows the particle identification spectrum before any corrections were applied. The white circles identify the $^3He^{2+}$ events. Figure B (right) shows the improved separation of the $^3He^{2+}$ from the background after corrections were applied. The white boxes illustrate the $^3He^{2+}$ gating used in the data analysis.

only the relevant $^3He^{2+}$ events from background events.

A particle identification spectrum was generated from data recorded at the thin scintillator in the S800 spectrograph focal plane. In this spectrum, the time of flight (*tof*) is plotted versus the energy loss (*de1*) as shown in Figure 4.1. This type of particle identification spectrum can be used to separate the ejectiles from different reaction channels in the secondary target. The energy loss (*de1*) is proportional to the ejectile proton number squared (Z^2) as determined with the Bethe-Bloch equation; energy loss allows for the selection of the desired ejectile isotope (in this experiment, ^{3}He). The time of flight (*tof*) is proportional to $\frac{M}{q}$, where M is ejectile mass and q is ejectile charge; the time of flight allows for the selection of the desired reaction channel (in this experiment, (t,^{3}He) reactions at the secondary target position are the desired reaction channel).

Events corresponding to the (t,^{3}He) reaction were easily determined in the particle identification spectrum. Data was taken on a target with a well-known excitation energy spectrum. Then, each blob in the particle identification spectrum was gated on individually until the expected excitation energy spectrum was found. In this case, a target of CH_2 was selected for this purpose because the excitation energy spectrum of the ^{12}C(t,^{3}He)^{12}B* reaction has been studied previously and was easily identifiable. The blobs corresponding to ^{3}He ejectiles are marked in Figure 4.1. In theory, if the other blobs were due to interactions in the reaction target from an alternative reaction channel, that reaction channel could potentially be identified by closely examining the excitation energy spectrum and comparing it to known excited states. However, the other blobs in the particle identification spectrum for this experiment did not correspond to reactions in the secondary target. When these background blobs were gated on, the measured trajectories exhibited unusual angular distributions, which strongly implied that they were background events that did not originate at the secondary target, as discussed above.

To clean up the particle identification spectrum so that the ^{3}He ejectiles were easily separated from background events, linear corrections were applied to the time of flight (tof) and energy loss ($de1$). For a given ejectile isotope, the time of flight corrections removed the dependence on momentum and path length, while the energy loss corrections removed the dependence of energy loss on path length. The corrected parameters are referred to as tof_c and $de1_c$. The specific corrections used in this experiment were determined phenomenologically and are listed in Table 4.3. The effect of these corrections is illustrated in Figure 4.1 B. The gate for the ^{3}He ejectiles was chosen from this corrected particle identification spectrum and used during further data analysis (the gate ranges used are also listed in Table 4.3).

Particle Identification corrections
$tof_c = tof + (1.95)(xg2 - xg1) + (0.169)(xg2) + (0.008)(xg1)$
$de1u_c = de1u + (0.84)(xg2 - xg1)$
$de1d_c = de1d - (1.07)(xg2 - xg1)$
$de1_c = \sqrt{(de1u_c)(de1d_c)}$

Boundaries for the ^{3}He gate	
$de1_c$ range	tof_c range
$432 < de1_c < 720$	$-830 < tof_c < -751$
$432 < de1_c < 720$	$-420 < tof_c < -350$

Table 4.3: This table lists the formulas used to make corrections to the time of flight (*tof*) and energy loss (*de1*) to obtain a clean gate on ^{3}He in the particle identification spectrum. The ^{3}He gate boundaries are also listed.

4.1.2 Cathode Readout Drift Chamber Calibration

The cathode readout drift chamber (CRDC) position measurements (*xg1, xg2, tac1, tac2*) were recorded in terms of pad numbers (in the dispersive plane) and electron drift time (in the non-dispersive plane). To convert these parameters into physical distances, a mask calibration was performed. A tungsten plate with a distinct set of holes and slits (see Figure 4.2) was inserted upstream of each CRDC sequentially. The distances between the holes and slits in these masks were well-known. Ideally, the mask blocks all particles except those that pass through the holes and slits, and thus the pattern of dots and lines observed in a masked CRDC run can be used to determine the conversion between the position parameters and actual distances with a linear parameterization.

However, the ^{3}He ejectile has a low proton number of $Z = 2$. The masks are not thick enough to stop fast ejectiles with such a low Z, so the ^{3}He ejectiles passed through the mask without stopping. This made it difficult to isolate the slit-hole pattern to calibrate the CRDC positions. However, the ^{3}He ejectiles lost some energy as they passed through the mask, causing the ejectiles to slow down slightly if they did not pass through a hole or

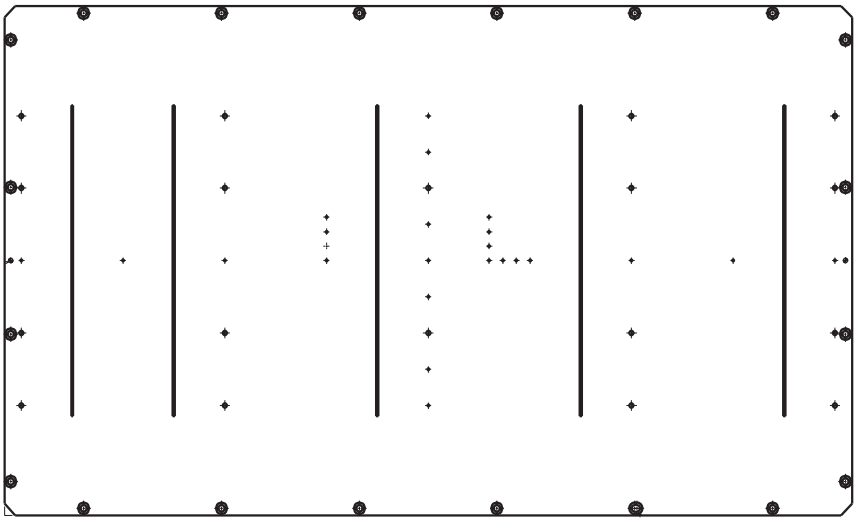

Figure 4.2: A schematic of the tungsten mask used for position calibrations of the CRDCs. This figure was taken from [40].

slit. Then, when the ^{3}He ejectiles interacted with the thin scintillator in the focal plane, the slower particles that had passed through the mask deposited more energy than the faster particles that had passed through slits or holes. Thus, through careful gating on energy loss (*de1*), ejectiles that had passed through the mask were separated from ejectiles that had passed through a hole, so the slit-hole pattern was recovered and used for calibration.

The CH_2 target was used during the mask calibration runs because it had the highest rate of ^{3}He ejectiles, and thus produced the best statistics of any of the available target options. However, the statistics for the mask calibration runs were relatively poor, so only a few mask holes were visible in the calibration runs (the slits were still easily visible, see Figure 4.3). To compensate for the difficulty of detecting the holes, information from a prior S800 spectrograph experiment was used to establish an initial calibration. This prior experiment, NSCL experiment number 08017, detailed in Reference [40], had higher statistics for its mask calibration runs. This initial calibration from experiment 08017 made it possible to identify a few holes and ensure that they were assigned correctly. The data from the mask

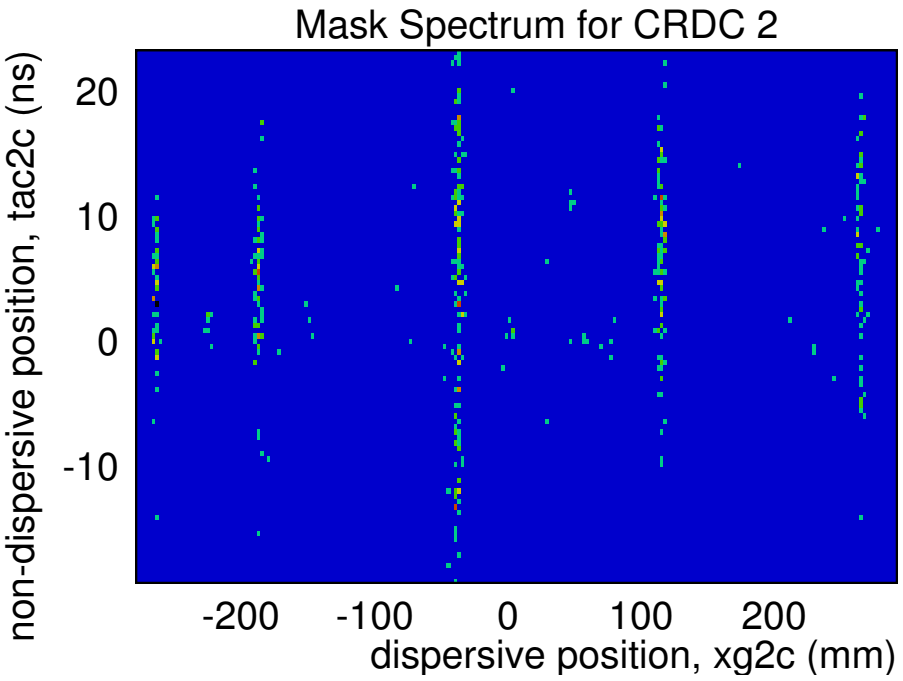

Figure 4.3: Position measurements for the mask calibration of CRDC 2. The slits from the mask were easily visible, but the holes were more difficult to distinguish.

runs in the present experiment were then used to refine and finalize the position calibration. Since it is possible to fine-tune the mask calibrations by applying kinematical constraints to the data sets, further mask calibration runs were unnecessary (see Section 4.1.5). The calibration was a simple linear relationship with parameters of slope (M) and intercept (B):

$$\text{calibrated CRDC position} = M(\text{CRDC data}) + B. \tag{4.1.1}$$

The values that were found for the parameters of the four calibrations are listed in Table 4.4. The origin of the coordinates corresponds to the vertex of the L-shape seen in the mask (see Figure 4.2), which is also the central trajectory through the S800 spectrograph for particles with the appropriate magnetic rigidity (Bρ). The calibration in the dispersive plane is stable over the duration of an experiment [47]. However, the slope in the non-dispersive plane is dependent on the electron drift velocity in the CRDCs and is sensitive

Name	CRDC	Plane	M	B
$xg1_c$	CRDC 1	Dispersive	2.54 mm/pad	-278.88 mm
$xg2_c$	CRDC 2	Dispersive	2.54 mm/pad	-278.99 mm
$tac1_c$	CRDC 1	Non-dispersive	-0.068 mm/ns	132.34 mm
$tac2_c$	CRDC 2	Non-dispersive	0.071 mm/ns	-147.35 mm

Table 4.4: Parameters used to calibrate CRDC data to a physical position, in millimeters. The values for M in the dispersive plane are fixed to the width of each pad at 2.54 mm.

to subtle changes in experimental conditions, so it tends to change slowly over the course of an experiment. It was not practical to take multiple CRDC calibration runs during this experiment, so these corrections were instead done on a run-by-run basis by examining the data as discussed in Section 4.1.5.

By using these calibrated position parameters ($xg1_c$, $xg2_c$, $tac1_c$, and $tac2_c$), angles and positions at the focal plane (*afp*, *bfp*, *xfp*, and *yfp*) were calculated in the format needed for the next step in the data analysis. The equations for the parameter transformations in the dispersive and non-dispersive planes for the angles (*afp* and *bfp*, respectively) and positions (*xfp* and *yfp*, respectively) are:

$$afp = \arctan\left(\frac{xg2_c - xg1_c}{1073}\right), \tag{4.1.2}$$

$$bfp = \arctan\left(\frac{tac2_c - tac1_c}{1073}\right), \tag{4.1.3}$$

$$xfp = \frac{xg1_c}{1000}, \text{ and} \tag{4.1.4}$$

$$yfp = \frac{tac1_c}{1000}. \tag{4.1.5}$$

The factor of 1073 present in the calculations of *afp* and *bfp* comes from the distance between the two CRDCs, which is 1.073 meters. The units chosen for these parameters were selected

for compatibility with the inverse transfer map matrix calculation detailed in Section 4.1.3.

4.1.3 Ejectile Parameters at the Secondary Target

Data on the position and the trajectory angle of the ejectile at the S800 spectrograph focal plane can be converted into information on the ejectile's properties as it leaves the secondary target. Since the goal of this data analysis is to study the excitation energy spectrum of the recoil particle, this conversion is a necessary step towards reconstructing reaction cross sections. This parameter conversion was accomplished via an inverse transfer map matrix. The inverse transfer map matrix transformed the positions (*xfp, yfp*) and angles (*afp, bfp*) at the focal plane into the position in the non-dispersive plane (*yta*), angles in the dispersive and non-dispersive planes (*ata, bta*), and fractional energy (*dta*) at the reaction target position [65].

The inverse transfer map matrix was generated using a COSY INFINITY [68, 69] calculation. Inputs for this calculation include magnetic field maps of the S800 spectrograph as well as experiment-specific magnetic rigidity settings and current settings. These experiment-specific settings were determined by the magnetic rigidity (Bρ) of the ejectile nucleus to be measured, which dictated the current that was needed in the S800 spectrograph dipole and quadrupole magnets. The values used for this experiment are listed in Table 4.5. Currently, the COSY INFINITY program used to determine the inverse transfer map matrix for the S800 spectrograph is accessible online at `http://maps.nscl.msu.edu/~s800maps/` and uses a fifth order calculation to generate the map matrix. The exact formula for the transform can be found in Reference [65] and additional details on this calculation are available in Reference [40].

The distance between the target and pivot point (d_1) was nonzero mainly due to imper-

Parameter	Value	Description
I256QA	-38.499 Amps	current in a quadrupole magnet
I258QB	35.342 Amps	current in a quadrupole magnet
I265DS	157.501 Amps	current in a dipole magnet
I269DS	157.519 Amps	current in a dipole magnet
Bρ	2.32930 Tm	magnetic rigidity of the S800 spectrograph
A	3	ejectile mass number
Z	2	ejectile proton number
d_1	-0.08 m	distance between target and pivot point
d_2	0.0	focal plane shift

Table 4.5: These settings for the S800 spectrograph were taken from a run midway through the experiment. This information was used in the COSY INFINITY calculation of the inverse transfer map matrix.

fections in the COSY INFINITY calculation of the inverse transfer map matrix, though some of the shift was likely due to minor uncertainty in the placement of the secondary target. It was possible to experimentally determine this pivot point shift through examination of the data. An unaccounted-for shift from the pivot point results in a noticeable rotation between the angle in the non-dispersive plane (bta_c) and the position in the non-dispersive plane (yta_c). When the shift is corrected for, this rotation vanishes. The ^{56}Fe target had a thick frame that illustrated this effect clearly (see Figure 4.4). A thick metal frame held the ^{56}Fe target on both edges in the non-dispersive plane, and was thus expected to occupy a small, fixed span of yta_c on both sides of the target. Since the frame was much thicker than the target, many background reactions occurred when the frame was hit by the beam, so events in the frame were clearly distinguishable from ^{56}Fe target events in the spectra as shown in Figure 4.4. When the pivot point shift was not corrected for in the COSY INFINITY calculation ($d_1 = 0$ cm), the two frame edges appeared diagonally in a bta_c vs. yta_c plot. When the shift from the focal plane was correctly accounted for ($d_1 = -8$ cm), the frame position in the non-dispersive plane (yta_c) was independent of the angle in the non-dispersive plane (bta_c). The value of d_1 found for the present experiment was similar to the pivot

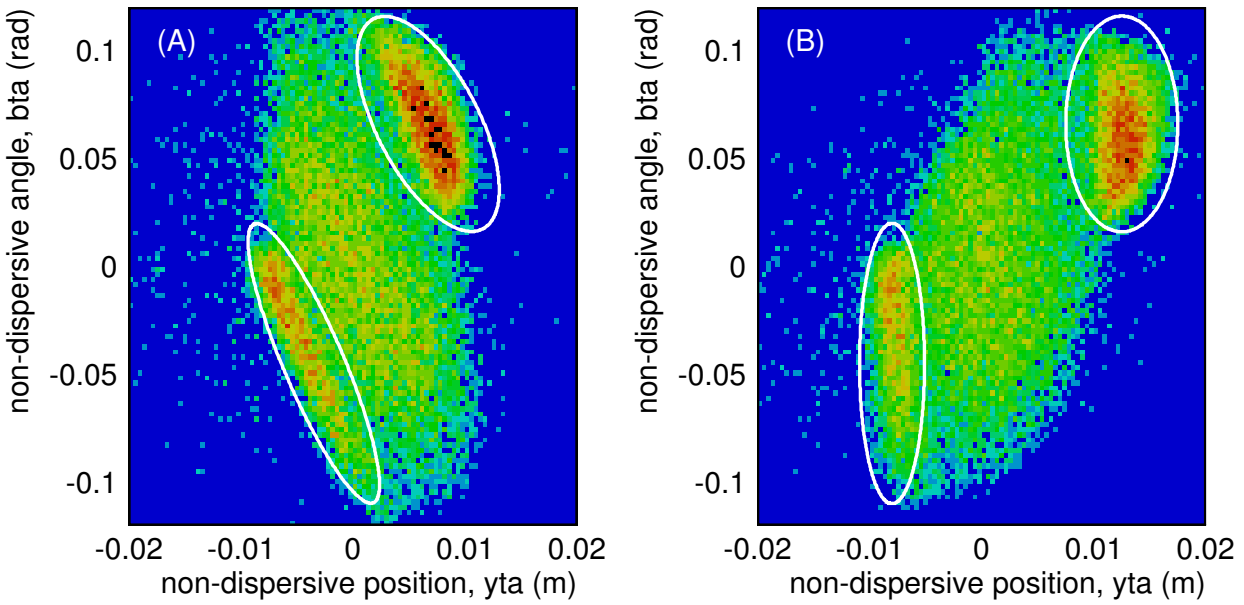

Figure 4.4: These figures demonstrate how the pivot point shift (d_1) was corrected. The thick frame around the edges of the ^{56}Fe target created many background events (circled) that were used to determine the pivot point shift. Figure A (left) shows the rotation between yta_c and bta_c that occurs when the pivot point shift was not accounted for. Figure B (right) shows that, when this shift was corrected, the frame position in the non-dispersive plane was independent of the angle in the non-dispersive plane.

point shift seen in a prior S800 spectrograph experiment and to prior simulation results by G. W. Hitt [47].

The parameter for fractional energy (dta) is closely related to kinetic energy (T_e). Fractional energy (dta) is a measure of the ejectile's energy relative to the energy of an ejectile traveling along the central trajectory (E_0) through the S800 spectrograph with the selected magnetic rigidity. The central kinetic energy of a ^{3}He ejectile with Bρ = 2.32930 Tm was calculated to be E_0 = 327.995 MeV. The formula used to determine the ejectile's kinetic energy (T_e) from the fractional energy parameter (dta) is:

$$T_e = (1 + dta)E_0. \tag{4.1.6}$$

A laboratory reference frame scattering angle was needed to construct differential cross sections. This scattering angle (θ_{lab}) was determined from the angle in the dispersive plane (ata) and the angle in the non-dispersive plane (bta) at the target location through:

$$\theta_{lab} = \arctan\left(\sqrt{\tan^2(ata) + \tan^2(bta)}\right). \tag{4.1.7}$$

The laboratory scattering angles (θ_{lab}) were converted to the center-of-mass reference frame (θ_{com}). At forward scattering angles, this transformation can be approximated with a linear scaling factor (S) with negligible error, as in Equation 4.1.8. The values used for the scaling factor were $S = 1.281$ for the ^{12}C target nuclei and $S = 1.176$ for the ^{19}F target nuclei with the kinematics of this experiment.

$$\theta_{com} = S\theta_{lab}. \tag{4.1.8}$$

4.1.4 Missing Mass Calculation

Once the motion of the ejectile at the secondary target position was well-defined by ata, bta, yta, and dta, a kinematic missing-mass calculation was used to recreate the excitation energy (E_x) of the recoil nucleus. The 4-momentum of the incoming projectile and the outgoing ejectile system (the target nucleus is immobile) were defined as follows.

Incoming projectile 4-momentum:

$$T_p = 340 \text{ MeV}, \tag{4.1.9}$$

$$p_{p1}c = 0, \tag{4.1.10}$$

$$p_{p2}c = 0, \text{ and} \tag{4.1.11}$$

$$p_{p3}c = p_{p4}c = \sqrt{(T_p + M_p c^2)^2 - (M_p c^2)^2}, \tag{4.1.12}$$

where p_{pi} was the projectile momentum i-component, T_p was the projectile kinetic energy, M_p was the projectile mass, and c was the speed of light. In this experiment, the exact projectile kinetic energy (T_p) was determined from calibration runs using a CH_2 target. The value of T_p was varied until the ground state excitation energy for the ^{12}C(t,^{3}He) reaction corresponded to zero, which means that it was assumed that there was no systematic error in the S800 spectrograph energy measurements. Additionally, setting p_{p1} and p_{p2} to zero was an approximation; in practice, the incoming beam had distributions of momentum in the transverse plane. This approximation decreased the experiment's angular and energy resolution.

Outgoing ejectile 4-momentum:

$$T_e = (1 + dta)E_0, \tag{4.1.13}$$

$$p_{e1}c = (p_{e4}c)\sin(ata), \tag{4.1.14}$$

$$p_{e2}c = (p_{e4}c)\sin(bta), \tag{4.1.15}$$

$$p_{e3}c = (p_{e4}c)\cos(\theta_{lab}), \text{ and} \tag{4.1.16}$$

$$p_{e4}c = \sqrt{(T_e + M_e c^2)^2 - (M_e c^2)^2}, \tag{4.1.17}$$

where p_{ei} was the ejectile momentum i-component, T_e was the ejectile kinetic energy, and M_e was the ejectile mass.

The missing energy (E_{mis}) was found from:

$$E_{mis} = (T_e + M_e c^2) - (T_p + M_p c^2 + M_t c^2), \tag{4.1.18}$$

where M_t was the mass of the target nucleus. The missing momentum (p_{mis}) was:

$$p_{mis} = \sqrt{p_{e1}^2 + p_{e2}^2 + (p_{e3} - p_{p3})^2}. \tag{4.1.19}$$

This gave the missing mass (M_{mis}) and the recoil excitation energy (E_x) as:

$$M_{mis}c^2 = \sqrt{E_{mis}^2 - (p_{mis}c)^2} \text{ and} \tag{4.1.20}$$

$$E_x = M_{mis}c^2 - M_r c^2, \tag{4.1.21}$$

where M_r was the mass of the recoil in its ground state. All of the masses relevant for this data analysis were taken from Reference [70] and are listed in the form of a mass excess[1] in Table 4.6.

4.1.5 Excitation Energy Corrections

The excitation energy of the recoil nucleus (E_x) is independent of the scattering angle (θ_{lab}). In practice, small corrections to *ata* and *bta* are needed to achieve this. The kine-

[1]The mass of atom, M, is found with the formula $M = A\left(\frac{931.494 \text{ MeV}/c^2}{1 \text{ amu}}\right) + ME$, where A is the atomic mass number and ME is the mass excess.

Nucleus	Mass Excess (MeV/c^2)	Nucleus	Mass Excess (MeV/c^2)
^{3}H	14.9498060	^{12}C	0.0
^{3}He	14.9312148	^{12}B	13.3689
^{1}H	7.28897050	^{19}F	-1.48739
n	8.0713171	^{19}O	3.3349

Table 4.6: This table lists the mass excesses that were relevant for this data analysis, as taken from Reference [70].

$$
\begin{aligned}
ata_c &= ata(0.987) + 0.00042 \\
bta_c &= bta(1.03) - (1.005)yta + 0.00325 \\
afp_c &= (0.95)\arctan\left(\frac{xg2_c - xg1_c}{1073}\right) \\
yfp_c &= (0.95)\left(\frac{tac1_c}{1000}\right)
\end{aligned}
$$

Table 4.7: This table contains the kinematic corrections that were applied to the angle in the dispersive plane (ata) and to the angle in the non-dispersive plane (bta) at the target position. Similarly, a factor of 0.95 was applied earlier in the data analysis process to correct the angle in the dispersive plane (afp) and position in the non-dispersive plane (yfp at the S800 spectrograph focal plane).

matic line from $p(t,^3\mathrm{He})n$ reactions in the CH_2 calibration target were used to perform this correction, because recoil energy is more strongly correlated to θ_{lab} in light nuclei than in heavy nuclei. The first-order corrections that were required to ensure that the excitation energy (E_x) was independent of the scattering angle (θ_{lab}) are listed in Table 4.7.

In addition, afp and yfp were scaled by a factor of 0.95 (see Table 4.7) to improve the reconstruction of the excitation energy (E_x). These corrections were likely related to minor inaccuracies in the calculation of the inverse transfer map matrix that was discussed in Section 4.1.3.

Some minor run-by-run corrections were required to obtain the optimal energy resolution. These small shifts ensured that the excitation energy was independent of scattering angle across the entire duration of the experiment, and that the scale for the excitation energy of the recoil was consistent. These run-by-run corrections compensated for gradual changes in

Run	exa_shift	ata_shift	yta_shift	Run	exa_shift	ata_shift	yta_shift
1012	-0.016	0.8	0.0100	1019	-0.02	-0.17	0.0114
1013	-0.018	1.7	0.0116	1064	0.017	0.12	0.0050
1014	-0.015	-0.07	0.0113	1067	-0.08	1.3	0.0057
1015	-0.01	-0.3	0.0108	1068	-0.08	3.6	0.0052
1016	-0.005	0.4	0.0107	1069	-0.06	0.04	0.0051
1017	0.011	1.8	0.0105	1099	-0.079	-0.7	0.0018
1018	0.014	-0.4	0.0107				

Table 4.8: This table lists all run-specific corrections. These corrections compensated for small changes that occurred during the experiment, such as small shifts in the beam alignment or changes in the gas of the CRDCs.

the CRDCs that caused variations in the calibration of the position in the non-dispersive plane. Run-by-run corrections also compensated for minor changes over time in the triton beam, such as shifts in the beam angular distribution. A run-by-run shift on *yta* was used to center the distribution of the position in the non-dispersive plane on zero, which simplified the acceptance corrections in Section 4.2.1.

The run-by-run corrections were linear and took the form of:

$$yta_c = yta - yta\_shift \text{ and} \tag{4.1.22}$$

$$E_{xc} = E_x - (ata_c)(ata\_shift) - exa\_shift, \tag{4.1.23}$$

where the parameters *yta_shift*, *ata_shift*, and *exa_shift* are the measured corrections for each run.

With these corrections in place, initial excitation energy spectra for recoil nuclei were obtained. Figure 4.5 shows examples of the excitation energy spectra for the CF_2 target, with kinematics set for the ^{19}F(t,^{3}He)^{19}O* reaction (note that the excited states of ^{12}B due to ^{12}C target nuclei were also visible in these spectra). Gamow-Teller transitions ($\Delta L = 0$) are characterized by angular distributions that peak at forward angles. Thus, restricting

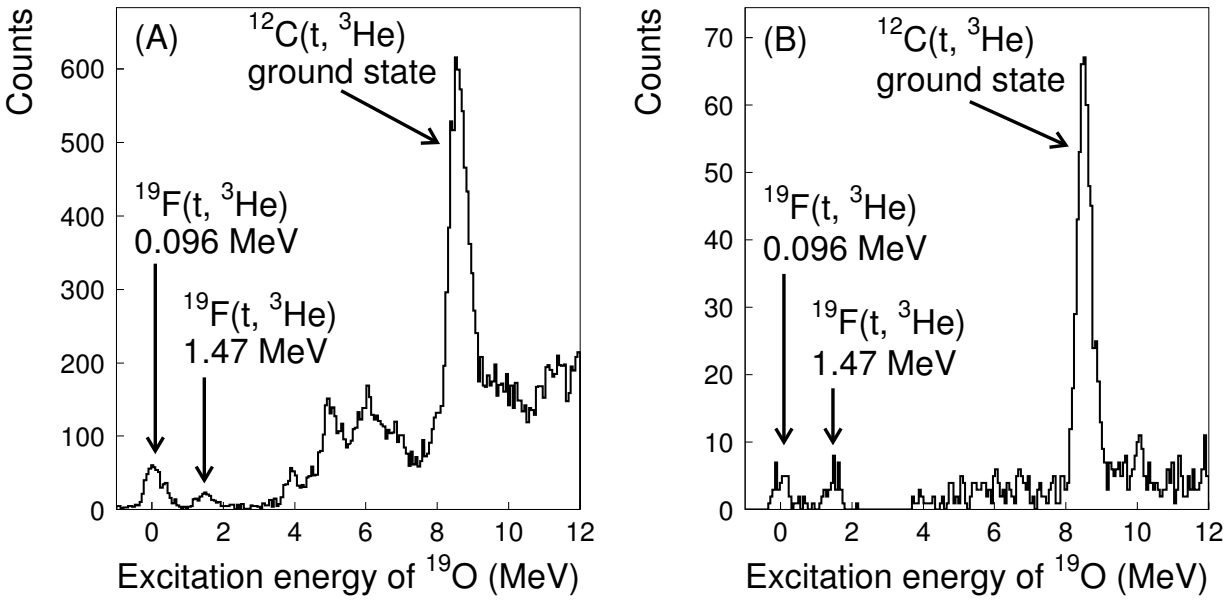

Figure 4.5: These figures show excitation energy spectra for (t,^{3}He) reactions on a CH_2 target. Figure A shows the excitation energy spectrum over all scattering angles. Figure B shows the corresponding spectrum for a scattering angle of 0–1 degrees in the center-of-mass frame, which gives the first indication of what the Gamow-Teller strength distribution will be. Three strong Gamow-Teller states are visible in this figure; the first two are from reactions on ^{19}F and the strongest state is from reactions with ^{12}C to the ground state of ^{12}B.

the center-of-mass frame scattering angle (θ_{com}) to a range of 0–1 degrees gave an initial indication of where Gamow-Teller strength was located (see Figure 4.5 B). Much of the higher-lying strength seen in Figure 4.5 A is dominated by dipole transitions (which peak at higher scattering angles), and thus vanishes in Figure 4.5 B where Gamow-Teller strength is dominant.

4.2 Differential Cross Sections

Differential cross sections are the next information needed to extract a Gamow-Teller strength distribution for the ^{19}F(t,^{3}He)^{19}O* reaction. Since absolute beam intensities were not measured in this experiment, relative differential cross sections were calculated in Section 4.2.1

from the excitation energy spectra found in Section 4.1. Data on the ^{12}C(t,^{3}He)^{12}B* reaction from a prior experiment were then used to scale relative differential cross sections to absolute differential cross sections in Section 4.2.2. In Section 4.2.3, the carbon background was subtracted from the absolute differential cross sections for the CF_2 target data, which produced the absolute differential cross sections for only the ^{19}F(t,^{3}He)^{19}O* reaction. This final set of differential cross sections were then used in Section 4.3 to obtain a Gamow-Teller strength distribution.

4.2.1 Relative Cross Sections

Relative differential cross sections were extracted from the measured excitation energy spectra. First, corrections were made to account for the detector's solid angle coverage and acceptance limitations. Those corrections produced uncalibrated relative cross sections. The uncalibrated relative cross sections were converted to absolute cross sections by establishing a proportionality between the ^{19}F(t,^{3}He) reaction event rate and the ^{12}C(t,^{3}He) reaction event rate while data was taken on the CF_2 target.

To create differential cross sections, the excitation energy spectra were divided into angular bins with a scattering angle width of $\theta_{lab} = 10$ mrad in the laboratory reference frame. Eight bins covered an angular range of 0–80 mrad. The solid angle for an angular bin ranging from θ_1 to θ_2 (see Figure 4.6) was calculated with the following equation:

$$d\Omega(\theta_1 \leq \theta_{lab} \leq \theta_2) = \int_0^{2\pi} d\phi \int_{\theta_1}^{\theta_2} d\theta \sin(\theta) = 2\pi\cos(\theta_1) - 2\pi\cos(\theta_2). \tag{4.2.1}$$

An acceptance correction was necessary to compensate for incomplete coverage of events with large scattering angles in the S800 spectrograph. The S800 spectrograph coverage is

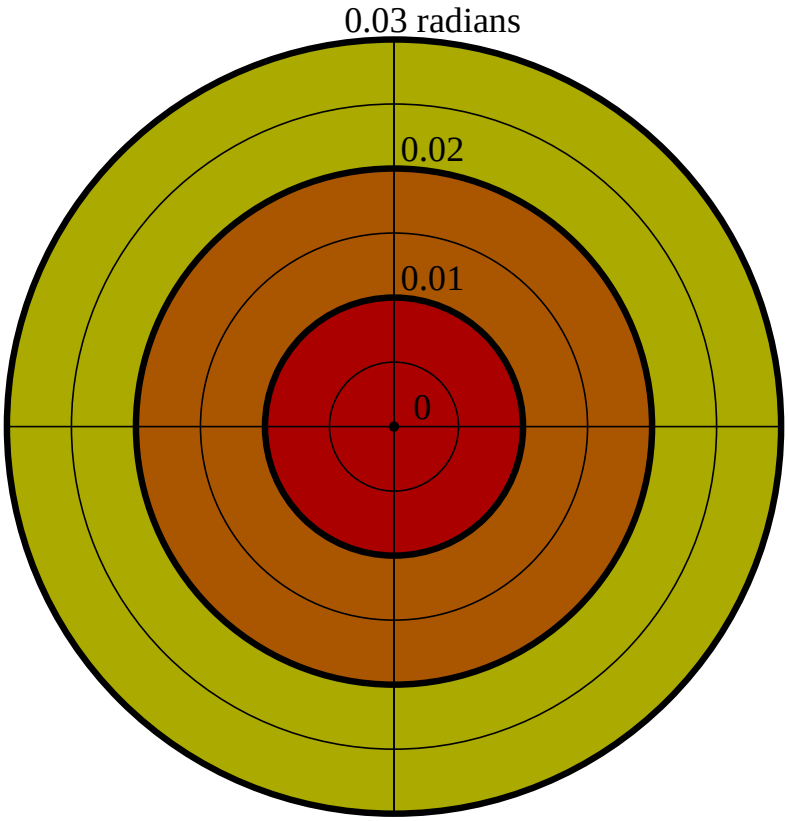

Figure 4.6: This figure illustrates the solid angle coverage as a function of scattering angle (θ_{lab}). The red surface area covers a range of 0 to 10 mrad, the orange surface area covers a range of 10 to 20 mrad, and the yellow surface area covers a range of 20 to 30 mrad. The solid angle is proportional to these areas and to the number of events (in an isotropic distribution).

Boundaries for ata	Boundaries for bta
$ata_c < (2.73244)dta + 0.1453$	$bta_c > (-33.4018)yta_c - 0.33949$
$ata_c < (-0.2269)dta + 0.0626$	$bta_c < (7.546039)yta_c + 0.099082$
$ata_c > (400.6571)dta - 12.3447$	$bta_c < (-5.3610)yta_c + 0.1124$
$ata_c > (-0.0115)dta - 0.0562$	$bta_c < (-182.2980)yta_c + 1.5828$
$ata_c > (-0.9405)dta - 0.0817$	$bta_c > (6.1234)yta_c - 0.0772$
$ata_c < (21.8486)dta + 1.1976$	$bta_c > (-0.6744)yta_c - 0.0702$

Table 4.9: This table lists the boundary equations used to constrain the angles ata and bta in the Monte-Carlo acceptance correction simulation.

complete for ejectiles at scattering angles of $\theta_{lab} < 3.5^\circ$ for the excitation energies studied in this experiment. However, for scattering angles $\theta_{lab} \geq 3.5^\circ$, some ejectiles were obstructed by dipole magnets or fell outside of the range of the focal plane detectors. Instead of disregarding angles with azimuthal coverage less than 2π, a Monte-Carlo simulation was performed to model and correct for the partial loss of events. This procedure allowed for the extraction of differential cross sections up to $\theta_{lab} = 5^\circ$ [48].

The Monte-Carlo simulation produced an isotropic distribution of events over the angles, positions, and energy ranges relevant to this data analysis. It compared the ideal distribution of events to a distribution of events with certain constraints on the angles in the dispersive and non-dispersive planes to determine the probability, $P_{acceptance}$, of a valid event successfully reaching the S800 spectrograph focal plane as a function of dta, yta, and θ_{lab}. The angular constraints used for this simulation were established experimentally. These constraints are represented by the white boundary lines in Figure 4.7 and the equations for the constraints are available in Table 4.9. In the dispersive direction (ata), the angular acceptance depends on the momentum of the particles (dta) as seen in Figure 4.7 A. In the non-dispersive direction (bta), the angular acceptance depends on the non-dispersive position of the particles (yta) as seen in Figure 4.7 B.

Once the solid angle ($d\Omega$) and the acceptance correction ($P_{acceptance}$) were established,

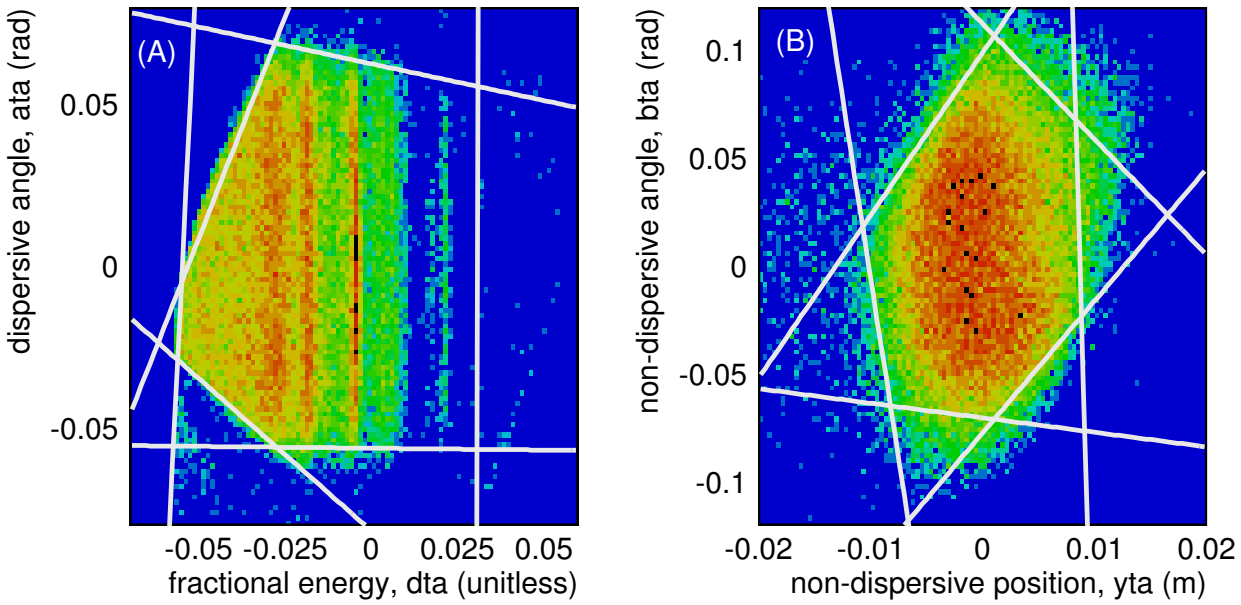

Figure 4.7: These spectra show the boundaries used in the Monte-Carlo simulation that determined the acceptance correction. These figures use data from the CF_2 target.

the unscaled relative differential cross sections were determined from the excitation energy spectra. Each count (N) in a given excitation energy spectrum was divided by the solid angle and acceptance correction:

$$\frac{d\sigma}{d\Omega}(\text{arbitrary units}) = \frac{N(\theta_{lab},\ dta_c,\ yta_c)}{d\Omega(\theta_{lab}) \cdot P_{acceptance}(\theta_{lab},\ dta_c,\ yta_c)}. \tag{4.2.2}$$

These differential cross sections, when compared to measured excitation energy spectra, showed a significant enhancement at small scattering angles from the solid angle and a moderate enhancement at large angles from the acceptance correction. See Figure 4.8 for an example of the transformation from excitation energy spectra to differential cross section for one particular transition.

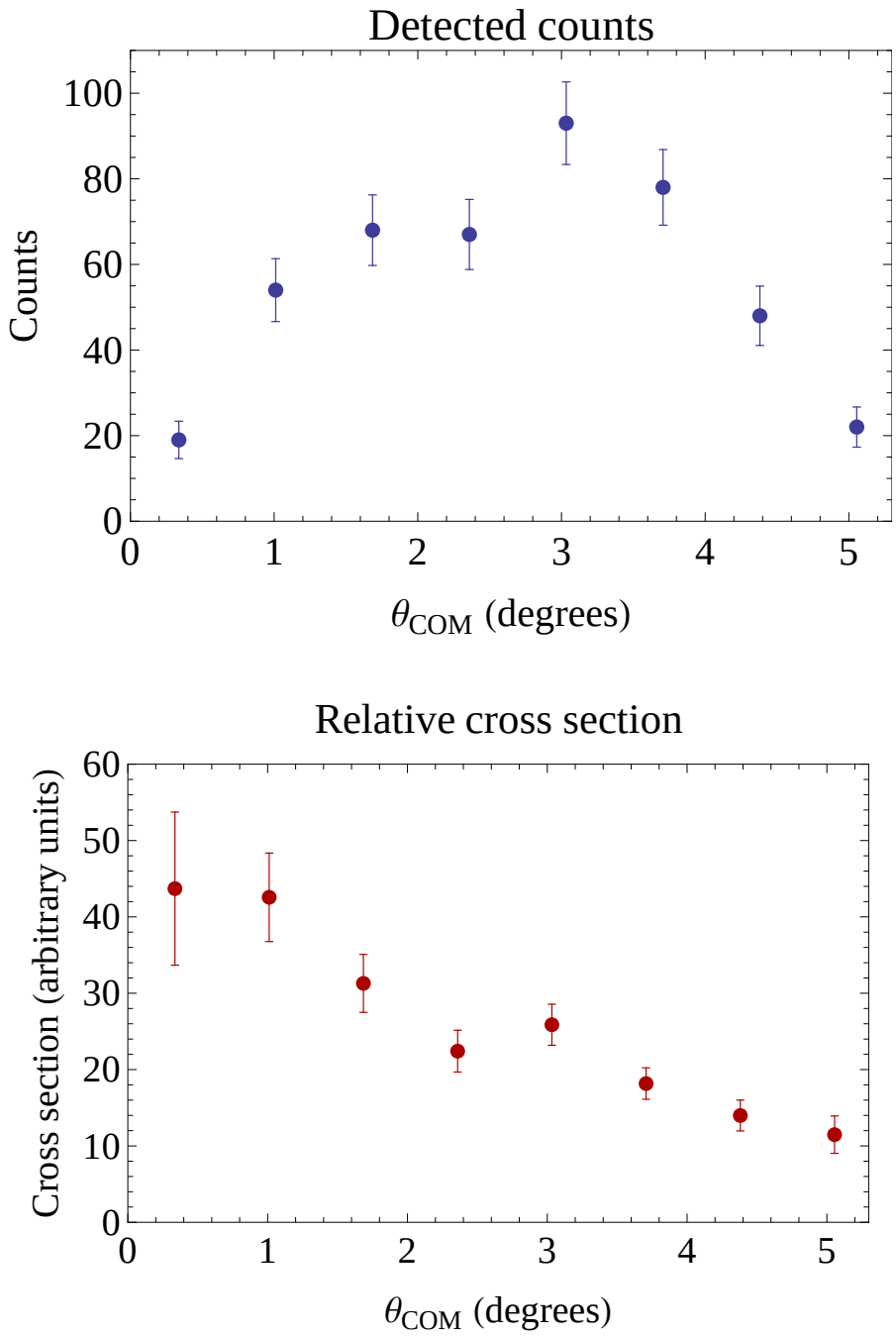

Figure 4.8: These spectra illustrate the transformation from excitation energy spectra to differential cross section for one specific excited state of ^{19}O. The top figure shows the measured excitation energy spectrum for the 0.096 MeV excited state of ^{19}O. The bottom figure shows the relative cross section for the same excited state after the solid angle and the acceptance correction were applied. The solid angle enhances the contribution of the first several angular bins, while the acceptance correction has the strongest effect on the three data points with $\theta_{com} > 3.5°$.

4.2.2 Absolute Cross Sections

So far, the differential cross sections are in arbitrary units. They can be normalized to an absolute scale by taking advantage of the carbon in both the CF_2 and CH_2 targets and information from a prior experiment. In experiment 06032, performed at the NSCL by C. J. Guess *et al.* [48, 71], an absolute cross section was measured for the reaction $^{12}C(t,^3He)^{12}B_{g.s.}$. This reaction was also observed in the current experiment with both the CH_2 and the CF_2 targets. The data from the ^{12}B ground state in the current experiment was scaled to the data from experiment 06032 to find absolute differential cross sections.

While it would have been ideal to compare the ^{12}B ground state data from experiment 06032 directly to the ^{12}B ground state data from the CF_2 target in the current experiment this was not possible due to background events from reactions on ^{19}F nuclei. Instead, the ^{12}B ground state data from experiment 06032 was scaled to the CH_2 data taken in the current experiment with the scaling factor of ϵ_{abs}. After that, an additional factor of ϵ_{prop} was used to scale the data taken on the CH_2 target to the data taken on the CF_2 target.

The ^{12}B ground state in the CH_2 target data was well-separated from other ^{12}B states and from events due to the hydrogen content of the target, so there were no notable background events to contend with. Figure 4.9 shows a comparison of the absolute differential cross section for ^{12}B ground state data from experiment 06032 with the distribution that was extracted during this experiment. A scaling factor of $\epsilon_{\text{abs}} = 0.048 \pm 0.001$ mb was found from a linear fit between the two differential cross sections. This factor of ϵ_{abs} provided an absolute differential cross section for the data taken on the CH_2 target in the current experiment.

A relationship between the CH_2 and CF_2 data sets (ϵ_{prop}) was established by taking

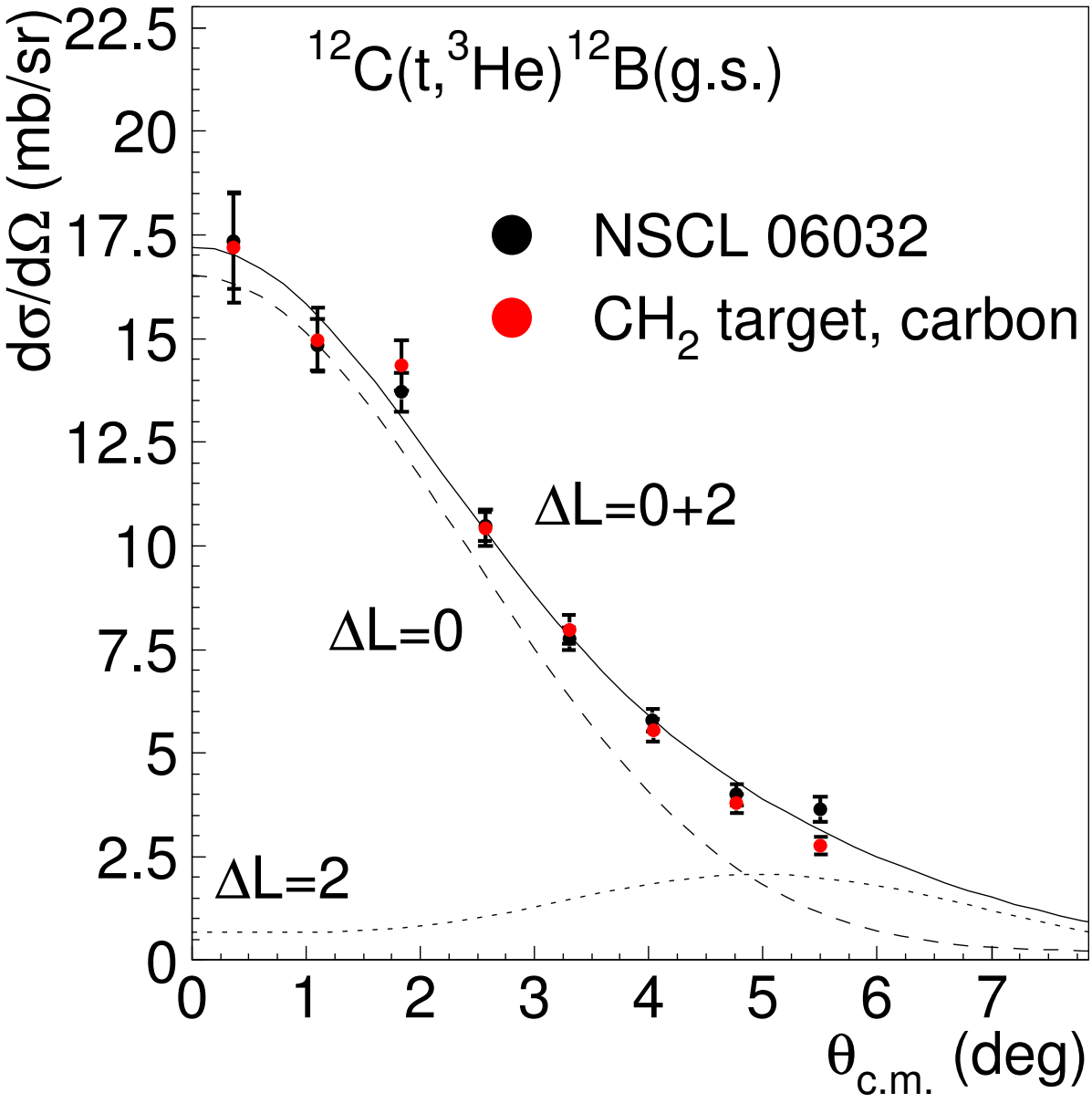

Figure 4.9: This figure shows a comparison of the data from experiment 06032 [48] and the CH_2 target of the current experiment for the ^{12}B ground state after the scaling factor ϵ_{abs} was applied. The angular distribution for this experiment was in excellent agreement with the results from experiment 06032. The ratio between the two results was used to establish an absolute cross section for the data collected in the current experiment, because the absolute cross section was carefully normalized in experiment 06032.

.

into account the differences in integrated beam intensities, data acquisition live times, and target thicknesses. A direct measurement of the triton beam rate at the target position was not available for this experiment, so three different indirect measurements of the beam rate were used instead. Two of these beam rate measurements came from the primary beam current probes that were described in Section 3.1, the Z001I-C probe and the Z026R-C probe. These primary beam current measurements were expected to be directly proportional to the secondary triton beam intensity. The third indirect measurement of the triton beam intensity was made at the S800 spectrograph focal plane. As mentioned earlier, there are a significant number of events seen in the S800 spectrograph particle identification spectra that are not due to reactions in the experimental targets (see Figure 4.1). These background events appeared to be unreacted triton particles that were scattered into the focal plane detectors, and thus also proportional to the triton beam intensity. The background events were used in aggregate to produce a beam rate ratio between the two different data sets for the CH_2 and CF_2 targets.

The beam rate ratios ($\epsilon_1 = \frac{CH_2}{CF_2}$) found were 0.35, 0.33, and 0.36 for the Z001I-C probe, the Z026R-C probe, and the unreacted beam in the S800 spectrograph focal plane, respectively. The beam was fairly stable over the entire experiment, with a run time of 3 hours for the CH_2 target and 9.5 hours for the CF_2 target. The average of these three measurements was taken as the final value of the beam rate ratio, and a conservative error of two standard deviations was used to reflect that these are indirect measurements, for a final value of $\epsilon_1 = 0.35 \pm 0.03$.

The data sets taken with the two different reaction targets had notable differences in overall detector count rates due to composition, which led to differences in data acquisition live times. The CH_2 target, which had a higher measured count rate due to the large reaction

cross section of triton on hydrogen, had an electronics dead time of 8.7%; the CF_2 target had a dead time of 3.7%. This gave a ratio of $\epsilon_2 = 0.9634$ between the CH_2 data set and the CF_2 data set related to data acquisition live time differences. The error in this dead time measurement was neglected because it was much smaller than other sources of experimental error.

Differences in target thickness and composition also needed to be taken into account to establish a proportionality between the CH_2 data set and the CF_2 data set. The CH_2 target had a thickness of 10.0 mg/cm^2, while the CF_2 target had a thickness of 11.2 mg/cm^2. Fluctuations in target thicknesses were negligible sources of error because the beam spot covered a large area of the target foils. The target composition differences were taken into account by calculating the proportion of the molar mass of each target due only to carbon, which was $\left(\frac{12.0108}{14.0266}\right)$ for the CH_2 target and $\left(\frac{12.0108}{50.0076}\right)$ for the CF_2 target. Combined, this gave a target thickness scaling ratio between the CH_2 data set and the CF_2 data set of $\epsilon_3 = 3.183$. This scaling factor was only applicable to the differential cross section for reactions on carbon in the targets. In order to scale the cross section due to reactions on fluorine nuclei in the CF_2 target, an additional factor of $\frac{1}{2}$ was needed to account for there being twice as many fluorine nuclei as carbon nuclei. Combining the three aforementioned scaling factors gave $\epsilon_{\text{prop}} = \epsilon_1\epsilon_2\epsilon_3 = 1.06 \pm 0.09$ as an overall proportionality factor to scale the carbon-target events in the CF_2 data set from the CH_2 data set. The error on this proportionality factor was treated as a systematic error. It was not included in the statistical error bars on differential cross section plots.

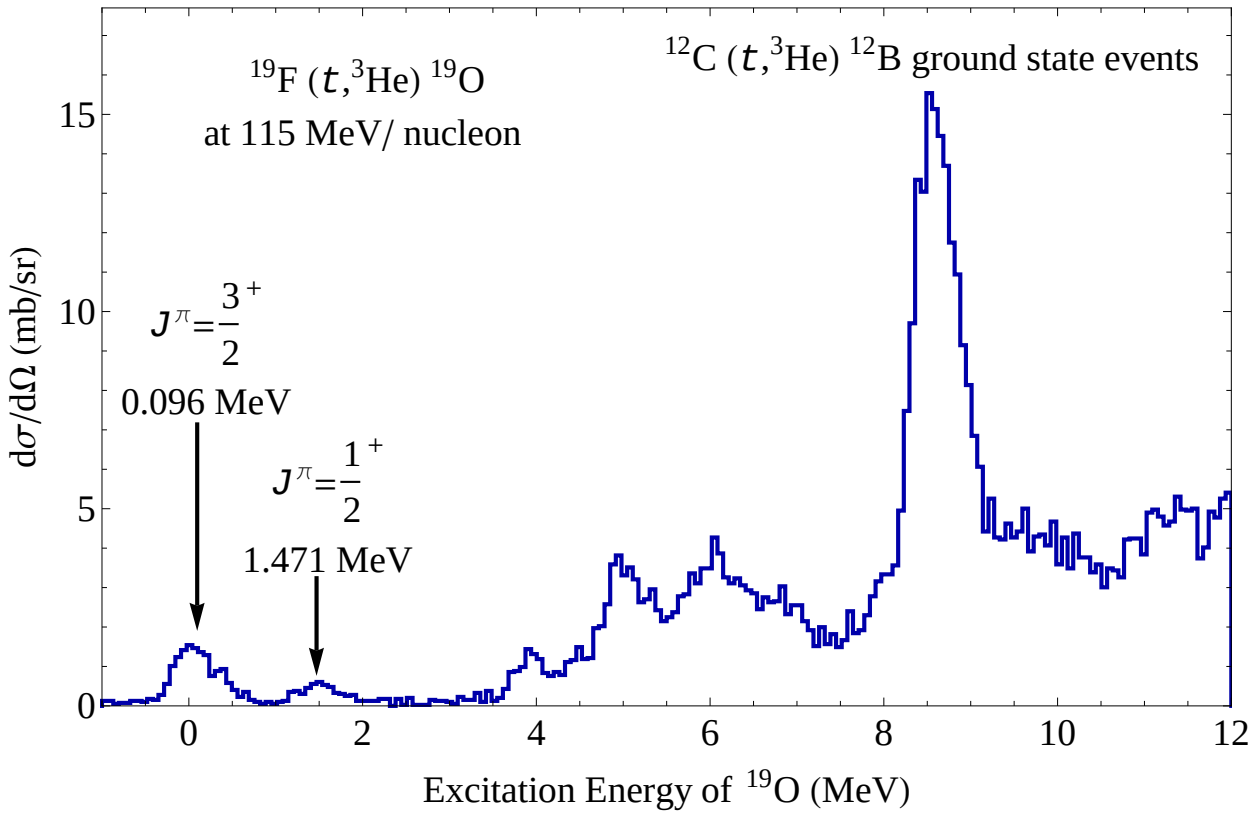

Figure 4.10: This figure shows the scaled absolute cross section for ^{19}O events from the CF_2 target. Note that the ^{12}B events are not subtracted, and are incorrectly scaled by a factor of two in this graph due to the difference in the number of carbon nuclei to fluorine nuclei in the target. This spectrum covers the full angular range of the experiment. Prominent features of the spectrum are marked, including the ^{12}B ground state and two low-lying ^{19}O states.

4.2.3 Isolating the ^{19}F Cross Section

After the proportionality factors ϵ_{abs} and ϵ_{prop} were established to scale the data set from the CF_2 target to an absolute cross section for either target nucleus, final differential cross sections for the $^{19}\text{F}(t,^3\text{He})^{19}\text{O}^*$ reaction were obtained through subtraction of events due to the carbon nuclei in the CF_2 target. This background subtraction was unnecessary over a significant energy range due to the large difference in ground state Q-values for the two reactions. The $^{19}\text{F}(t,^3\text{He})^{19}\text{O}_{g.s.}$ reaction has a Q-value of -4.802 MeV, while the $^{12}\text{C}(t,^3\text{He})^{12}\text{B}_{g.s.}$ reaction has a Q-value of -13.350 MeV. This placed the ground state of ^{12}B at 8.5 MeV above the ground state of ^{19}O on an energy excitation spectrum (see Figure 4.10 for an illustration). Since the experimental resolution was 480 keV, carbon background subtraction was not needed before $E_x\left[^{19}\text{O}\right] = 8$ MeV. No notable hydrogen contamination was visible in the CF_2 data set, but any events related to hydrogen contamination would have sat 4 MeV below the ground state of ^{19}O and so were not a significant concern (the $p(t,^3\text{He})n$ reaction has a Q-value of -0.764 MeV).

For excitation energies of $E_x\left[^{19}\text{O}\right] < 8$ MeV, the following formula was used to obtain the absolute differential cross sections for $^{19}\text{O}^*$ events:

$$\frac{d\sigma}{d\Omega}\left[^{19}\text{O}^*\right] = \left(\frac{N[\text{CF}_2]}{d\Omega \cdot P_{acceptance}}\right)\epsilon_{\text{prop}}\left(\frac{1}{2}\right)\epsilon_{\text{abs}}. \tag{4.2.3}$$

For excitation energies of $E_x\left[^{19}\text{O}\right] \geq 8$ MeV, where carbon background subtraction was necessary, this formula was used instead:

$$\frac{d\sigma}{d\Omega}\left[^{19}\text{O}^*\right] = \left[\left(\frac{N[\text{CF}_2]}{d\Omega \cdot P_{acceptance}}\right)\epsilon_{\text{prop}} - \left(\frac{N[\text{CH}_2]}{d\Omega * P_{acceptance}}\right)\right]\left(\frac{1}{2}\right)\epsilon_{\text{abs}}. \tag{4.2.4}$$

Differential cross sections as a function of scattering angle were created to calculate Gamow-Teller transition strengths. Most of the states in ^{19}O couldn't be clearly separated from each other, so separate angular distributions were generated for different excitation energy bin ranges. For excitation energies of 3.5 MeV $\leq E_x\left[^{19}\mathrm{O}\right] \leq$ 16 MeV, data was divided in 0.5 MeV wide bins, with the bin width roughly reflecting the experimental energy resolution of 480 keV. The two low-lying states of ^{19}O beneath $E_x\left[^{19}\mathrm{O}\right] = 3.5$ MeV were well-separated from other spectrum features, so they were treated differently. For the 0.096 MeV (first excited) state, an energy bin ranging from -0.52 MeV to 0.68 MeV was used; for the 1.471 MeV (second excited) state, a bin range of 0.86 MeV to 2.1 MeV was used. For angular distributions of differential cross sections, binning of the scattering angle was done in increments of 10 mrad in the laboratory frame from 0 mrad to 80 mrad; 10 mrad bins were chosen to reflect the angular resolution achieved in this experiment. Figure 4.11 shows an example of an angular distribution for a differential cross section after carbon background subtraction.

4.3 Calculating Gamow-Teller Strengths

Gamow-Teller transition strengths are extracted from charge-exchange differential cross sections at zero momentum transfer through a well-established proportionality coefficient that is referred to as the unit cross section, shown in Equation 4.3.1 (see also Section 2.1). In this proportionality equation, $\hat{\sigma}_{\mathrm{GT}}$ is the unit cross section, B[GT] is the Gamow-Teller strength, and $\frac{d\sigma}{d\Omega}(q=0)$ is the charge-exchange differential cross section at zero momentum transfer $(q=0)$.

$$\frac{d\sigma}{d\Omega}(q=0) = \hat{\sigma}_{\mathrm{GT}}\left(B[\mathrm{GT}]\right). \tag{4.3.1}$$

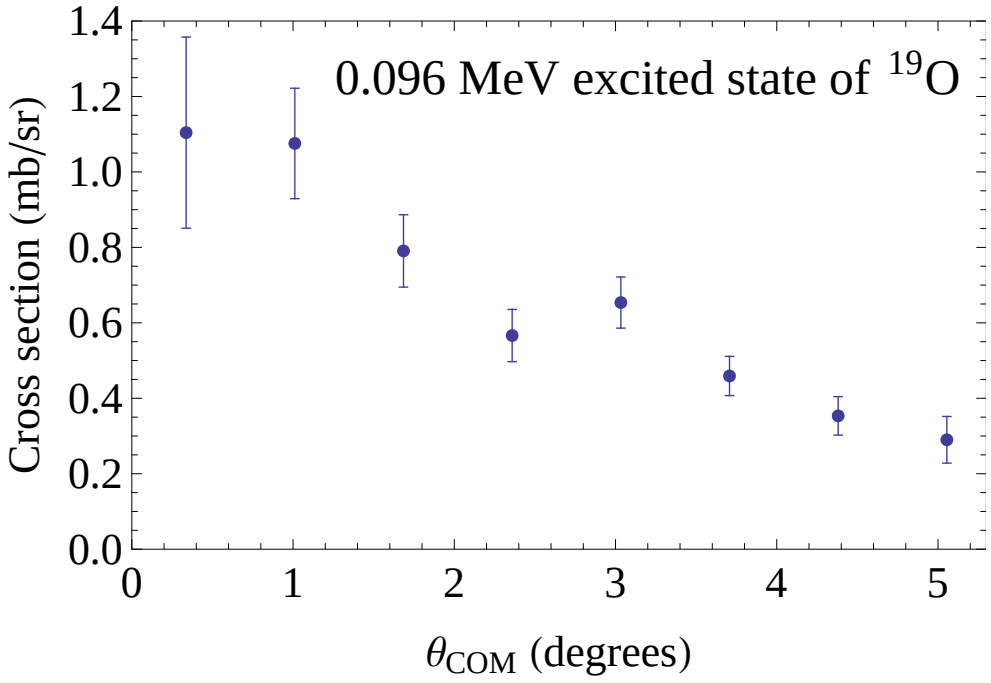

Figure 4.11: This figure displays an angular distribution of the differential cross section for the 0.096 MeV excited state of ^{19}O. This is an example of what the differential cross sections look like after all scalings and corrections were performed and after carbon subtraction was completed.

The differential cross sections extracted in Section 4.2 occurred at a nonzero momentum transfer. Three factors must be taken into account to extract a zero momentum transfer cross section $\left(\frac{d\sigma}{d\Omega}(q=0)\right)$ from the experimentally determined cross sections with finite momentum transfer so that Equation 4.3.1 can be used to determine the Gamow-Teller strength distribution of the ^{19}F(t,^{3}He)^{19}O* reaction. First, the measured (t,^{3}He) reactions can occur at a variety of angular momentum transfers (ΔL), but the Gamow-Teller states only correspond to zero angular momentum transfer ($\Delta L = 0$). A multipole decomposition analysis (MDA) was used to extract the portion of the differential cross section due to only zero angular momentum transfer. Second, the extracted differential cross sections cover a range of scattering angles, but the cross section at a scattering angle of zero ($\theta_{com} = 0^\circ$) is required for the extraction of Gamow-Teller strengths, so this differential cross section value

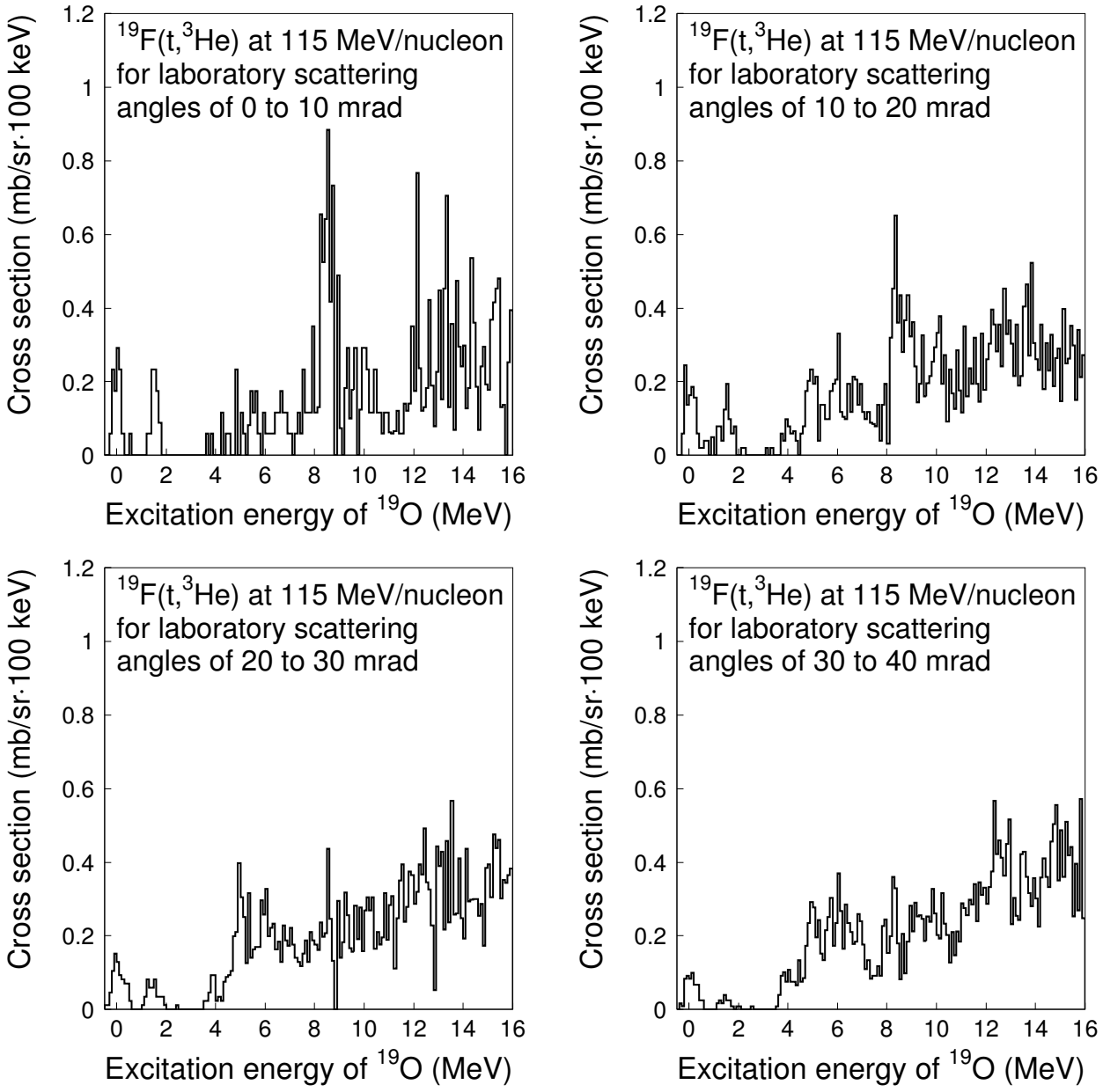

Figure 4.12: These figures show the absolute differential cross sections for the ^{19}F(t,^{3}He) reaction over an excitation energy range in ^{19}O of -0.5 MeV to 16 MeV. Each spectrum covers a different scattering angle range, as listed in the figure. Strong Gamow-Teller states are most visible in the first spectrum, which covers the most forward scattering angles of 0 mrad $\leq \theta_{lab} \leq$ 10 mrad. The figures continue onto the next page.

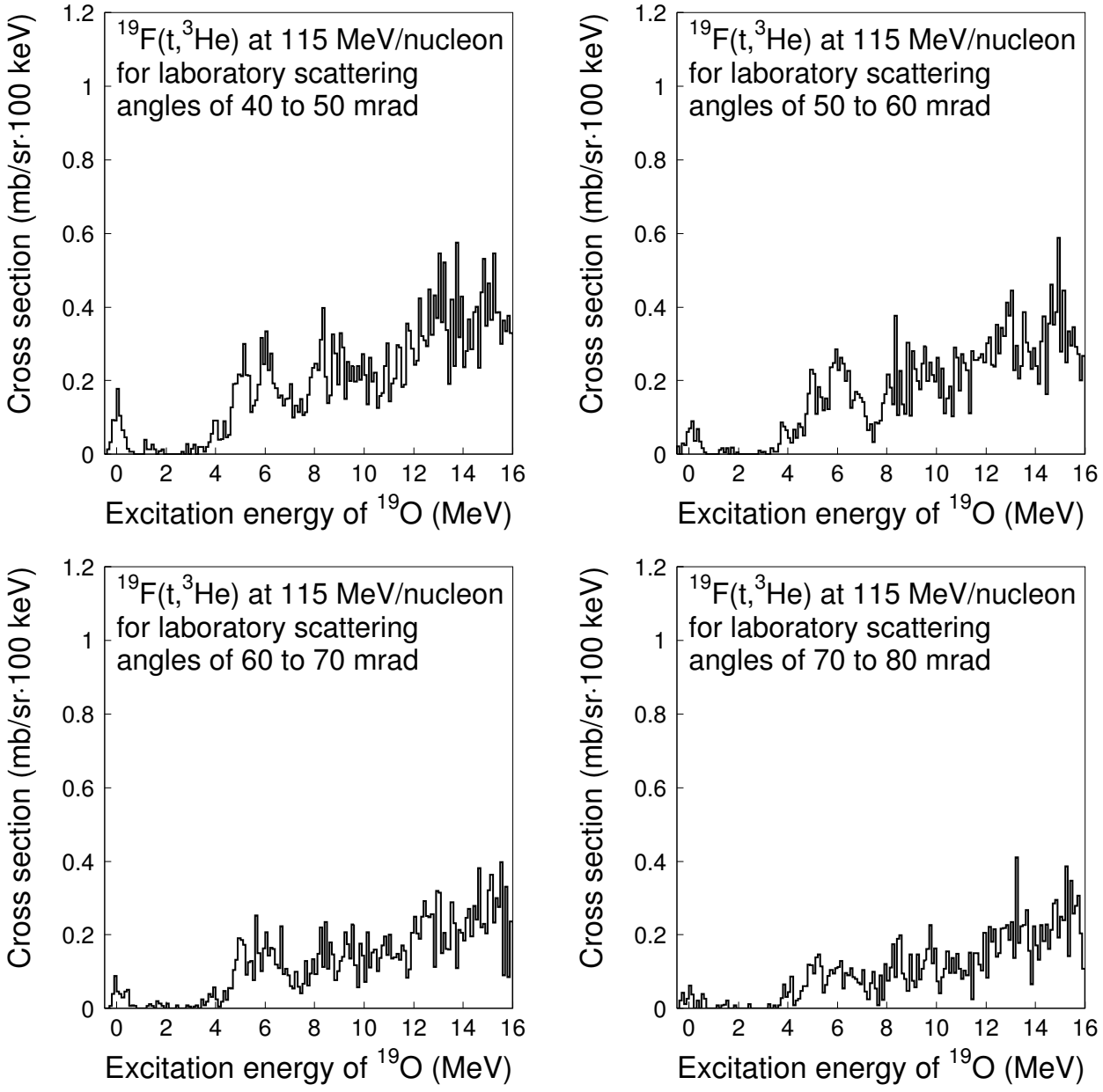

Figure 4.13: These figures are continued from the prior page. They show the absolute differential cross sections for the ^{19}F(t,^{3}He) reaction over an excitation energy range in ^{19}O of -0.5 MeV to 16 MeV. Each spectrum covers a different scattering angle range, as listed in the figure. Strong Gamow-Teller states are most visible in the first spectrum, which covers the most forward scattering angles of 0 mrad $\leq \theta_{lab} \leq$ 10 mrad.

must be extrapolated. The differential cross section angular distributions were extrapolated to $\theta_{com} = 0°$. Third, the measured reactions took place at a nonzero Q-value (-4.802 MeV $\leq Q \leq -20.802$ MeV), so the extracted differential cross section angular distributions were projected to $Q = 0$ to satisfy the zero momentum transfer condition. After these three factors were taken into account to obtain $\frac{d\sigma}{d\Omega}(Q = 0, 0°)$, as described in Section 4.3.1, the final Gamow-Teller strength distribution was calculated in Section 4.3.3.

4.3.1 Multipole Decomposition Analysis

A multipole decomposition analysis (MDA) [40, 48, 71] was used to extract the $\Delta L = 0$ component of the measured differential cross sections. As discussed in Section 2.2, theoretical angular distributions with orbital angular momentum of $0 \leq L \leq 3$ were calculated for transitions in the ^{19}F(t,^{3}He)^{19}O* reaction at selected Q-values. The MDA was performed by fitting a linear combination of the theoretical angular distributions that were generated with a distorted wave Born approximation calculation (see Section 2.2) to the differential cross sections obtained in Section 4.2.2 (see Figure 4.11).

Initial testing of the MDA fit procedure used fits with four variable parameters, one for each possible value of ΔL:

$$\left(\frac{d\sigma}{d\Omega}\right)_{exp} = A\left(\frac{d\sigma}{d\Omega}\right)_{\Delta L=0} + B\left(\frac{d\sigma}{d\Omega}\right)_{\Delta L=1} + C\left(\frac{d\sigma}{d\Omega}\right)_{\Delta L=2} + D\left(\frac{d\sigma}{d\Omega}\right)_{\Delta L=3}, \qquad (4.3.2)$$

where $\left(\frac{d\sigma}{d\Omega}\right)_{exp}$ are the experimentally determined differential cross section data points; the letters A, B, C, and D are variable parameters in the fit, and $\left(\frac{d\sigma}{d\Omega}\right)_{\Delta L=i}$ is one of the possible theoretical angular distributions with an angular momentum of $\Delta L = i$, for i within the range 0–3. Since there are only eight data points available, the fit was restricted to a

maximum of one component per ΔL to preserve some degrees of freedom (ν). The MDA fit procedure was limited to components with $\Delta L \leq 3$ because excitations associated with $\Delta L > 3$ are not expected to be highly populated for low momentum transfers and because their angular distributions peak outside of the angular range of this experiment. However, it was found that in these four-parameter fits, the best fit always had at least one parameter scaled to zero, so the process was expanded to consider several alternative combinations of angular momentum with only two or three varying parameters. Using several different models for the MDA fitting procedure gave insight into the systematic error due to choice of the model.

The best fit (chosen by the χ^2/ν fit parameter) from this MDA process was used as the final set of angular distributions for each differential cross section energy bin. To estimate the systematic error in the MDA procedure, the most extreme fits that still had a probability of being a valid $\geq 5\%$ were used. Here, "extreme fits" refers to the fits that gave the highest and lowest possible values of the $\Delta L = 0$ angular distribution at $\theta_{com} = 0^\circ$, which corresponded to the maximum and minimum possible values of Gamow-Teller strength. These maximum and minimum possible Gamow-Teller strengths were then used as the upper and lower limits of the systematic uncertainty.

Note that this MDA procedure was applied to differential cross sections for excitation energy bins of width 0.5 MeV, ranging from 3.5 MeV to 16 MeV in the excitation energy of ^{19}O. The systematic errors from the choice of the MDA fit model for these excitation energy bins were found to be very large. The possibility of there being no Gamow-Teller strength could not be excluded over this excitation energy range. Despite this, the results of the MDA procedure for these excitation energy bins can be used to provide upper limits on the Gamow-Teller strength distribution.

The two low-lying excited states of ^{19}O at 0.096 MeV and 1.471 MeV are well-separated in the spectra from other transitions, and no transitions with odd values of orbital angular momentum are expected for $E_x < 3$ MeV. The systematic error due to choice of the fit model in these two particular MDA procedures was very small. However, an additional source of systematic error affects the first and second excited states of ^{19}O. Interference between the transition amplitudes due to the $\sigma\tau$ and Tτ (tensor-τ) components of the effective interaction creates a systematic error that cannot be accounted for with only the MDA procedure. This systematic error was estimated with a comparison of theoretical calculations with and without the Tτ interaction by following the procedure described in Reference [42]. The systematic error from the tensor-τ term was found to be 3.4% (0.002) for the first excited state of ^{19}O at 0.096 MeV and 2.0% (0.001) for the second excited state of ^{19}O at 1.471 MeV. Since the systematic error from the MDA is so large for the other extracted Gamow-Teller states, error from the tensor term was ignored as negligible in the reported values for error in Table 4.11 for Gamow-Teller strengths with $E_x \geq 3.5$ MeV.

4.3.2 Extrapolating the Cross Section to $Q = 0$

Once a best fit for the theoretical angular distributions was determined, the differential cross section of the $\Delta L = 0$ component at $\theta_{com} = 0^\circ$ was extracted: $\frac{d\sigma}{d\Omega}(Q_{exp}, 0^\circ)_{experiment}$. The equation used to further extrapolate to $Q = 0$ [39] is:

$$\frac{d\sigma}{d\Omega}(Q = 0, 0^\circ) = \left[\frac{\frac{d\sigma}{d\Omega}(Q = 0, 0^\circ)}{\frac{d\sigma}{d\Omega}(Q_{exp}, 0^\circ)}\right]_{theory} \cdot \left[\frac{d\sigma}{d\Omega}(Q_{exp}, 0^\circ)\right]_{experiment}. \tag{4.3.3}$$

In this equation, the ratio between the theoretical angular distributions at $Q = 0$ and $Q = Q_{exp}$ was used as the basis of the extrapolation. The values calculated for the ratio

$E_x(^{19}\mathrm{O})$ (MeV)	Ratio	$E_x(^{19}\mathrm{O})$ (MeV)	Ratio	$E_x(^{19}\mathrm{O})$ (MeV)	Ratio
0.096	1.043 ‡	7.5–8.0	1.281	12.5–13.0	1.476
1.471	1.113 ‡	8.0–8.5	1.300	13.0–13.5	1.496
3.5–4.0	1.124	8.5–9.0	1.320	13.5–14.0	1.515
4.0–4.5	1.144	9.0–9.5	1.340	14.0–14.5	1.535
4.5–5.0	1.164	9.5-10.0	1.359	14.5–15.0	1.554
5.0–5.5	1.183	10.0–10.5	1.378	15.0–15.5	1.574
5.5–6.0	1.203	10.5–11.0	1.398	15.5–16.0	1.593
6.0–6.5	1.222	11.0–11.5	1.417		
6.5–7.0	1.242	11.5–12.0	1.437		
7.0–7.5	1.261	12.0-12.5	1.456		

Table 4.10: This table lists the ratios that were calculated to extrapolate the differential cross section at a finite reaction Q-value to $Q = 0$ in order to fulfill the condition of zero momentum transfer in Equation 4.3.1 and calculate Gamow-Teller transition strengths, as discussed in the text. The ‡ indicates that, for the first two excited states of ^{19}O, the precise calculated ratio was used instead of a value interpolated from the fit.

of $\left[\frac{\frac{d\sigma}{d\Omega}(Q=0,0^\circ)}{\frac{d\sigma}{d\Omega}(Q_{exp},0^\circ)}\right]_{theory}$ for each Gamow-Teller transition were then used to construct a linear fit so that values of this ratio could be obtained for an arbitrary energy bin. The values used for this ratio in the calculation of the Gamow-Teller strength distribution are listed in Table 4.10. For the first two excited states of ^{19}O, the precise calculated ratio was used instead of a value interpolated from the fit.

4.3.3 Gamow-Teller Strength Distribution

With an extracted value for $\frac{d\sigma}{d\Omega}(Q = 0, 0^\circ)$, the only variable needed in Equation 4.3.1 to find the Gamow-Teller strength is the unit cross section ($\hat{\sigma}_{\mathrm{GT}}$). The unit cross section was calculated from a global fit of $\hat{\sigma}_{\mathrm{GT}}$ as a function of nuclear mass (A) that was performed in Reference [38]:

$$\hat{\sigma}_{\mathrm{GT}} = \frac{109}{A^{0.65}}, \tag{4.3.4}$$

where A is the mass number of the target nuclei. This fit has an error of 5% [38]. This equation gives $\hat{\sigma}_{\mathrm{GT}} = 16.1 \pm 0.8$ mb/sr for the ^{19}F(t,^{3}He) reaction. The error in the unit cross section was treated as a systematic error.

Gamow-Teller strengths were then calculated with equation 4.3.1. The Gamow-Teller strength distribution for the ^{19}F(t,^{3}He)^{19}O* reaction at 115 MeV (and associated errors) are listed in Table 4.11. The transition from the ground state of ^{19}F to the first excited state of ^{19}O at 0.096 MeV was found to have a Gamow-Teller strength of B[GT] $= 0.068^{+0.011}_{-0.009}$. The error in this figure is discussed in greater detail in Section 5.3 and this result for Gamow-Teller strength is further discussed in Section 5.1 in the context of its application to fluorine nucleosynthesis. The transition from the ground state of ^{19}F to the second excited state of ^{19}O at 1.471 MeV was found to have a Gamow-Teller strength of B[GT] $= 0.057^{+0.011}_{-0.010}$. The results of the MDA fitting process for these two low-lying states are shown in Figures 4.14 A and B, respectively. A Gamow-Teller strength distribution was extracted for higher lying strength for 3.5 MeV $\leq E_x \leq$ 16 MeV in ^{19}O as well. However, the systematic error on these Gamow-Teller strengths is large enough that B[GT] $= 0$ cannot be excluded. Additionally, the statistical error for the Gamow-Teller strengths in the excitation energy bins with 8.0 MeV $\leq E_x \leq$ 16 MeV in ^{19}O are significantly larger than those with $E_x <$ 8.0 MeV because of the carbon background subtraction process discussed in Section 4.2.3.

The Gamow-Teller strength distribution was also compared to theoretical calculations of Gamow-Teller strength. These theoretical Gamow-Teller strength distributions were calculated using the shell-model code OXBASH [50] in the *sd* model space with the USDB [72] interaction and in the *spsdpf* model space with the WBP [54] interaction. The calculated Gamow-Teller strengths from OXBASH are listed in Table 4.12. Figures 4.15 A and B show comparisons between these two different theoretical Gamow-Teller strength distribu-

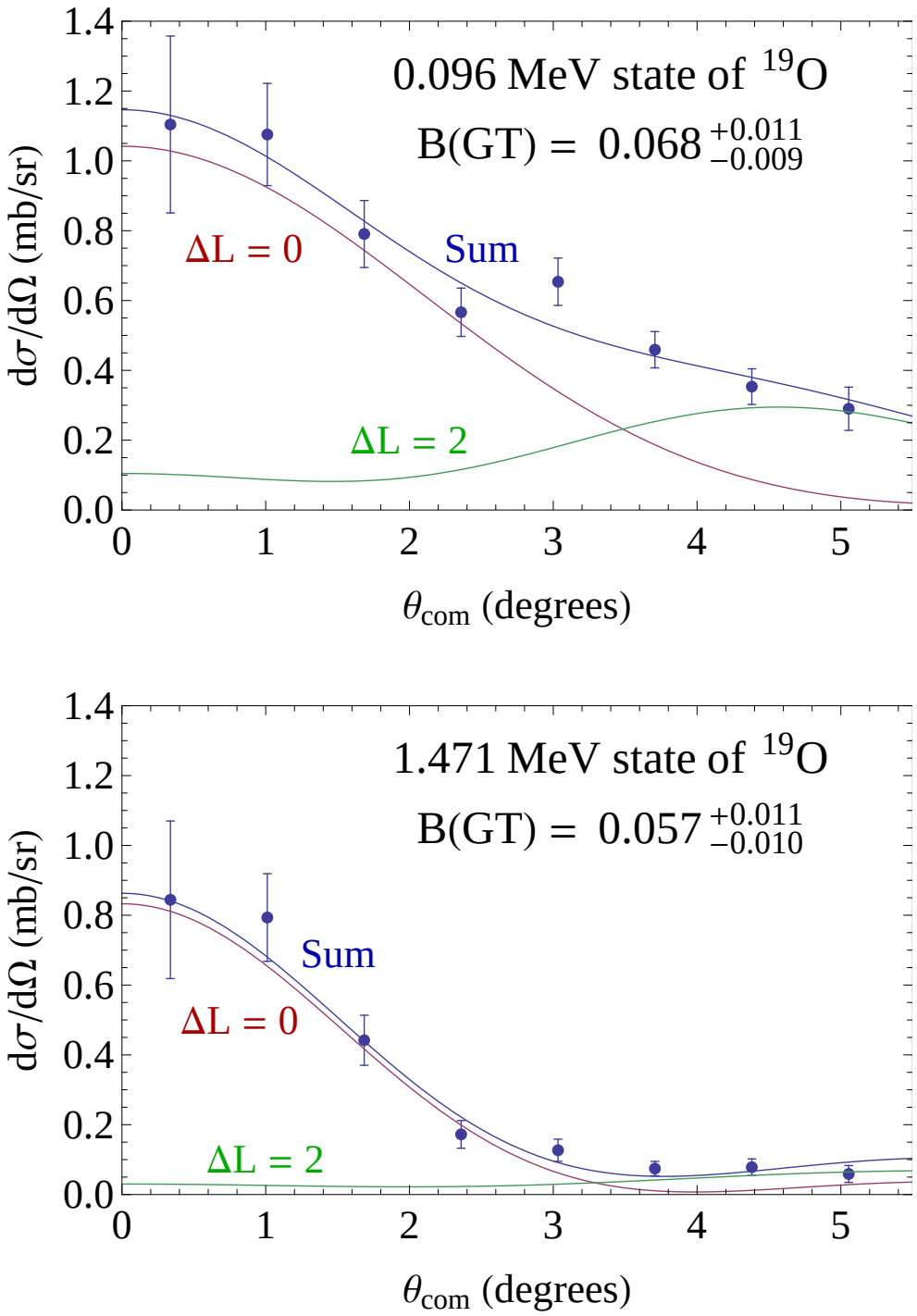

Figure 4.14: These figures show the results of the multipole decomposition analysis for the first two excited states of ^{19}O. The blue circles are data points with statistical error bars. Figure A shows the decomposition of the 0.096 MeV first excited state of ^{19} and Figure B shows the decomposition of the 1.471 MeV second excited state. The red lines are $\Delta L = 0$ components of the angular distribution, used for determining the Gamow-Teller strength of each state. The green lines are $\Delta L = 2$ components of the angular distribution from quadrupole transitions. The blue lines are sums of the separate components.

tions and the distribution extracted in this work. When comparing theoretical Gamow-Teller strengths to experimental Gamow-Teller strengths, it is expected that the theoretical Gamow-Teller strengths will need to be quenched by a factor of $(0.77)^2$, as discussed in References [42, 73, 74, 75]. This factor accounts for the degrees of freedom not considered in the shell model calculations. When quenching is applied, the WBP interaction comes closest to reproducing the experimentally determined Gamow-Teller strength of the first excited state in ^{19}O at 0.096 MeV; the quenched strength of the WBP interaction is 1.1 standard deviations from experiment, while the quenched strength of the USDB interaction is 2.1 standard deviations from the Gamow-Teller strength found experimentally. Both interactions do a poor job of reproducing the Gamow-Teller strength of the second excited state in ^{19}O at 1.471 MeV; their quenched strengths are 4.1 (for the WBP interaction) and 4.4 standard deviations (for the USDB interaction) from the Gamow-Teller strength found experimentally.

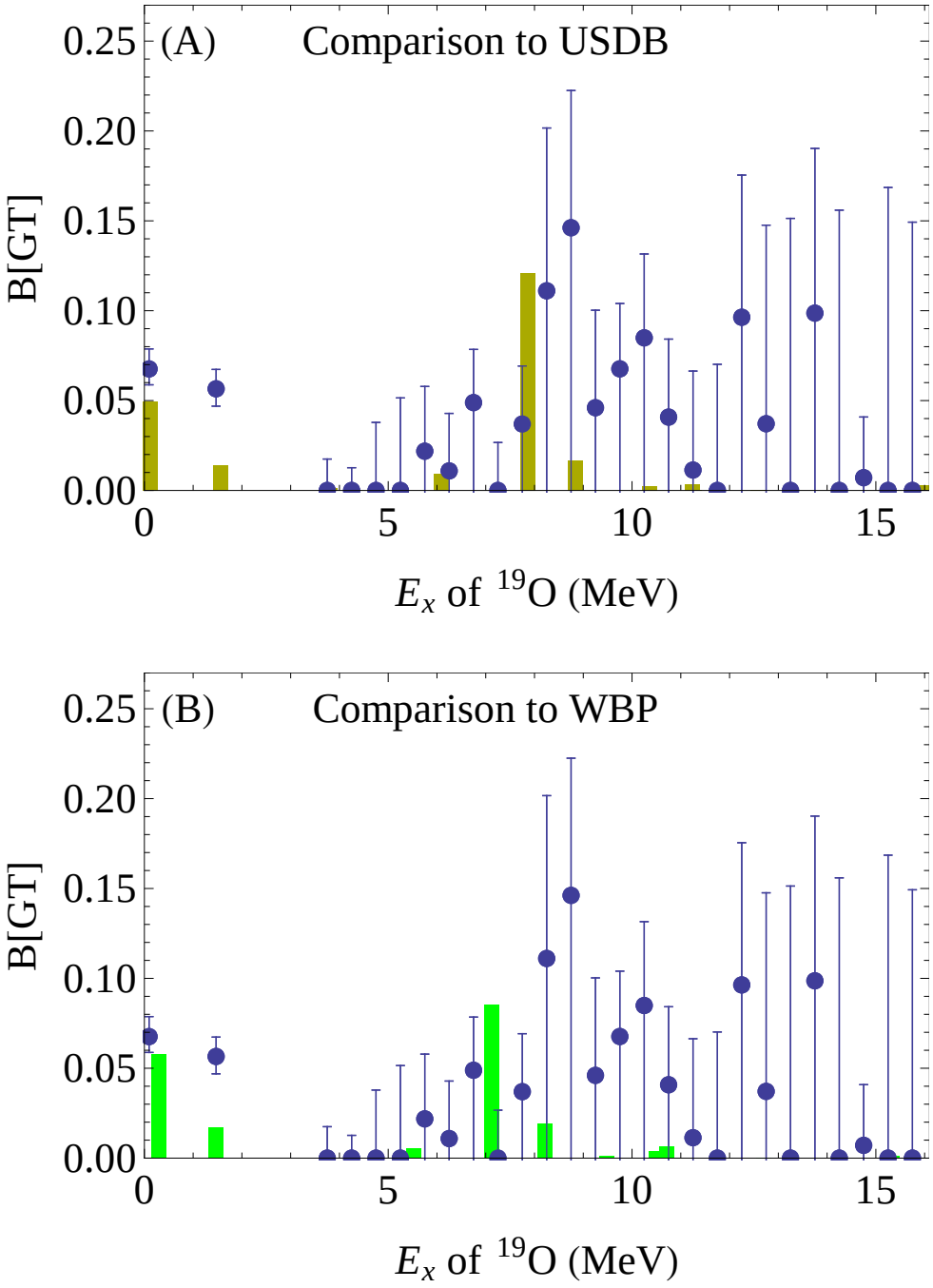

Figure 4.15: These figures show comparisons between theoretical and experimentally extracted Gamow-Teller strength distributions. Figure A compares the Gamow-Teller strengths extracted in this experiment (blue points) with the strength distribution produced with the USDB [72] interaction (yellow bars) in the *sd* model space. Figure B compares the Gamow-Teller strengths extracted in this experiment (blue points) with the strength distribution produced with the WBP [54] interaction (green bars) in the *spsdpf* model space. Both theoretical strength distributions were calculated with OXBASH [50]. In both cases, the theoretical Gamow-Teller strengths are quenched by a factor of $(0.77)^2$ as discussed in the text.

E_x [^{19}O] (MeV)	B[GT]	B[GT] Error (+)	B[GT] Error (−)
0.096	0.068	0.011	0.009
1.471	0.057	0.011	0.010
3.5–4.0	0	0.018	0
4.0–4.5	0	0.013	0
4.5–5.0	0	0.038	0
5.0–5.5	0	0.052	0
5.5–6.0	0.022	0.036	0.028
6.0–6.5	0.011	0.032	0.017
6.5–7.0	0.049	0.030	0.058
7.0–7.5	0	0.027	0
7.5–8.0	0.037	0.032	0.045
8.0–8.5	0.111	0.091	0.132
8.5–9.0	0.146	0.076	0.172
9.0–9.5	0.046	0.054	0.059
9.5-10.0	0.068	0.036	0.080
10.0–10.5	0.085	0.047	0.096
10.5–11.0	0.041	0.043	0.053
11.0–11.5	0.011	0.055	0.025
11.5–12.0	0	0.070	0
12.0-12.5	0.096	0.079	0.111
12.5–13.0	0.037	0.111	0.058
13.0–13.5	0	0.151	0
13.5–14.0	0.099	0.092	0.118
14.0–14.5	0	0.156	0
14.5–15.0	0.007	0.034	0.026
15.0–15.5	0	0.169	0
15.5–16.0	0	0.149	0

Table 4.11: This table lists the calculated Gamow-Teller strengths for the ^{19}F(t,^{3}He)^{19}O* reaction at 115 MeV. Associated errors are also listed.

	WBP		USDB	
J^π	E (MeV)	B[GT]	E (MeV)	B[GT]
$\frac{3}{2}^+$	0.29	0.0979	0.12	0.0835
$\frac{1}{2}^+$	1.47	0.0286	1.57	0.0234
$\frac{3}{2}^+$	3.75	0.0017	3.80	0.0018
$\frac{3}{2}^+$	5.53	0.0096	6.08	0.0155
$\frac{1}{2}^+$	7.13	0.1445	7.86	0.2036
$\frac{3}{2}^+$	8.22	0.0328	8.84	0.0282
$\frac{3}{2}^+$	9.48	0.0025	10.36	0.0036
$\frac{3}{2}^+$	10.49	0.0070	11.28	0.0003
$\frac{1}{2}^+$	10.72	0.0114	11.24	0.0058
$\frac{3}{2}^+$	12.71	0.0006	12.58	0.0000
$\frac{1}{2}^+$	15.34	0.0018	16.06	0.0045
$\frac{1}{2}^+$	16.02	0.0001	16.71	0.0001

Table 4.12: This table lists the predicted Gamow-Teller strengths for transitions in the ^{19}F(t,^{3}He)^{19}O* reaction for two different interactions, USDB [72] and WBP [54], along with the predicted energy level for each transition. These calculations were both performed with the shell-model code OXBASH [50] in the *sd* model space. These values are all unquenched; when used in calculations, a quenching factor of $(0.77)^2$ should be applied as described in the text.

Chapter 5

Results

5.1 β-decay Rate Calculation

As discussed in Section 1.3, the Gamow-Teller strengths of the ^{19}F(t,^{3}He)^{19}O* reaction have an application in fluorine nucleosynthesis. In hot stellar environments, it is possible to thermally populate low-lying excited states of ^{19}O*. These excited states are not accessible to a traditional β-decay experiment because they de-excite by γ-ray emission in nanoseconds, whereas the β-decays of interest take place on a time scale of several seconds. As discussed in Reference [26] and in Section 1.3, the lowest-lying excited state of ^{19}O at 0.096 MeV potentially makes a significant impact on the total β-decay rate of stellar ^{19}O. This particular excited state at 0.096 MeV is allowed to β-decay to the ground state of ^{19}F directly, whereas the ^{19}O ground state to ^{19}F ground state is a second forbidden ($\Delta\pi = 0$, $\Delta L = 2$) β-decay by spin-parity considerations (see Figure 1.2 for the relevant level scheme).

In Section 4.3.3, the extracted Gamow-Teller strength of the transition from the ground state of ^{19}F to the 0.096 MeV first excited state of ^{19}O was found to be B[GT] $= 0.0676^{+0.011}_{-0.009}$. This Gamow-Teller strength can be used to determine the weak interaction rate for the transition from the 0.096 MeV state in ^{19}O to the ground state of ^{19}F. To account for the fact that this measured Gamow-Teller strength is for the ^{19}F $\rightarrow$^{19}O ($A \rightarrow B$) direction while the weak decay proceeds in the opposite ^{19}O $\rightarrow$^{19}F ($B \rightarrow A$) direction, the Gamow-Teller

strength must be scaled by a factor of:

$$F = \frac{(2J_A + 1)}{(2J_B + 1)}, \tag{5.1.1}$$

where $J_A = \frac{1}{2}$ for the total angular momentum of the transition state in the fluorine nucleus, $J_B = \frac{3}{2}$ for the total angular momentum of the transition state in the oxygen nucleus, for a scaling factor of $F = 0.5$. It is possible to decay to other states in ^{19}F from the 0.096 MeV state in ^{19}O, but those transitions were not accessible via the experiment performed in this dissertation. There are five total energy levels in ^{19}F with an allowed spin-parity for β-decay reactions and within the permitted Q-value range of such a β-decay; these ^{19}F energy levels are listed in Table 5.1.

Theoretical shell-model calculations are used to determine the Gamow-Teller strengths for decay transitions that go from the 0.096 MeV state in ^{19}O to an excited state i in ^{19}F (listed in Table 5.1). These theoretical Gamow-Teller strengths allow for an estimate of the branching ratios (I_i) for each allowed transition. The shell-model calculations to obtain theoretical Gamow-Teller strengths were performed in the *sd*-model space with the USDB interaction [72] with the code OXBASH [50]. It is difficult to assign an error to the theoretical Gamow-Teller strengths. Fortunately, the main role of the theoretical Gamow-Teller strengths in this calculation is only to determine a branching ratio for the possible β-decay transitions, and that branching ratio is dominated ($I_{exp} = 86\%$) by the measured transition. Several different assumptions for the error on the theoretical Gamow-Teller strengths were tested ranging up to 100% error, and it was found to have only a small influence on the error of the final β-decay rate calculation. Ultimately, the theoretical Gamow-Teller strengths were assigned an error of 36% because that corresponds to the variation found between the Gamow-Teller

^{19}F Energy Level (MeV)	J^π	Q-value (MeV)	B[GT] USDB	Quenched B[GT] USDB
0.000	$\frac{1}{2}^+$	4.918	0.04177 ‡	0.0248 ‡
0.197	$\frac{5}{2}^+$	4.721	0.00064	0.0004
1.554	$\frac{3}{2}^+$	3.364	0.04538	0.0269
3.908	$\frac{3}{2}^+$	1.010	0.39516	0.2343
4.550	$\frac{5}{2}^+$	0.368	0.49186	0.2916

Table 5.1: This table lists the energy levels and associated spin-parity assignments of the states in ^{19}F that are relevant for weak reaction rate calculations for the β-decay of the 0.096 MeV excited state in ^{19}O ($J^\pi = \frac{3}{2}^+$). Q-values for β-decays from the 0.096 MeV state in ^{19}O are listed in the third column. Gamow-Teller theoretical strengths (quenched by a factor of $(0.77)^2$ [73, 74, 75, 42], discussed in Section 4.3.3) are listed as well. The ^{19}F energy levels and spin-parity assignments were taken from Reference [25]. The ‡ denotes that this theoretical Gamow-Teller strength is not actually used in further calculations, because it is replaced with the measured value B[GT] $= 0.034^{+0.006}_{-0.004}$ (with $F = 0.5$ as discussed in the text) for this transition from Section 4.3.3.

strength measured in this experiment and its corresponding (quenched; see Section 4.3.3) theoretical value from the USDB interaction. The USDB interaction was chosen for this purpose because it is generally regarded as a better model for *sd*-shell isotopes, even though in this case it performed worse than the WBP interaction (see Section 4.3.3). In practice, the choice of interaction in this calculation had no significant effect on the outcome.

Gamow-Teller strengths can be related to ft-values via the equation:

$$ft = \frac{\left(\frac{K}{g_v^2}\right)}{\mathrm{B[GT]}\left(\frac{g_a}{g_v}\right)^2}, \tag{5.1.2}$$

where $\frac{K}{g_v^2} = 6143 \pm 2$ s and $\frac{g_a}{g_v} = -1.2694 \pm 0.0028$ [39]. Once an ft-value is calculated for specific transition to a final state i, it can be related to the partial half-life (t_i) and the partial decay rate λ_i via the equations [2, 76]:

$$t_i = 10^{\left[\log(ft)_i - \log(f)_i\right]} \text{ and} \tag{5.1.3}$$

$$\lambda_i = \frac{\ln(2)}{t_i}, \tag{5.1.4}$$

where $\log(f)_i$ is a calculated value based on the Q-value of the β-decay reaction, the type of β-decay (a β^+ reaction vs. a β^- reaction, and whether the decay is allowed or forbidden), and the proton number (Z) of the daughter nucleus. The $\log(f)_i$ values used in these weak reaction rate calculations were interpolated from tables in Reference [76], and any error in them was considered to be negligible.

For the set λ_i of β-decay transitions from a single specific state a in ^{19}O to the set i of

allowed states in ^{19}F, the branching ratio to each state i (I_i) is [76]:

$$\mathrm{I}_i = \frac{\lambda_i}{\sum_i \lambda_i}, \tag{5.1.5}$$

and the overall half-life ($\mathrm{T}_{1/2,a}$) and weak decay rate (λ_a) for all decays from the state a are found from [2]:

$$\mathrm{T}_{1/2,a} = \mathrm{I}_i * t_i \text{ for any state } i \text{ and} \tag{5.1.6}$$

$$\lambda_a = \frac{\lambda_i}{\mathrm{I}_i} \text{ for any state } i. \tag{5.1.7}$$

From these equations, the final β^- decay rate from the 0.096 MeV first excited state in ^{19}O was found to be $\lambda_x = 0.038^{+0.011}_{-0.008}$ s^{-1} (which corresponds to $\mathrm{T}_{1/2} = 18^{+5}_{-4}$ s). See Table 5.2 for the intermediate calculation values. The errors in this calculation were handled through standard error propagation formula and are discussed in greater detail in Section 5.3, especially Section 5.3.4. Errors in the $\log(f)_i$ values were negligible.

The Boltzmann distribution gives the probability P_j for a nucleus in a stellar environment with temperature T to be in an excited state j with spin J_j and excitation energy E_j as [2]:

$$\mathrm{P}_j = \frac{(2J_j+1)\, e^{\left(\frac{-E_j}{kT}\right)}}{\sum_j (2J_j+1)\, e^{\left(\frac{-E_j}{kT}\right)}}, \tag{5.1.8}$$

where k is the Boltzmann constant, which has a value of $k = 8.6173 \times 10^{-2}$ MeV/T_9 [2]. The temperature notation T_9 is used frequently in astrophysics in place of GK; 1.0 T_9 is equivalent to 10^9 kelvin. The fluctuation in the population of the ground and 0.096 MeV first excited state of ^{19}O is pictured in Figure 5.1. As expected, at low temperatures around

E_f [^{19}F] (MeV)	J^π	B[GT]	Error in B[GT]	log(ft)	log(f)	λ (s^{-1})	I (%)
0.000	$\frac{1}{2}^+$	0.034 ‡	$^{+0.006}_{-0.004}$	5.05	3.73	0.033	86.0
0.197	$\frac{5}{2}^+$	0.0004	0.0001	7.00	3.65	0.00032	0.8
1.554	$\frac{3}{2}^+$	0.027	0.007	5.15	2.99	0.0048	12.5
3.908	$\frac{3}{2}^+$	0.23	0.06	4.21	0.77	0.00025	0.7
4.550	$\frac{5}{2}^+$	0.29	0.08	4.12	-0.87	7.2E-6	0.02

Table 5.2: This table shows intermediate calculation stages used to determine a β^- decay rate (λ_x) for the 0.096 MeV first excited state of ^{19}O. The first column lists the energy level of a possible final state for this β-decay in ^{19}F. ‡: This particular Gamow-Teller strength was extracted from the experiment performed for this dissertation. The other B[GT] values in this column were determined from shell-model calculations as described in the text. The log(f) values were interpolated from tables in Reference [76].

$T_9 = 0.1$, no significant amount of ^{19}O is in the first excited state. At $T_9 = 0.4$, the excited state starts to account for $P_x = 4\%$ of the total ^{19}O population. At $T_9 = 1.6$, the excited state accounts for a more noticeable $P_x = 25\%$ of the total ^{19}O population, and it levels off near $P_x = 36\%$ over the rest of the relevant stellar temperature range. For this calculation, higher excited states of ^{19}O are ignored. Their impact was examined separately, and they have only a minor impact on the excited state populations; the second excited state at 1.471 MeV only makes up 3% of the ^{19}O population at $T_9 = 10.0$.

Looking at only the ground state (subscript $g.s.$) and first excited state (subscript x) β-decay of ^{19}O, the total decay rate λ_{tot} as a function of temperature (T) is [2]:

$$\lambda_{\text{tot}} = \sum_j \mathrm{P}_j \lambda_j = \mathrm{P}_{g.s.}(T)\lambda_{g.s.} + \mathrm{P}_x(T)\lambda_x \tag{5.1.9}$$

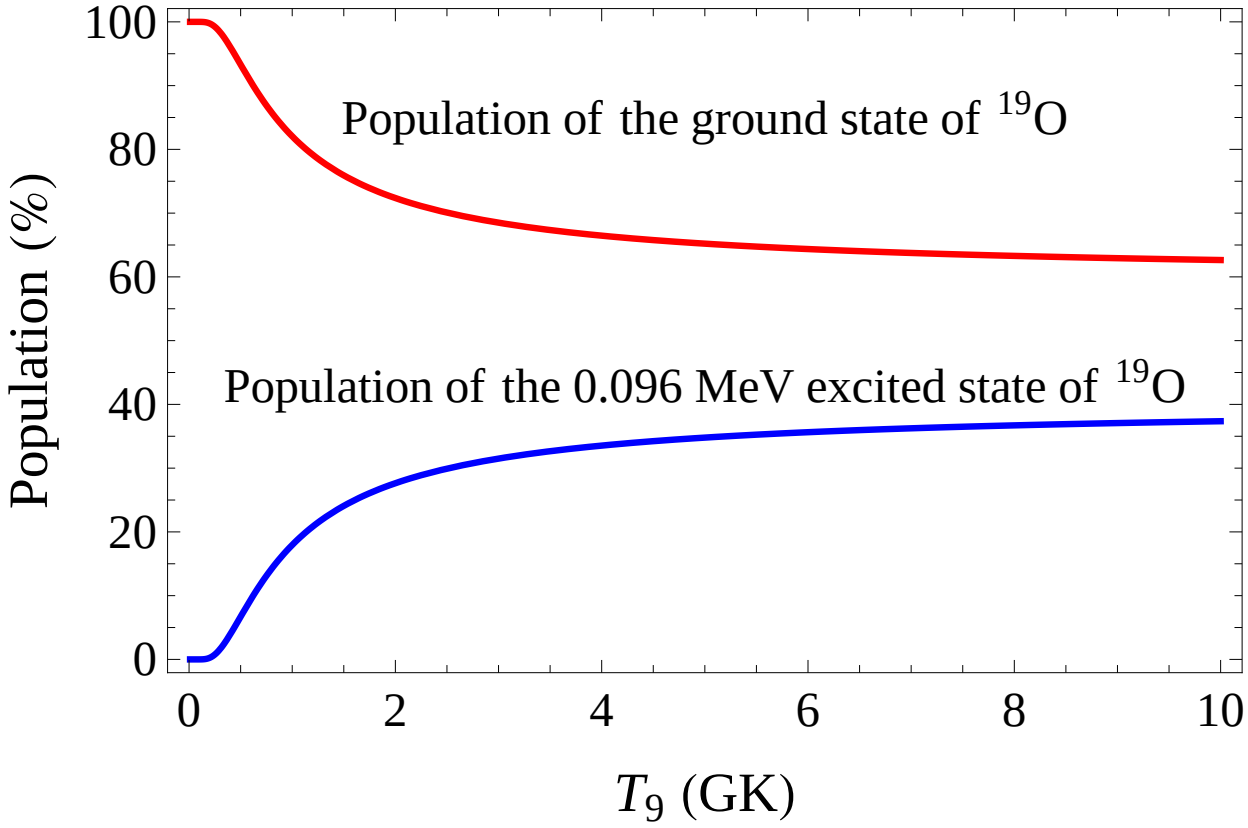

Figure 5.1: This figure shows the population of the ground state and first excited state of ^{19}O over a stellar temperature range. The red line indicates the percentage of ^{19}O in the ground state at temperature T. The blue line indicates the percentage of ^{19}O in the first excited state at 0.096 MeV for a given temperature. The first excited state is rapidly populated around $T_9 = 1.6$ and levels off near 36% for $T_9 > 2$.

The β-decay rate for the ground state of ^{19}O is known from direct β-decay measurements to be $\lambda_{g.s.} = 0.02571 \pm 0.00007$ s^{-1}, which equates to $T_{1/2} = 26.96 \pm 0.07$ s [25] (see also Table 5.3).

5.2 Conclusions

As Figure 5.2 illustrates, the increase in the total β-decay rate (λ_{tot}) over a range of astrophysical temperatures is modest. At the top of the temperature range, this new rate (λ_{tot}) increases 18% beyond the ground state reaction rate ($\lambda_{g.s}$). This small rate increase is unlikely to have a significant influence on astrophysical simulations of fluorine production. It is worthwhile to note that the ^{19}O$(\beta^-)^{19}$F reaction is neglected entirely in many fluorine nucleosynthesis simulations. Inclusion of this fluorine production mechanism has the potential to increase simulated fluorine yields, even though the rate enhancement examined in this work was found to be relatively small.

Recall from Section 1.3 that a theoretical calculation of this same rate by Chernykh *et al.* [26] yielded an increase of up to a factor of three. The large discrepancy between the calculation in Reference [26] and those presented here results deserves scrutiny. The measured Gamow-Teller strength of the ^{19}O$_{[0.096\text{ MeV}]}(\beta^-)^{19}F_{g.s.}$ transition was found to be B[GT] $= 0.034^{+0.006}_{-0.004}$. In Figure 4.15 and Section 4.3.3, the experimentally determined Gamow-Teller strength was compared to OXBASH [50] calculations in the USDB [72] and WBP [54] interaction, which gave quenched (unquenched) values of 0.0248 (0.0418) and 0.0289 (0.0490) respectively in the ^{19}O $\rightarrow^{19}$ F direction. This means that the experimentally determined Gamow-Teller strength is 2.0 standard deviations from the Gamow-Teller strength predicted with the USDB [72] interaction and 1.1 standard deviations from the

E_i (MeV)	I_i (%)	$\log ft$	B[GT] (estimated)
0.000	≤ 4	≥ 6.5	≤ 0.0012
0.197	45.4	5.384	0.0157
1.554	54.4	4.625	0.0904

Table 5.3: This table shows experimental β-decay information for $^{19}O_{g.s.}(\beta^-)^{19}F^*$. The decay to the ground state of ^{19}F is forbidden; the branching ratios listed here were calculated without considering forbidden states. These values were taken from Reference [25].

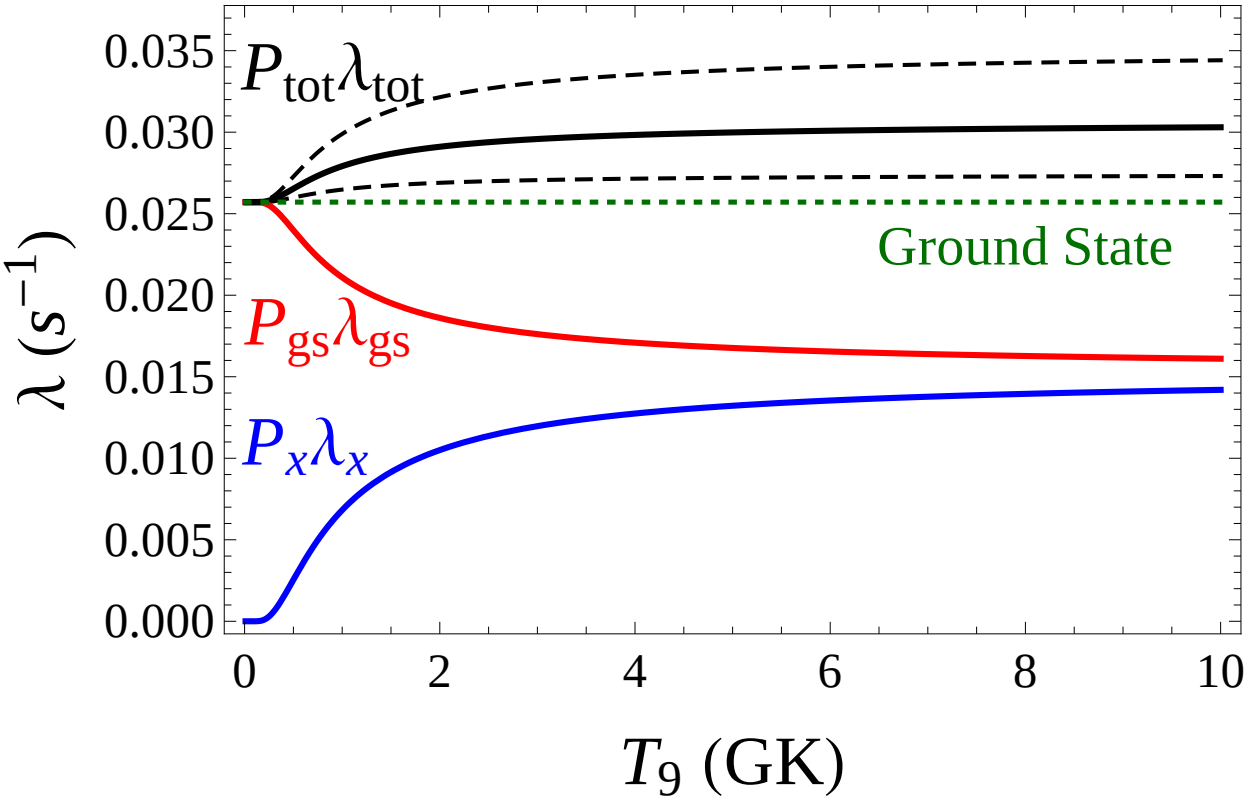

Figure 5.2: This graph shows the temperature dependence of the β-decay rate for $^{19}O(\beta^-)^{19}F$. The green dotted line indicates the β-decay rate for ^{19}O in the ground state, which was known from prior experiments [25]. The solid black line shows λ_{tot}, the new rate determined in this work for β-decays from either the ground or first excited state of ^{19}O. The black dashed lines indicate the error in this new decay rate. The red and blue lines indicate the contribution to the new rate from the ground and first excited state, respectively. The black line is the sum of the red and blue lines. As the blue line indicates, the first excited state doesn't contribute much to the new decay rate at low temperatures because the excited state isn't heavily populated. At higher temperatures, the excited state contributes nearly as much as the ground state to the total β-decay rate.

Gamow-Teller strength predicted with the WBP [54] interaction. Theoretical calculations of B[GT] values in Chernykh *et al.*'s work used different interactions: CW, HBUMSD, and HBUSD [75] with Gamow-Teller strengths of 0.0290, 0.0456, and 0.0333 respectively. These Gamow-Teller strengths are also fairly close to the experimentally determined value. No quenching factor was taken into account in Chernykh *et al.*'s work, which inflates the β-decay rate (λ_{tot}) by 70%, but does not account for the overall discrepancies between the decay rates. Another slight difference between the decay rate in this work and Reference [26] is that this work uses the experimentally determined value of $\lambda_{g.s.}$ while Chernykh *et al.* use a theoretical calculation of $\lambda_{g.s.}$, but the effect of this difference in approach is small.

Since the discrepancy between decay rates for this work and Chernykh *et al.*'s work does not arise from a conflict between experimental measurement and theoretical predictions of Gamow-Teller strength, it is difficult to determine exactly where it comes from. A close examination of the calculations available in Reference [26] suggests that there was an error in Chernykh *et al.*'s calculation of the Boltzmann distribution (Equation 5.1.8).

The new experimentally determined rate (λ_{tot}) presented in this work is available for future studies of fluorine nucleosynthesis that involve the $^{19}\text{O}(\beta^-)^{19}\text{F}$ reaction. Additionally, the Gamow-Teller strength distribution presented in 4.3.3 provides boundaries to guide future studies of $^{19}\text{F}_{g.s.}$ to $^{19}\text{O}^*$ transitions and to constrain shell-model calculations.

5.3 Discussion of Error Sources

There are many potential sources of error in a complex experiment like this one. Brief notes have been included throughout this dissertation to address sources of error as they appear. However, it is helpful to have a comprehensive review of how all known error

sources are handled. This section discusses all errors associated with the factors used in the data analysis of Chapter 4 and in the calculation of the β-decay rate for the transition from the 0.096 MeV first excited state in ^{19}O to the ground state of ^{19}F in Section 5.1.

5.3.1 Experimental Errors

There are many possible sources of experimental error. This section examines potential errors in any part of the experiment or data analysis up to the conversion from experimental count rates to differential cross sections (Chapter 3 and Section 4.1).

Ultimately, only the statistical error of the measurement was considered a significant source of error in this portion of the data analysis. Other errors were disregarded as negligible because it was possible to verify the results of the data analysis for Section 4.1 by looking at data taken on the CH_2 calibration target. The cross section that was produced for the ^{12}C(t,^{3}He)^{12}B* reaction was compared to a prior measurement of this same reaction in experiment 06032 (see Section 4.2.2) and the results were in good agreement. This indicated that any uncertainties in Section 4.1 of the data analysis procedure must be relatively minor. This validation process also indicated that there were no significant problems with the experimental apparatus that was described in Chapter 3.

Resolutions were the only other significant factor in the experiment. The scattering angle resolution of the S800 spectrograph was 10 mrad in the laboratory frame; this was dominated by the large beam spot size and thickness of the target. The energy resolution of the S800 spectrograph was found to be 480 keV for this experiment by examining the width of the peak for the $^{12}C_{g.s.}$(t,^{3}He)$^{12}B_{g.s.}$ transition. This energy resolution was lower than normal for similar experiments due to problems with beam tuning.

5.3.2 Theoretical Cross Section Errors

Theoretical DWBA calculations of differential cross section angular distributions from the WSAW/FOLD/DWHI code package were used in two different aspects of the data analysis. They were used in the multipole decomposition analysis described in Section 4.3.1 to provide line shapes for the MDA fit procedure. They were also used to perform an extrapolation from the experimental cross section with a finite Q-value to a cross section with $Q = 0$ using Equation 4.3.3 that was discussed in Section 4.3.2. This extrapolation was necessary to fulfill the condition of zero linear momentum transfer ($q = 0$) required to calculate Gamow-Teller strengths with Equation 4.3.1. The only difference between these two theory calculations was the input Q-value, so the potential sources of error within the calculations themselves were essentially identical. Thus, treatment of the error associated with these two different calculated quantities varied only slightly.

When used in the MDA fit procedure, the magnitudes of angular distributions were treated as fitted parameters. This means that errors of absolute magnitude in the DWBA were not very relevant; variations in the line shapes of the angular distributions were much more important. This insensitivity to absolute magnitudes means that errors in the DWBA calculations were considered negligible in comparison to other sources of experimental error. Error resulting from line-shape choices in the MDA procedure was much more critical, and this is discussed in more detail in the next section (Section 5.3.3).

In the extrapolation to zero linear momentum transfer ($q = 0$) from Equation 4.3.3, the two different calculated angular distribution values for $Q = Q_{exp}$ and $Q = 0$ at $\theta = 0^\circ$ were divided by each other to form a ratio. Since only the ratio of the two values matters, neither absolute magnitudes nor line shapes were relevant; as a result, this quantity was very

insensitive to errors in the DWBA calculation. In the final error calculation, any error in this quantity was considered to be negligible.

The WSAW/FOLD/DWHI code package itself has been vetted by comparing its calculation results to numerous data sets. Any errors from uncertainties in the code are expected to be negligible compared to other sources of experimental error. Similarly, the error associated with the various code inputs was treated as negligible, but these inputs are listed for completeness.

WSAW inputs:

- Binding energies calculated in OXBASH
- A single-particle potential: Diffuseness, Coulomb radius, Woods-Saxon radius, and Spin-orbit potential depth
- Quantum numbers: spin, total angular momentum, orbital angular momentum, and charge

FOLD inputs:

- Kinetic energy of the beam particles
- Quantum numbers: total angular momentum, parity, isospin, isospin projection
- Effective nucleon-nucleon interaction (Love-Franey interaction)
- One-body transition densities from OXBASH calculations

DWHI inputs:

- Quantum numbers: total angular momentum, charge

- Kinetic energy of the beam particles
- Optical potential parameters
- Coulomb radii
- Q-value

5.3.3 Gamow-Teller Strength Errors

Gamow-Teller strength was calculated with Equation 4.3.1 as discussed in Section 4.3. This required fitting the theoretical angular distributions to experimentally determined differential cross sections in a multipole decomposition analysis, as discussed in Section 4.3.1. Four different factors contributed to the error of the Gamow-Teller strength measurements. Statistical error arose from the number of events counted in the course of the experiment. Systematic errors came from the multipole decomposition analysis (MDA) procedure that was discussed in Section 4.3.1. More systematic errors (not related to the MDA) arose from the conversion of experimental event counts into an absolute cross section. The tensor term of the effective interaction also contributed a small systematic error.

5.3.3.1 Statistical Error

The statistical error was derived from the number of counts (N) measured during the experiment. These counts were separated into bins by scattering angle (θ) and excitation energy in ^{19}O (E_x [^{19}O]). The relative statistical error for each of these bins was found with the formula $\frac{\sqrt{N}}{N}$, where $\sqrt{N}$ was the error of a bin with N counts in it. For the first excited state at 0.096 MeV in ^{19}O, this error was 7.9%. For the second excited state at 1.471 MeV

in ^{19}O, this error was 13.6%. The statistical errors of the measurements for $E_x\left[^{19}\mathrm{O}\right] > 3.5$ MeV varied greatly and were generally large.

In Gamow-Teller strength calculations with $E_x\left[^{19}\mathrm{O}\right] > 8.0$ MeV, the carbon background subtraction procedure that was described in Section 4.2.3 increased the statistical error. This was handled through error propagation formulas derived from Equation 4.2.4. The higher statistical error from carbon background subtraction contributed significantly to the larger final errors in computed Gamow-Teller strengths in this region.

This statistical error was incorporated into the calculation of Gamow-Teller strength through the multipole decomposition analysis fit. The fit parameters had a calculated error, which came from the statistical error for each point in the fit (shown with error bars in Figure 4.11 and Figure 4.14).

5.3.3.2 Systematic Error in the Multipole Decomposition Analysis

In order to account for the error in the MDA procedure due to line shape choices that was mentioned in Section 5.3.2, many different line shapes from sets of angular distributions were tested. The best-fitting set of line shapes was used to calculate Gamow-Teller strengths. However, to account for the error in this procedure, all sets of angular distributions with at least a 5% chance of being accurate according to a chi-squared goodness of fit test were considered valid. From this expanded set of valid fits, the two fits that provided the highest and lowest Gamow-Teller strengths were used to establish the systematic error bounds due to the MDA procedure.

For the two low-lying states at 0.096 MeV and 1.471 MeV in the excitation energy of ^{19}O, the error from the MDA process was negligible. At these energies, the level density is still very low, so there are very few possible choices of line shapes for the multipole decomposition

analysis; additionally, the line shape options that are present do not vary much from each other. The state at 0.096 MeV is well-separated from all but the ground state of ^{19}O. Fortunately, this ground state contribution was expected to have only a $\Delta L = 2$ component, which did not strongly alter the $\Delta L = 0$ component that determined the Gamow-Teller strength. The state at 1.471 MeV is well-separated from all other states in ^{19}O.

At higher energies, the systematic error from the multipole decomposition analysis became much more important. This systematic error was large enough that no Gamow-Teller strength could be conclusively detected for $E_x[^{19}\mathrm{O}] > 3.5$ MeV. Individual states could not be isolated in the data set at these energies due to relatively low energy resolution and to lack of statistics. Additionally, many of the known states in ^{19}O with $E_x[^{19}\mathrm{O}] > 3.5$ MeV do not have firm total angular momentum or parity assignments. Some known states do not match up well with shell-model level predictions from OXBASH calculations. All of these factors increased the uncertainty associated with the MDA fits due to line shape choices. The errors from the MDA procedure are listed for each measured Gamow-Teller strength in Table 5.4. The contribution of the MDA error to the final error of a Gamow-Teller strength measurement varied considerably, but averaged 80% and ranged from 30% to 100% for measurements with $E_x[^{19}\mathrm{O}] > 3.5$ MeV. It was the dominant error factor for all but one of these measurements (the one exception had extremely high statistical error).

5.3.3.3 Systematic Error in the B[GT] Calculation

Several potential systematic errors (not related to the MDA) arose from the conversion of experimental event counts into an absolute cross section. Three of these errors were large enough to be included in the error analysis calculation. The rest were considered to be negligible. These systematic errors come from the portion of the data analysis that is

E_x (^{19}O) (MeV)	B[GT]	MDA Error (+)	MDA Error (-)
0.096	0.068	N/A	N/A
1.471	0.057	N/A	N/A
3.5–4.0	0	0.018	0
4.0–4.5	0	0.013	0
4.5–5.0	0	0.038	0
5.0–5.5	0	0.052	0
5.5–6.0	0.022	0.029	0.022
6.0–6.5	0.011	0.026	0.011
6.5–7.0	0.049	0.020	0.049
7.0–7.5	0	0.027	0
7.5–8.0	0.037	0.024	0.037
8.0–8.5	0.111	0.070	0.111
8.5–9.0	0.146	0.051	0.146
9.0–9.5	0.046	0.042	0.011
9.5-10.0	0.068	0.025	0.068
10.0–10.5	0.085	0.036	0.085
10.5–11.0	0.041	0.031	0.041
11.0–11.5	0.011	0.042	0.011
11.5–12.0	0	0.070	0
12.0-12.5	0.096	0.065	0.096
12.5–13.0	0.037	0.090	0.037
13.0–13.5	0	0.151	0
13.5–14.0	0.099	0.072	0.099
14.0–14.5	0	0.156	0
14.5–15.0	0.007	0.009	0.002
15.0–15.5	0	0.169	0
15.5–16.0	0	0.149	0

Table 5.4: This table lists the calculated Gamow-Teller strengths for the ^{19}F(t,^{3}He)^{19}O* reaction at 115 MeV along with the errors due only to the multipole decomposition analysis (MDA). These errors from the MDA procedure dominated the total errors for Gamow-Teller strengths above 3.5 MeV in ^{19}O. On average, they accounted for 80% of the total error for a measurement, ranging from a minimum of 30% to a maximum of 100%.

described in Section 4.2.

The solid angle angle calculation ($d\Omega$) in Equation 4.2.1 of Section 4.2.1 had no significant error, as it was a straightforward geometrical calculation. There was an error associated with the calculation of the acceptance correction ($P_{acceptance}$) via a Monte Carlo simulation. However, the error in this Monte Carlo simulation can be reduced by simulating a large number of events, so 1 billion events were simulated. This reduced the expected errors for the simulation to a point where they were negligible compared to other sources of error. Any uncertainties in the simulation code itself were determined to be negligible compared to statistical uncertainties by examining the calibration data taken on a CH_2 target to validate the data analysis procedure, as was discussed in Section 5.3.1. The cross section that was produced for the $^{12}C(t,^3He)^{12}B^*$ reaction using the Monte Carlo acceptance correction was compared to a prior measurement of this same reaction in experiment 06032 (see Section 4.2.2) and the results were in good agreement. This indicated that any uncertainties in the data analysis procedure up to the relative cross section calculation must be minor.

The conversion from a relative cross section to an absolute cross section involved four scaling factors (ϵ_{abs}, ϵ_1, ϵ_2, and ϵ_3) that were discussed in detail in Section 4.2.2. The scaling factor of $\epsilon_{\text{abs}} = 0.048$ mb was determined by a fit between the $^{12}C(t,^3He)^{12}B_{g.s.}$ reaction cross section that was measured in the current experiment and a prior measurement during experiment 06032 (see Figure 4.9). The error in this factor (± 0.001 mb, 2.2%) was determined from the error in the fit. This error in ϵ_{abs} was treated as a systematic error.

The scaling factor for beam rate ratios ($\epsilon_1 = 0.35$) was determined by taking the average of the beam rate measurements from three different detectors (see Section 4.2.2); the error in this term (± 0.03, 8.8%) was determined by taking twice the standard deviation of this average. This very conservative error was chosen (instead of a single standard deviation)

because these beam rate measurements were all indirect measurements and there was no direct comparison to the actual beam rate available; it was treated as a systematic error.

The scaling factor for differences in data acquisition live time ($\epsilon_2 = 0.9634$) was considered to have negligible error; this decision was based past experience with the same data acquisition system in similar experiments.

The scaling factor for target composition differences ($\epsilon_3 = 3.183$) was also considered to have negligible error. The calculation of the scaling factor ϵ_3 involves two different sources of potential error: the molar mass of the chemical compounds in the targets and the thickness of the targets. The masses of all the isotopes present in the target were known to a high precision, so this part of the error was negligible. The target thickness was not trivial to measure accurately, but could be considered negligible for this experiment because the beam spot was large. The large beam spot sampled the target thickness across a large area, so any variations in thickness over a small area were deemed irrelevant.

To calculate a Gamow-Teller strength using Equation 4.3.1, the experimental cross sections must first be projected to $Q = 0$ to fulfill the requirement of zero linear momentum transfer ($q = 0$), as discussed in Section 4.3.2. This was accomplished with the ratio $\left[\frac{\frac{d\sigma}{d\Omega}(Q=0,0^\circ)}{\frac{d\sigma}{d\Omega}(Q_{exp},0^\circ)}\right]_{theory}$ from Equation 4.3.3. As discussed previously in Section 5.3.2, this ratio was computed from theoretical angular distributions that were calculated with the WSAW/FOLD/DWHI code package. Thus, any errors in this ratio were considered negligible compared to experimental errors.

In the proportionality relationship described by Equation 4.3.1, there was a significant error associated with obtaining the unit cross section ($\hat{\sigma}_{\mathrm{GT}}$) from the phenomenological global fit of Equation 4.3.4. The error associated with this unit cross section was 5%; the fit and its error are discussed in Reference [38]. This error was treated as a systematic error.

5.3.3.4 Systematic Error from the Tensor Interaction

As mentioned briefly at the end of Section 4.3.1, the tensor interaction causes systematic errors in Gamow-Teller strength measurements. Interference between the transition amplitudes due to the $\sigma\tau$ and Tτ (tensor-τ) components of the effective interaction creates a systematic error that cannot be accounted for with an MDA procedure. The error due to the tensor component of the interaction is stronger for weak Gamow-Teller states because of this interference dynamic (see Reference [42] for details). This systematic error was estimated by calculating theoretical angular distributions for a transition twice: once with the full interaction (including the tensor interaction term), and once without the tensor interaction. The difference between these two results provided an estimate for the systematic error. The procedure for examining error from the tensor interaction is outlined fully in Reference [42], which discusses error from the tensor interaction in Gamow-Teller strength measurements in greater detail. The error due to the tensor term was found to be +0.0026 for the first excited state at 0.096 MeV in ^{19}O (an error of 4%) and +0.0011 for the second excited state at 1.471 MeV in ^{19}O (an error of 2%). In both cases, this error happened to cause an underestimation of the Gamow-Teller strength, so it is applied only to the positive error value; more generally, this error could be positive or negative.

Error from the tensor term in the effective interaction was ignored for the higher-lying strength. Error from the MDA procedure dominated these measurements, as was discussed earlier. Since it was not possible to definitively identify any Gamow-Teller strength above the 1.471 MeV state of ^{19}O in this data analysis, any additional error from the tensor interaction was negligible compared to the MDA error contributions. If Gamow-Teller strengths could be definitively established in a future experiment, then it would be necessary to examine the

tensor contributions to the errors.

5.3.3.5 Summary of Errors Related to Gamow-Teller Strengths

In summary, there were four types of error considered in the calculation of Gamow-Teller strengths. These four error categories were: statistical error, systematic MDA error, systematic (non-MDA) errors, and tensor interaction systematic error. For the first two excited states at 0.096 MeV and 1.471 MeV in ^{19}O, statistical errors were the dominant source of error, followed by systematic (non-MDA) errors and then by tensor interaction systematic error, with systematic MDA error considered negligible. In the higher-lying Gamow-Teller strength measurements with $E_x[^{19}\mathrm{O}] > 3.5$ MeV, the total error was dominated by systematic MDA error, followed by statistical error, followed by systematic (non-MDA) errors; tensor interaction systematic errors were considered negligible.

The transition from the ground state of ^{19}F to the first excited state of ^{19}O at 0.096 MeV was found to have a Gamow-Teller strength of B[GT] $= 0.068^{+0.011}_{-0.009}$, which corresponded to relative errors of $^{+16\%}_{-11\%}$. The transition from the ground state of ^{19}F to the second excited state of ^{19}O at 1.471 MeV was found to have a Gamow-Teller strength of B[GT] $= 0.057^{+0.011}_{-0.010}$, which corresponded to relative errors of $^{+19\%}_{-18\%}$.

5.3.4 β-decay Rate Errors

Calculation of the β-decay rate for the first excited state at 0.096 MeV in ^{19}O was a multi-step process with several possible sources of error. Ultimately, only one factor added significant error to the decay rate, beyond the error in the computed Gamow-Teller strength that was discussed in detail in Section 5.3.3. This important factor was the choice of theoretical Gamow-Teller strengths and an associated error for the determination of branching ratios (Equation 5.1.5). Other possible but negligible sources of error are discussed in this section for completeness.

Equation 5.1.2 converted Gamow-Teller strengths (B[GT]) into ft-values. Equations 5.1.3 and 5.1.4 converted the ft-values into partial decay rates (λ_i). Beyond the error of the experimentally determined Gamow-Teller strength, possible sources of error included the factors $\frac{K}{g_v^2}$ and $\frac{g_a}{g_v}$ in Equation 5.1.2; these had relative errors of 0.2% and 0.03% respectively, which were both negligible compared to the error in B[GT]. The $\log(f)$ values determined from Reference [76] had a relative error of 0.01%, which was also negligible.

Equation 5.1.5 determined branching ratios for the β-decay from the 0.096 MeV state in ^{19}O to five possible states in ^{19}F. These branching ratio (I_i) calculations used the experimentally determined Gamow-Teller strength to find the partial decay rate to the ground state of ^{19}F and theoretical Gamow-Teller strengths to find the partial decay rates to four

excited states of ^{19}F (see Table 5.2). Then the final β-decay rate (λ_x) for the first excited state at 0.096 MeV in ^{19}O was calculated with Equation 5.1.7. To perform this calculation of the branching ratios, theoretical Gamow-Teller strengths and associated errors were chosen for transitions from the 0.096 MeV excited state in ^{19}O to four excited states in ^{19}F. The theoretical Gamow-Teller strengths were calculated with the USDB interaction [72] using OXBASH [50]. The final calculation of λ_x was not sensitive to the choice of interaction; Gamow-Teller strengths computed using the WBP interaction [54] gave the same result. The USDB interaction was chosen over the WBP interaction because it is generally a better choice for *sd*-shell nuclei, and thus likely to be of interest to a wider audience, even though it did not outperform the WBP interaction for the transition measured in this experiment. A relative error of 36% was assigned to the theoretical Gamow-Teller strengths to reflect the error in the USDB's prediction of the Gamow-Teller strength for the experimentally measured transition from the 0.096 MeV excited state of ^{19}O to the ground state of ^{19}F. This was a somewhat arbitrary assignment of error, but it turns out that the calculation of λ_x was not very sensitive to this error assignment, though it is still significant. The reason for this can be seen in the branching ratios listed in Table 5.2. The measured transition accounted for the large majority (86%) of the branching ratio. Only one other transition (from the 0.096 MeV excited state of ^{19}O to the 1.554 MeV state of ^{19}F) had a significant branching ratio (12.5%), and thus a significant effect on the calculation of λ_x.

The population of the first excited state at 0.096 MeV in ^{19}O in a stellar temperature range was computed with Equation 5.1.8. Equation 5.1.9 determined the temperature dependence of the total β-decay rate for a stellar population of ^{19}O. The variables involved in computing the Boltzmann distribution for P_j were the spins and energy levels of the ground and first excited states, which were well-known, and the Boltzmann constant, which was also

well-known; thus, the Boltzmann distribution computation was not a significant source of error. The β-decay rate for the ground state of ^{19}O ($\lambda_{g.s.}$) was a potential source of error in Equation 5.1.9, but it had a negligible error of 0.3% [25].

The final value of the β-decay rate for the 0.096 MeV excited state of ^{19}O was found to be $\lambda_x = 0.038^{+0.011}_{-0.008}$ s^{-1}, which corresponded to a relative error of $^{+29\%}_{-21\%}$. This error was dominated by the error in the Gamow-Teller strength measurement for the transition from the 0.096 MeV first excited state of ^{19}O to the ground state of ^{19}F, but error from the determination of the branching ratio with theoretical Gamow-Teller strengths also influenced the final error significantly.

Chapter 6

Summary

6.1 Summary

This dissertation described the measurement of the charge-exchange reaction ^{19}F(t,^{3}He) at 115 MeV/nucleon. The experiment was performed at the Coupled Cyclotron Facility at the National Superconducting Cyclotron Laboratory (NSCL). A beam of tritons from the Coupled Cyclotron Facility was impinged on a target that contained fluorine (CF_2). The ^{3}He ejectiles were momentum-analyzed in the S800 spectrograph. An overview of the experimental apparatuses that were used in this measurement is available in Chapter 3 and Figure 3.1. A more detailed explanation of the S800 spectrograph in particular was given in Section 3.3.

This specific reaction was measured to test a hypothesis on fluorine nucleosynthesis in core-collapse supernovae. As discussed in Chapter 1, there are several different theories regarding where and how the element fluorine is produced. There is currently no consensus between these different theories of fluorine nucleosynthesis and available astrophysical observations. The β-decay of ^{19}O* in core-collapse supernova has been previously suggested [26] as a possible avenue for fluorine nucleosynthesis. In hot astrophysical environments (such as supernovae), it is possible to thermally populate low-lying excited states of ^{19}O, and the β-decay of these excited states would enhance the overall β-decay rate into ^{19}F.

At the high temperatures of a core-collapse supernova, a significant portion of ^{19}O will achieve equilibrium in the very low-lying first excited state at 0.096 MeV, making it possible to β-decay from this excited state in ^{19}O* to ^{19}F. As was discussed in Section 1.3, this is interesting because β-decay between the ground state of ^{19}O and the ground state of ^{19}F is forbidden. However, β-decay from the low-lying excited state in ^{19}O at 0.096 MeV excited state in ^{19}O to the ground state of ^{19}F is allowed (see Figure 1.2). This creates an opportunity for a significant increase in the β-decay rate for ^{19}O in a supernova compared to the β-decay rate that has been measured directly for the ^{19}O ground state in laboratory conditions. Chernykh *et al.* [26] performed a theoretical calculation to estimate the reaction rate increase that occurs when the 0.096 MeV state in ^{19}O is taken into account. Their calculations suggested that the β-decay rate for ^{19}O$(\beta^-)^{19}$F might increase by a factor of three at high stellar temperatures.

To examine this theory, the ^{19}F$(t,^3$He$)^{19}$O* reaction at 345 MeV was measured. The differential cross section of this charge-exchange reaction can be used to extract the Gamow-Teller strength distribution for ($\Delta L = 0$, $\Delta S = 1$) transitions between ^{19}F and ^{19}O using Equation 2.1.2, as discussed in Chapter 2. The procedure discussed in Section 2.1, when applied to data from the ^{19}F$(t,^3$He$)^{19}$O* reaction, allowed for the extraction of the Gamow-Teller strength of the beta decay from the 0.096 MeV state in ^{19}O to the ground state of ^{19}F. This particular Gamow-Teller strength was then used to calculate the same β^--decay rate for ^{19}O$(\beta^-)^{19}$F ($\lambda_{\rm tot}$) that was discussed in by Chernykh *et al.* in Reference [26].

The procedure for extracting differential cross sections from data taken with the S800 spectrograph was described in Sections 4.1 and 4.2. The differential cross sections were used to compute Gamow-Teller strengths in Section 4.3. For the transition from the ground state of ^{19}F to the 0.096 MeV state of ^{19}O, a Gamow-Teller strength of B[GT] $= 0.068^{+0.011}_{-0.009}$ was

found. This corresponds to B[GT] = $0.034^{+0.006}_{-0.004}$ for transitions in the ^{19}O $\rightarrow^{19}$ F direction (see also Figure 4.14 A). Gamow-Teller strengths for transitions from the ground state of ^{19}F for excitation energies in ^{19}O of 0 MeV to 16 MeV are listed in Table 4.11 and plotted in Figure 4.15.

The Gamow-Teller strength for the transition from the first excited state of ^{19}O at 0.096 MeV to the ground state of ^{19}F was used to calculate a weak decay rate in Section 5.1 to compare with the theoretical calculation of Chernykh *et al.* in Reference [26]. For the transition from the 0.096 MeV excited state alone, this β^--decay rate was found to be $\lambda_x = 0.038^{+0.011}_{-0.008}$ s^{-1} (which corresponds to $T_{1/2} = 18^{+5}_{-4}$ s). A total β^--decay rate over stellar temperatures (T) for ^{19}O in either the first excited or ground state was found with Equation 5.1.9 and plotted in Figure 5.2.

As discussed in Section 5.2 and shown in Figure 5.2, the increase in the total β-decay rate (λ_{tot}) over a range of astrophysical temperatures is modest. At the top of the temperature range, this new rate (λ_{tot}) increases 18% above the ground state reaction rate ($\lambda_{g.s.}$). This small rate increase is unlikely to have a significant influence on astrophysical simulations of fluorine production, but a full fluorine nucleosynthesis simulation would be needed to confirm that. This result contradicts the theoretical results put forth by Chernykh *et al.* in Reference [26]; the discrepancy might stem from a calculation error in Reference [26] in the Boltzmann distribution. A detailed discussion of the error analysis for all values calculated in this dissertation was provided in Section 5.3.

The new experimentally determined rate (λ_{tot}) presented in this work is available for future studies of fluorine nucleosynthesis that involve the ^{19}O(β^-)^{19}F reaction. Additionally, the Gamow-Teller strength distribution presented in Figure 4.15 provides boundaries to guide future studies of ^{19}F$_{g.s.}$ to ^{19}O* transitions and to constrain shell-model calculations.

6.2 Outlook

6.2.1 Fluorine Nucleosynthesis

As stated earlier, this new measurement of the β-decay rate of the first excited state of ^{19}O to the ground state of ^{19}F is not expected to significantly influence fluorine production in core-collapse supernovae. This cannot be definitively concluded until the new decay rate is tested in astrophysical simulations, but it is clear that any increase from such decays will be modest. However, as mentioned in Section 1.5, there has been little effort to simulate the fluorine production from ^{19}O$(\beta^-)^{19}$F at all in any astrophysical environment. This path of fluorine production has not received much attention because, as Jorissen *et al.* observed in Reference [8], production of ^{19}O via neutron capture on ^{18}O inevitably competes with the much stronger rate of neutron capture on ^{19}F. This leads to the assumption that neutron capture processes are a net loss for fluorine abundance.

While it is quite possible, even probable, that neutron capture processes are strictly a net loss for fluorine abundance, that hypothesis should be examined in detailed astrophysical simulations. Fluorine abundance predictions from simulations would provide stronger guidance as to whether the ^{19}O$(\beta^-)^{19}$F process is a viable alternative for fluorine production. Prior research into fluorine nucleosynthesis has shown that it is an unusual nucleosynthesis process which depends closely on the stellar dynamics that govern the ejection of matter from the star, so simple rate comparisons can be misleading. Simulated abundance predictions would give clearer guidance as to whether this nucleosynthesis path merits further research.

Further progress in understanding fluorine nucleosynthesis will rely heavily upon astrophysical observations and astrophysical simulations. Asymptotic giant branch (AGB) stars are currently the best understood sources of fluorine production. It is not yet clear if Wolf-

Rayet stars or core-collapse supernovae produce significant amounts of fluorine, so more study is needed for both of these stellar environments. A study of galactic fluorine with a chemical evolution model is needed to update the work of Renda *et al.* [20] with the progress made in the field of fluorine nucleosynthesis in the past decade.

Another opportunity for improvement in fluorine nucleosynthesis measurements lies in the study of our solar system's fluorine abundance. Currently, the only solar measurement of fluorine abundance available comes from a study of sunspot composition from a paper by Hall *et al.* published in 1969 [14], and it has a fairly large uncertainty: $A(\mathrm{F}) = 4.56 \pm 0.33$ dex (see also Section 1.2). It should be possible to take advantage of improvements in the understanding of solar physics from the past four decades to perform an improved version of Hall *et al.*'s sunspot study of HF molecules. Improvements in technology might allow for a modern study of solar fluorine abundances to be done with a UV-capable satellite telescope that could view elemental fluorine. It might be possible to improve upon the solar system fluorine abundance measured with carbonaceous chondrite meteorites [15], which has a higher accuracy of 15% that still leaves room for improvement.

6.2.2 Nuclear Structure

The experiment described in this dissertation did not allow for a detailed study of the nuclear structure of the $^{19}\mathrm{F}_{g.s.}$ to $^{19}\mathrm{O}^*$ transitions, but it did suggest a potential future experiment to that end. The state predicted by shell-model calculations to have the strongest Gamow-Teller strength (B[GT] $\approx$ 0.1) in the $^{19}\mathrm{F}(t,^3\mathrm{He})^{19}\mathrm{O}^*$ reaction occurs at approximately 7.5 MeV in the excitation energy of $^{19}\mathrm{O}$ (see Table 4.12). In the present experiment, that state happens to fall very close to the peak for the $^{12}\mathrm{C}(t,^3\mathrm{He})^{12}\mathrm{B}_{g.s.}$ transition at $E_x\left[^{19}\mathrm{O}\right] = 8.5$ MeV generated by the carbon nuclei in the CF_2 target. If another experi-

ment were performed with a different target choice, it would likely be possible to measure the Gamow-Teller strength and excitation energy of this strong state. Current results hint that a strong Gamow-Teller state might exist near $E_x\left[^{19}\mathrm{O}\right] = 8.5$ MeV (see Figure 4.15), but the high error precludes a firm measurement of B[GT]. An experiment with higher statistics might also allow for a quantitative measurement of the Gamow-Teller strength distribution for states with $E_x\left[^{19}\mathrm{O}\right] > 3.5$ MeV. Possible target options for such an experiment include fluorspar (CaF_2), a mineral, or hydrofluoric acid ($HF+(H_2O)_n$), a weak acid, among other fluorine compounds.

BIBLIOGRAPHY

BIBLIOGRAPHY

[1] Bernard E. J. Pagel. *Nucleosynthesis and Chemical Evolution of Galaxies*. Cambridge University Press, 1997. ISBN 0 521 55958 8.

[2] Christian Iliadis. *Nuclear Physics of Stars*. Wiley-VCH, 2007. ISBN 978-3-527-40602-9.

[3] E. Margaret Burbidge, G. R. Burbidge, William A. Fowler, and F. Hoyle. Synthesis of the elements in stars. *Reviews of Modern Physics*, 29(4):547–650, October 1957. http://dx.doi.org/10.1103/RevModPhys.29.547.

[4] S. E. Woosley and W. C. Haxton. Supernova neutrinos, neutral currents and the origin of fluorine. *Nature*, 334(6177):45–47, July 1988. http://www.nature.com/nature/journal/v334/n6177/index.html#LT.

[5] S. E. Woosley, A. Heger, and T. A. Weaver. The evolution and explosion of massive stars. *Reviews of Modern Physics*, 74(4):1015–1071, October 2002. http://link.aps.org/doi/10.1103/RevModPhys.74.1015.

[6] A. Heger, E. Kolbe, W. C. Haxton, K. Langanke, G. Martínez-Pinedo, and S. E. Woosley. Neutrino nucleosynthesis. *Physics Letters B*, 606(3–4):258–264, January 2005. http://www.sciencedirect.com/science/article/pii/S0370269304016739.

[7] Martin Asplund, Nicolas Grevesse, A. Jacques Sauval, and Pat Scott. The Chemical Composition of the Sun. *Annual Review of Astronomy and Astrophysics*, 47:481–522, September 2009. http://dx.doi.org/10.1146/annurev.astro.46.060407.145222.

[8] A. Jorissen, V. V. Smith, and D. L. Lambert. Fluorine in red giant stars: evidence for nucleosynthesis. *Astronomy and Astrophysics*, 261(1):164–187, July 1992. http://adsabs.harvard.edu/abs/1992A%26A...261..164J.

[9] C. Abia, A. Recio-Blanco, P. de Laverny, S. Cristallo, I. Domínguez, and O. Straniero. Fluorine in Asymptotic Giant Branch Carbon Stars Revisited. *The Astrophysical Journal*, 694(2):971–977, April 2009. http://stacks.iop.org/0004-637X/694/i=2/a=971.

[10] X.-W. Liu. Temperature fluctuations and chemical homogeneity in the planetary nebula NGC 4361. *Monthly Notices of the Royal Astronomical Society*, 295(3):699–710, April 1998. http://adsabs.harvard.edu/abs/1998MNRAS.295..699L.

[11] Y. Zhang and X.-W. Liu. Fluorine Abundances in Planetary Nebulae. *The Astrophysical Journal Letters*, 631(1):L61–L64, September 2005. http://stacks.iop.org/1538-4357/631/i=1/a=L61.

[12] K. Werner, T. Rauch, and J. W. Kruk. Fluorine in extremely hot post-AGB stars: Evidence for nucleosynthesis. *Astronomy & Astrophysics*, 433(2):641–645, April 2005. http://dx.doi.org/10.1051/0004-6361:20042258.

[13] Gajendra Pandey. The Discovery of Fluorine in Cool Extreme Helium Stars. *The Astrophysical Journal Letters*, 648(2):L143–L146, August 2006. http://stacks.iop.org/1538-4357/648/i=2/a=L143.

[14] Donald N. B. Hall and Robert W. Noyes. Observation of Hydrogen Fluoride in Sunspots and the Determination of the Solar Fluorine Abundance. *Astrophysical Letters*, 4(5):143–148, November 1969.

[15] Katharina Lodders. Solar System Abundances and Condensation Temperatures of the Elements. *The Astrophysical Journal*, 591(2):1220–1247, July 2003. http://stacks.iop.org/0004-637X/591/i=2/a=1220.

[16] E. Anders and M. Ebihara. Solar-system abundances of the elements. *Geochimica et Cosmochimica Acta*, 46(11):2363, November 1982. http://dx.doi.org/10.1016/0016-7037(82)90208-3.

[17] European Southern Observatory website. http://www.eso.org.

[18] S. E. Woosley, D. H. Hartmann, R. D. Hoffman, and W. C. Haxton. The ν-process. *The Astrophysical Journal*, 356:272–301, June 1990. http://adsabs.harvard.edu/abs/1990ApJ...356..272W.

[19] S. E. Woosley and Thomas A. Weaver. The Evolution and Explosion of Massive Stars. II. Explosive Hydrodynamics and Nucleosynthesis. *The Astrophysical Journal Supplement Series*, 101(1):181–235, November 1995. http://adsabs.harvard.edu/abs/1995ApJS..101..181W.

[20] Agostino Renda, Yeshe Fenner, Brad K. Gibson, Amanda I. Karakas, John C. Lattanzio, Simon Campbell, Alessandro Chieffi, Katia Cunha, and Verne V. Smith. On the origin of fluorine in the Milky Way. *Monthly Notices of the Royal Astronomical Society*, 354(2):575–580, October 2004. http://dx.doi.org/10.1111/j.1365-2966.2004.08215.x.

[21] Katia Cunha, Verne V. Smith, David L. Lambert, and Kenneth H. Hinkle. Fluorine Abundances in the Large Magellanic Cloud and ω Centauri: Evidence for Neutrino Nucleosynthesis? *The Astronomical Journal*, 126(3):1305–1311, September 2003. http://stacks.iop.org/1538-3881/126/i=3/a=1305.

[22] Katia Cunha, Verne V. Smith, and Brad K. Gibson. Fluorine Abundances in the Milky Way Bulge. *The Astrophysical Journal Letters*, 679(1):L17–L20, April 2008. http://stacks.iop.org/1538-4357/679/i=1/a=L17.

[23] B. D. Anderson, N. Tamimi, A. R. Baldwin, M. Elaasar, R. Madey, D. M. Manley, M. Mostajabodda'vati, J. W. Watson, W. M. Zhang, and C. C. Foster. Gamow-Teller strength in the (p, n) reaction at 136 MeV on ^{20}Ne, ^{24}Mg, and ^{28}Si. *Physical Review C*, 43(1):50–58, January 1991. http://dx.doi.org/10.1103/PhysRevC.43.50.

[24] S. R. Federman, Yaron Sheffer, David L. Lambert, and V. V. Smith. *Far Ultraviolet Spectroscopic Explorer* Measurements of Interstellar Fluorine. *The Astrophysical Journal*, 619(2):884–890, February 2005. http://stacks.iop.org/0004-637X/619/i=2/a=884.

[25] D. R. Tilley, H. R. Weller, C. M. Cheves, and R. M. Chasteler. Energy levels of light nuclei $A = 18$–19. *Nuclear Physics A*, 595(1):1–170, December 1995. http://dx.doi.org/10.1016/0375-9474(95)00338-1.

[26] M. Chernykh, J. Enders, P. von Neumann-Cosel, C. Rangacharyulu, and A. Richter. The Role of the 96 keV Level in the ^{19}O$(\beta^-)^{19}$F Process at Stellar Temperatures. *The Astrophysical Journal Letters*, 633(1):L61–L64, November 2005. http://stacks.iop.org/1538-4357/633/i=1/a=L61.

[27] G. Meynet and M. Arnould. Synthesis of ^{19}F in Wolf-Rayet stars. *Astronomy & Astrophysics*, 355(1):176–180, March 2000. http://aa.springer.de/bibs/0355001/2300176/small.htm.

[28] Paul A. Crowther. Physical Properties of Wolf-Rayet Stars. *Annual Review of Astronomy and Astrophysics*, 45:177–219, September 2007. http://dx.doi.org/10.1146/annurev.astro.45.051806.110615.

[29] A. Palacios, M. Arnould, and G. Meynet. The thermonuclear production of ^{19}F by Wolf-Rayet stars revisited. *Astronomy & Astrophysics*, 443(1):243–250, November 2005. http://dx.doi.org/10.1051/0004-6361:20053323.

[30] Claudio Ugalde. *The $^{19}F(\alpha, p)^{22}Ne$ Reaction and the Nucleosynthesis of Fluorine*. Ph.D. dissertation, University of Notre Dame, Notre Dame, IN 46556, July 2005. http://physics.nd.edu/assets/25579/ugaldec072005.pdf.

[31] A. I. Karakas, M. A. Lugaro, M. Wiescher, J. Görres, and C. Ugalde. The Uncertainties in the ^{22}Ne+α-Capture Reaction Rates and the Production of the Heavy Magnesium Isotopes in Asymptotic Giant Branch Stars of Intermediate Mass. *The Astrophysical Journal*, 643(1):471–483, May 2006. http://stacks.iop.org/0004-637X/643/i=1/a=471.

[32] C. Abia, K. Cunha, S. Cristallo, P. de Laverny, I. Domínguez, K. Eriksson, L. Gialanella, K. Hinkle, G. Imbriani, A. Recio-Blanco, V. V. Smith, O. Straniero, and R. Wahlin. Fluorine Abundances in Galactic Asymptotic Giant Branch Stars. *The Astrophysical Journal Letters*, 715(2):L94–L98, June 2010. http://stacks.iop.org/2041-8205/715/i=2/a=L94.

[33] S. Goriely and N. Mowlavi. Neutron-capture nucleosynthesis in AGB stars. *Astronomy & Astrophysics*, 362(2):599–614, October 2000. http://aa.springer.de/bibs/0362002/2300599/small.htm.

[34] Ethan Uberseder, Michael Heil, Franz Käppeler, Joachim Görres, and Michael Wiescher. New measurements of the ^{19}F$(n,\gamma)^{20}$F cross section and their implications for the stellar reaction rate. *Physical Review C*, 75(3):035801, March 2007. http://prc.aps.org/abstract/PRC/v75/i3/e035801.

[35] T. N. Taddeucci, C. A. Goulding, T. A. Carey, R. C. Byrd, C. D. Goodman, C. Gaarde, J. Larsen, D. Horen, J Rapaport, and E. Sugarbaker. The (p,n) reaction as a probe of beta decay strength. *Nuclear Physics A*, 469(1):125–172, July 1987. http://dx.doi.org/10.1016/0375-9474(87)90089-3.

[36] H. Lenske, H. H. Wolter, and H. G. Bohlen. Reaction mechanism of heavy-ion charge-exchange scattering at intermediate energies. *Physical Review Letters*, 62(13):1457–1460, March 19899. http://dx.doi.org/10.1103/PhysRevLett.62.1457.

[37] W. G. Love and M. A. Franey. Effective nucleon-nucleon interaction for scattering at intermediate energies. *Physical Review C*, 24(3):1073–1094, September 1981. http://dx.doi.org/10.1103/PhysRevC.24.1073.

[38] R. G. T. Zegers, T. Adachi, H. Akimune, Sam M. Austin, A. M. van den Berg, B. A. Brown, Y. Fujita, M. Fujiwara, S. Galès, C. J. Guess, M. N. Harakeh, H. Hashimoto, K. Hatanaka, R. Hayami, G. W. Hitt, M. E. Howard, M. Itoh, T. Kawabata, K. Kawase, M. Kinoshita, M. Matsubara, K. Nakanishi, S. Nakayama, S. Okumura, T. Ohta, Y. Sakemi, Y. Shimbara, Y. Shimizu, C. Scholl, C. Simenel, Y. Tameshige, A. Tamii, M. Uchida, T. Yamagata, and M. Yosoi. Extraction of Weak Transition Strengths via the $(^3\mathrm{He},t)$ reaction at 420 MeV. *Physical Review Letters*, 99:202501, November 2007. http://dx.doi.org/10.1103/PhysRevLett.99.202501.

[39] G. Perdikakis, R. G. T. Zegers, Sam M. Austin, D. Bazin, C. Caesar, J. M. Deaven, A. Gade, D. Galaviz, G. F. Grinyer, C. J. Guess, C. Herlitzius, G. W. Hitt, M. E. Howard, R. Meharchand, S. Noji, H. Sakai, Y. Shimbara, E. E. Smith, and C. Tur. Gamow-Teller unit cross sections for the $(t,{}^3\mathrm{He})$ and $({}^3\mathrm{He},t)$ reactions. *Physical Review C*, 83:054614, May 2011. http://dx.doi.org/10.1103/PhysRevC.83.054614.

[40] Rhiannon Meharchand. *Spectroscopy of ^{12}Be using the (^7Li,^7Be) Reaction in Inverse Kinematics*. PhD thesis, Michigan State University, 2011. http://www.nscl.msu.edu/ourlab/publications/download/Meharchand2011_286.pdf.

[41] R. Meharchand, R. G. T. Zegers, B. A. Brown, Sam M. Austin, T. Baugher, D. Bazin, J. Deaven, A. Gade, G. F. Grinyer, C. J. Guess, M. E. Howard, H. Iwasaki, S. McDaniel, K. Meierbachtol, G. Perdikakis, J. Pereira, A. M. Prinke, A. Ratkiewicz, A. Signoracci, S. Stroberg, L. Valdez, P. Voss, K. A. Walsh, D. Weisshaar, and R. Winkler. Probing Configuration Mixing in ^{12}Be with Gamow-Teller Transition Strengths. *Physical Review Letters*, 108:122501, March 2012. http://dx.doi.org/10.1103/PhysRevLett.108.122501.

[42] R. G. T. Zegers, H. Akimune, Sam M. Austin, D. Bazin, A. M. van den Berg, G. P. A. Berg, B. A. Brown, J. Brown, A. L. Cole, I. Daito, Y. Fujita, M. Fujiwara, S. Galès, M. N. Harakeh, H. Hashimoto, R. Hayami, G. W. Hitt, M. E. Howard, M. Itoh, J. Jänecke, T. Kawabata, K. Kawase, M. Kinoshita, T. Nakamura, K. Nakanishi, S. Nakayama, S. Okumura, W. A. Richter, D. A. Roberts, B. M. Sherrill, Y. Shimbara, M. Steiner, M. Uchida, H. Ueno, T. Yamagata, and M. Yosoi. The $(t,{}^3\mathrm{He})$ and $({}^3\mathrm{He},t)$ reactions as probes of Gamow-Teller strength. *Physical Review C*, 74(2):024309, August 2006. http://dx.doi.org/10.1103/PhysRevC.74.024309.

[43] G. W. Hitt, R. G. T. Zegers, Sam M. Austin, D. Bazin, A. Gade, D. Galaviz, C. J. Guess, M. Horoi, M. E. Howard, W. D. M. Rae, Y. Shimbara, E. E. Smith, and C. Tur. Gamow-Teller transitions to ^{64}Cu measured with the $^{64}\mathrm{Zn}(t,{}^3\mathrm{He})$ reaction. *Physical Review C*, 80(1):014313, July 2009. http://dx.doi.org/10.1103/PhysRevC.80.014313.

[44] J. Cook and J. A. Carr, computer program FOLD, Florida State University (unpublished), based on F. Petrovich and D. Stanley, Nucl. Phys. A275, 487 (1977), modified as described in J. Cook *et al.*, Phys. Rev. C 30, 1538 (1984) and R. G. T. Zegers, S. Fracasso and G. Colò (2006), unpublished.

[45] Ian J. Thompson and Filomena M. Nunes. *Nuclear Reactions for Astrophysics: Principals, Calculation and Applications of Low-Energy Reactions*. Cambridge University Press, New York, 2009. www.cambridge.org/9780521856355.

[46] M. N. Harakeh and A. van der Woude. *Giant Resonances: Fundamental High-Frequency Modes of Nuclear Excitation*. Oxford University Press Inc., New York, 2001.

[47] George Wesley Hitt. *The $^{64}Zn(t,^3He)$ Charge-Exchange Reaction at 115 MeV Per Nucleon and Application to ^{64}Zn Stellar Electron-Capture*. PhD thesis, Michigan State University, 2009. http://www.nscl.msu.edu/ourlab/publications/download/Hitt2008_252.pdf.

[48] Carol Jeanne Guess. *The $^{150}Sm(t,^3He)^{150}Pm*$ and $^{150}Nd(^3He,t)^{150}Pm*$ Reactions and Applications for 2ν and 0ν Double Beta Decay*. PhD thesis, Michigan State University, 2011. http://www.nscl.msu.edu/ourlab/publications/download/Guess2010_272.pdf.

[49] R. G. T. Zegers. *Search for isovector giant monopole resonances*. PhD thesis, University of Groningen, 1999.

[50] B. A. Brown, A. Etchegoyen, N. S. Godwin, W. D. M. Rae, W. A. Richter, W. E. Ormand, E. K. Warburton, J. S. Winfield, L. Zhao, and C. H. Zimmerman. MSU-NSCL report number 1289.

[51] B. Alex Brown. New Skyrme interaction for normal and exotic nuclei. *Physical Review C*, 58(1):220–231, July 1998. http://dx.doi.org/10.1103/PhysRevC.58.220.

[52] S. C. Pieper and R. B. Wiringa. Quantum Monte Carlo calculations of light nuclei. *Annual Review of Nuclear and Particle Science*, 51:53–90, December 2001. http://dx.doi.org/10.1146/annurev.nucl.51.101701.132506.

[53] M. A. Franey and W. G. Love. Nucleon-nucleon t-matrix interaction for scattering at intermediate energies. *Physical Review C*, 31(2):488–498, February 1985. http://dx.doi.org/10.1103/PhysRevC.31.488.

[54] E. K. Warburton and B. A. Brown. Effective interactions for the $0p1s0d$ nuclear shell-model space. *Physical Review C*, 46(3):923–944, September 1992. http://dx.doi.org/10.1103/PhysRevC.46.923.

[55] H. Fujita, G. P. A. Berg, Y. Fujita, J. Rapaport, T. Adachi, N. T. Botha, H. Fujimura, K. Fujita, K. Hara, K. Hatanaka, J. Kamiya, T. Kawabata, K. Nakanishi, R. Neveling, N. Sakamoto, Y. Sakemi, Y. Shimbara, Y. Shimizu, F. D. Smit, M. Uchida, T. Wakasa, M. Yoshifuku, M. Yosoi, and R. G. T. Zegers. High resolution study of isovector negative parity states in the $^{16}O(^3He,t)^{16}F$ reaction at 140 MeV/nucleon. *Physical Review C*, 79:024314, February 2009. http://dx.doi.org/10.1103/PhysRevC.79.024314.

[56] S. Y. van der Werf, S. Brandenburg, P. Grasdijk, W. A. Sterrenburg, M. N. Harakeh, M. B. Greenfield, B. A. Brown, and M. Fujiwara. The Effective ^{3}He-Nucleon Force in a Microscopic DWBA Approach to the $(^3He,t)$

Charge-Exchange Reaction. *Nuclear Physics A*, 496(2):305–332, May 1989. http://dx.doi.org/10.1016/0375-9474(89)90177-2.

[57] C. N. Pinder, C. O. Blyth, N. M. Clarke, D. Barker, J. B. A. England, B. R. Fulton, O. Karban, M. C. Mannion, J. M. Nelson, C. A. Ogilvie, L. Zybert, R. Zybert, K. I. Pearce, P. J. Simmonds, and D. L. Watson. Consistent description of the $(t,^3\mathrm{He})$ reaction for $A = 12$–89. *Nuclear Physics A*, 533(1):25–48, October 1991. http://dx.doi.org/10.1016/0375-9474(91)90818-Q.

[58] D. J. Morrissey. The coupled cyclotron project at the NSCL. *Nuclear Physics A*, 616(1–2):45c–55c, 1997. http://dx.doi.org/10.1016/S0375-9474(97)00073-0.

[59] F. Marti, P. Miller, D. Poe, M. Steiner, J. Stetson, and X. Y. Wu. Commissioning of the Coupled Cyclotron system at NSCL. Number 600 in AIP Conference Proceedings, pages 64–68. American Institute of Physics, May 2001. http://dx.doi.org/10.1063/1.1435199.

[60] G. W. Hitt, Sam M. Austin, D. Bazin, A. L. Cole, J. Dietrich, A. Gade, M. E. Howard, S. D. Reitzner, B. M. Sherrill, C. Simenel, E. E. Smith, J. Stetson, A. Stolz, and R. G. T. Zegers. Development of a secondary triton beam from primary ^{16,18}O beams for $(t,^3\mathrm{He})$ experiments at intermediate energies. *Nuclear Instruments and Methods in Physics Research A*, 566(2):264–269, August 2006. http://dx.doi.org/10.1016/j.nima.2006.07.045.

[61] D. J. Morrissey, B. M. Sherrill, M. Steiner, A. Stolz, and I. Wiedenhoever. Commissioning the A1900 projectile fragment separator. *Nuclear Instruments and Methods in Physics Research B*, 204:90–96, 2003. http://dx.doi.org/10.1016/S0168-583X(02)01895-5.

[62] A. Stolz, T. Baumann, T. N. Ginter, D. J. Morrissey, M. Portillo, B. M. Sherrill, M. Steiner, and J. W. Stetson. Production of rare isotope beams with the NSCL fragment separator. *Nuclear Instruments and Methods in Physics Research B*, 241:858–861, December 2005. http://dx.doi.org/10.1016/j.nimb.2005.07.168.

[63] Y. Shimbara, R. G. T. Zegers, and M. Scott. Private communication, 2011.

[64] J. Yurkon, D. Bazin, W. Benenson, D. J. Morrissey, B. M. Sherrill, D. Swan, and R. Swanson. Focal plane detector for the S800 high-resolution spectrometer. *Nuclear Instruments and Methods in Physics Research A*, 422(1–3):291–295, 1999. http://dx.doi.org/10.1016/S0168-9002(98)00960-7.

[65] D. Bazin, J. A. Caggiano, B. M. Sherrill, J. Yurkon, and A. Zeller. The S800 spectrograph. *Nuclear Instruments and Methods in Physics Research B*, 204:629–633, 2003. http://dx.doi.org/10.1016/S0168-583X(02)02142-0.

[66] K. Meierbachtol, D. Bazin, and D. J. Morrissey. New CsI(Na) hodoscope aray for the S800 spectrograph at NSCL. *Nuclear Instruments and Methods in Physics Research A*, 652(1):668–670, October 2011. http://dx.doi.org/10.1016/j.nima.2010.10.053.

[67] Fuchi, Y. and Tanaka, M.H. and Kubono, S. and Kawashima, H. and Takaku, U. and Ichihara, T. High-Resolution, Two-Dimensional Focal-Plane Detector for Intermediate-Energy Heavy Ions. In *Nuclear Science Symposium and Medical Imaging Conference, 1992., Conference Record of the 1992 IEEE*, pages 172–174, October 1992. http://dx.doi.org/10.1109/NSSMIC.1992.301113.

[68] M. Berz, K. Joh, J. A. Nolen, B. M. Sherrill, and A. F. Zeller. Reconstructive correction of aberrations in nuclear particle spectrographs. *Physical Review C*, 47(2):537–543, February 1993. http://dx.doi.org/10.1103/PhysRevC.47.537.

[69] Kyoko Makino and Martin Berz. COSY INFINITY version 8. *Nuclear Instruments and Methods in Physics Research A*, 427:338–343, May 1999. http://dx.doi.org/10.1016/S0168-9002(98)01554-X.

[70] G. Audi, A. H. Wapstra, and C. Thibault. The AME2003 atomic mass evaluation. *Nuclear Physics A*, 729(1):337–676, December 2003. http://dx.doi.org/10.1016/j.nuclphysa.2003.11.003.

[71] C. J. Guess, T. Adachi, H. Akimune, A. Algora, Sam M. Austin, D. Bazin, B. A. Brown, C. Caesar, J. M. Deaven, H. Ejiri, E. Estevez, D. Fang, A. Faessler, D. Frekers, H. Fujita, Y. Fujita, M. Fujiwara, G. F. Grinyer, M. N. Harakeh, K. Hatanaka, C. Herlitzius, K. Hirota, G. W. Hitt, D. Ishikawa, H. Matsubara, R. Meharchand, F. Molina, H. Okamura, H. J. Ong, G. Perdikakis, V. Rodin, B. Rubio, Y. Shimbara, G. Süsoy, T. Suzuki, A. Tamii, J. H. Thies, C. Tur, N. Verhanovitz, M. Yosoi, J. Yurkon, R. G. T. Zegers, and J. Zenihiro. The ^{150}Nd(^{3}He, t) and ^{150}Sm(t,^{3}He) reactions with applications to $\beta\beta$ decay of ^{150}Nd. *Physical Review C*, 83:064318, June 2011. http://dx.doi.org/10.1103/PhysRevC.83.064318.

[72] B. Alex Brown and W. A. Richter. New "USD" Hamiltonians for the *sd* shell. *Physical Review C*, 74(3):034315, September 2006. http://dx.doi.org/10.1103/PhysRevC.74.034315.

[73] B. H. Wildenthal, M. S. Curtin, and B. A. Brown. Predicted features of the beta decay of neutron-rich sd-shell nuclei. *Physical Review C*, 28(3):1343–1366, September 1983. http://dx.doi.org/10.1103/10.1103/PhysRevC.28.1343.

[74] B. A. Brown and B. H. Wildenthal. Experimental and theoretical Gamow-Teller beta-decay observables for the sd-shell nuclei. *Atomic Data and Nuclear Data Tables*, 33(3):347–404, 1985. http://dx.doi.org/10.1016/0092-640X(85)90009-9.

[75] B. A. Brown and B. H. Wildenthal. Status of the nuclear shell model. *Annual Review of Nuclear and Particle Science*, 38:29–66, December 1988. http://dx.doi.org/10.1146/annurev.ns.38.120188.000333.

[76] N. B. Gove and M. J. Martin. Log-f tables for beta decay. *Atomic Data and Nuclear Data Tables*, 10(3):205 – 219, 1971. http://dx.doi.org/10.1016/S0092-640X(71)80026-8.